Investigation of Thermally Induced Stresses in a Transition-piece in Relation to an Aero-Derivative Gas Turbine Engine Operation

by

Alaaeldin H. Mustafa BEng, MSc

A thesis submitted in fulfillment of the requirement for the degree of

Doctor of Philosophy

Supervisor:

Professor M.S.J. Hashmi

Dublin City University
School of Mechanical and Manufacturing Engineering

July 2007

DECLARATION

I herby certify that this material, which I now submit for assessment on the programme of study leading to the award of Doctor of Philosophy, is entirely my own work and has not been taken from the work of others save and to the extent that such work has been cited and acknowledged within the text of my work.

Signed: _____ I.D. Number: 53122259

Date:

ACKNOWLEDGMENTS

First and foremost, I thank ALLAH, who bestowed me with the strength to complete this work.

I would also like to thank the following:

My supervisor, Professor Salem Hashmi, who guided me through this project and unselfishly dedicated his time to share his vast experience and knowledge. I owe him a lifelong debt of gratitude.

Professor Bekir Sami Yilbas for his inspiration, encouragement, and timely guidance throughout this research.

Dr. Mohmmet Sunar for his sustained interest and helpfulness during my study period.

My gratitude also goes to the librarian of the Exploration and Petroleum Engineering Information Center (EPiC), Saudi Aramco for her assistance during the course of this research.

Last but not least, I would like to say a sincere 'thank you' to my mother and wife for their loving encouragement and tireless support.

ABSTRACT

Investigation of Thermally Induced Stresses in a Transition-Piece in Relation to Gas Turbine Operation

By

Alaaeldin H. Mustafa B. Eng MSc

The transition-piece of an aero-derivative gas turbine engine transfers high temperature combusted gases from the gas generator to a power turbine, and it is manufactured from Iron-Base Superalloy A286 in this investigation. Due to the thermal stress levels developed in the casing of the transition-piece after long operating hours, the life expectancy of the transition-piece becomes shorter. The present study aims to investigate the thermal stress field development in the casing of the aero-derivative gas turbine engine transition-piece in relation to the flow and heat transfer situation inside the transition-piece. The typical operating conditions, under which the transition-piece is subjected, are accommodated in the model study to determine the amount of heat transfer from the combusted gases to the casing using CFD FLUENT code. The two-Dimensional CFD model is adopted in the study due to the axisymmetric flow situation in the transition-piece. Since the day to-day operation varies depending on the engine output demand, the model study is carried out under different operating conditions: (i) typical operating condition, (ii) ±10% change in mass flow rate, and (iii) ±10% change in combusted gas temperature. Temperature predictions of the numerical study are used as input to the thermal stress model to predict the thermally induced stress level in the transition-piece outer casing. The thermally induced stresses are computed through Finite Element Method (FEM) using the ANSYS code. Experimental work is carried out to determine the mechanical properties of the As Received

(AR) and Heat Treated (HT) A286 alloy through tensile and 3-point bending tests. The A286 alloy was heat treated to resemble the actual operating conditions of the transition-piece. Using the Scanning Electron Microscopy (SEM) and Optical Microscopy (M), the microstructure of the alloy prior and after the heat treatment is examined. The investigation concluded that the A286 alloy Young's Modulus of Elasticity (E) will reduce significantly due to operation at elevated temperature and that the fixed ends of the transition-pieces are the most likely areas to fail and result in reduction of the life expectancy of the transition-piece.

TABLE OF CONTENTS

LIST OF FIGURES

LIST OF TABLES

NOMENCALTURE

A	Cross-sectional area
a_o	Node coefficient
$C_{1,2}$	Various empirical constants in turbulent model
C_p	Specific heat (function of temperature)
C_μ	Viscosity constant
[D]	Elastic matrix
d	Diffusion term
E	Young's modulus of elasticity
E_{AR}	Young's modulus of elasticity for as received specimen
E_{HT}	Young's modulus of elasticity for heat treated specimen
G	Shear modulus (MPa)
g	Grams
h	Heat transfer coefficient
i	X axis direction
j	Y axis direction
K	Thermal conductivity
k_p	Local turbulent kinetic energy generation
L	Characteristic length
l	Length scale constant
n	Exponent
O,o	A typical node in the computational grid
P	Rate of production
p	Pressure
p′	Pressure correction
$p^\dagger$	Assumed pressure
P_{KK}	Production term
S	Source term

S_o	Source term at node 'o'
$\overline{S_T}$	Source term in the energy equation
$\overline{S}$	Source term average value over the control volume
S_u	Algebraic equation constant
T	Temperature
ΔT	Delta temperature
T_{amb}	
T_{ref}	Reference temperature (298.15 K)
T_s	Surface temperature
T_{iw}	Temperature an the inner wall
T_{egf}	Exhaust gas temperature
t	Turbulent
U	Velocity
U_i,	Velocity in the x direction
U_j	Velocity in the y direction
U^*	Friction velocity
$\overline{U}$	Time average arbitrary velocity
$\overline{u_i u_j}$	Reynolds stress per unit mass
$\overline{u_i \theta}$	Turbulent enthalpy per unit mass
$\overline{uw}$	Apparent shear stress
X	Axial direction
w	r.m.s. fluctuating velocity in the axial direction
x_i, x_j	Arbitrary axial direction
y	Distance in y direction
z	Co-ordinate direction normal to a solid wall
z_p	Mean velocity at point

z_p^+	Dimensionless distance where flow is fully turbulent
z_p^*	Dimensionless distance from point p to the solid wall

Abbreviations

Re	Reynolds number
w,e,s,n	Interface of a node to its west, east, south, and north
W, E, S, N	Centre of West, East, South and North.
AISI	American Iron and Steel Institute
TRIP	Transformation induced plasticity
ASTM	American Society of Testing and Materials
AISI	American Iron and Steel Institute
BWR	Boiling water reactor
PWR	Power water reactor
IGSCC	Intergranular surface corrosion cracks
RTO	Regenerative Thermal Oxidation
Pe	Peclet Number
SIMPLE	Semi-Implicit Method for Pressure-Linkage Equations
Nu	Nesselt Number
Pr	Prandtl Number
Re	Reynolds Number
hcp	Hexagonal closed- packed
XRD	X-Ray Diffraction
SEM	Scanning Electron Microscope
FEM	Finite Element Modeling

Greek

υ	Poisson's ratio
α	Linear coefficient of thermal expansion equations
ρ	Density (function of temperature and pressure)
μ	Dynamic velocity
μ_t	Turbulent dynamic viscosity
σ_K	Prandtl number (function of temperature)
σ_t	Turbulence Prandtl number
σ_{rr}	Stress in radial direction

$\sigma_{\theta\theta}$	Stress in tangential direction
σ_{zz}	Stress in axial direction
θ	Fluctuating component of temperature
κ	Turbulent kinetic viscosity
ε	Energy dissipation, Strain (table 11)
ϕ	Arbitrary variable
ϕ'	Fluctuating component of ϕ
δ_{ij}	Kronecker delta
Γ	Arbitrary diffusion coefficient
Γ_t	Turbulent diffusivity
ν	Kinematic viscosity (function of temperature)
$\rho\varepsilon$	Viscous dissipation term
ϑ	Turbulent velocity scale constant
η	Metallurgical phase
ξ	Arbitrary coordinate
$\rho\varepsilon$	Viscous dissipation term
χ	Wall roughness parameter
τ_w	Shear stress
$\forall$, V	Volume
ΔV	Volume in equation 3.18
p'	Pressure fluctuations in the turbulent flow field
$\{\in\}$	Total strain tensor
$\{\in^e\}$	Elastic strain tensor
$\{\in^{th}\}$	Thermal strain tensor
$\in$	Equivalent strain
ε_{rr}	Strain in radial direction
$\varepsilon_{\theta\theta}$	Strain in tangential direction
ε_{zz}	Strain in the axial direction

1

INTRODUCTION

Passages with gradual contractions and enlargements are found in a number of engineering equipment. Turbulent flows through such ducting systems can be encountered in industrial piping, jet pumps, gas turbines, air conditioning ducts, and other types of engineering systems and applications. Accurate determination of the flow field and heat transfer rates in engineering systems contributes significantly to efficiency increase, optimal design parameters, and ultimately reduction in cost-benefit relationship. The appropriate selection of bulk materials and equipment components is an important consideration for the economic success of these industries. Moreover, the need to minimise cost and enhance the reliability of rotating and stationary fluid machinery equipment that are subjected to high thermal stresses is of major importance. Consequently, understanding the behaviour of the material in use in the above described engineering systems is mandatory.

Advances in thermal efficiency and material system development, along with the readily available natural gas, have facilitated rapid growth of the combustion turbine market. At the same time, the investment in hot section parts as well as the cost of refurbishment has increased significantly; making life cycle management of these parts a major consideration in procurement and maintenance [1]. The ability to determine the present condition and predict the rate of future degradation of an equipment, or its components, depends on degradation monitoring technology and its incorporation into physical models that provide the basis for cost-benefit analysis, but most importantly it also depends on the engineer's experience and

knowledge. The hot gas path components of an aero-derivative (Figure 1) gas turbine engine include the combustors, combustors transition-pieces, transition seals, high pressure turbine, low pressure turbines, exhaust transition-piece (Figure 2) connecting the gas generator to a free power turbine (Figure 3.a and Figure 3.b, in which a schematic view of gas turbine engine and the location of transition-piece is shown). The gas generator is connected aerodynamically to the free power turbine via a transition-piece, while the power turbine is connected mechanically through a gearbox to the load, which is either a pump or a compressor. The transition-piece which connects the gas generator to the free power turbine is the focus of this study.

Modern gas turbines are designed to run at high turbine inlet temperatures in excess of some metals (such as nickel based alloys) melting temperature limits (~ 2100 K). In addition to improved temperature capability materials and thermal barrier coatings, highly sophisticated cooling techniques, such as augmented internal cooling and external film cooling, are used to maintain acceptable life and operational requirements under such extreme heat load conditions. To design a system that most efficiently cools the turbine hot-gas flow path components, it is necessary to better comprehend the detailed hot-gas flow physics within the turbine itself. There is a great need to increase the understanding of heat transfer within the highly turbulent and complex flow field. An example is the blade life which may be reduced by half, if the blade metal temperature prediction is off by only 283.15 K (Figure 4). Therefore, it is critical to predict accurately the local-heat transfer coefficient as well as the local blade temperature in order to prevent local hot spots and increase blade life. Current turbine designs are characterized by an inability to predict accurately heat-transfer coefficient distributions under turbo-machinery flow conditions. This results in a nonoptimised design causing penalties to the cycle in terms of power and specific fuel consumption [1].

The main function of the transition-piece under investigation here is to deliver the exhaust gases from the low pressure turbine exit to the power turbine inlet. In

doing that it should deliver the exhaust gases with the minimum disturbance to the face of the power turbine, with predetermined levels of pressure, velocity, and most importantly it should maintain its metallurgical integrity and be capable of withstanding the arduous operating conditions which manifests itself as high temperature, thermal fatigue, and creep which might lead to changes in the mechanical properties and eventually failure (Figure 5).

The flow field in the transition-piece influences the temperature distribution and the amount of heat transferred to its metallic casing. Due to the geometric configuration of the transition-piece, flow deceleration in the annular passage alters temperature distribution in the metal casing. High temperature of the combusted gas ($\approx$ 900 K) generates thermal stresses in the casing of the transition-piece. Since the transition-piece casing is fixed at both ends, the magnitude of the compressive stress level becomes high due to the thermal expansion of the casing material. Moreover, the elastic limit of the substrate material reduces significantly at elevated temperatures; consequently, investigation into the flow field, thermal stress development and its effect on the transition-piece casing material becomes necessary.

The potential importance of conjugate heat transfer in the downstream fluid in a diverging transition-piece relies on the thermal response of the solid casing. In this case, the flow velocity influences the average convective heat transfer coefficient in the flow region and the degree of heat transfer coefficient enhancement increases significantly with the wall inclined angle, with the temperature gradient in the solid casing initiates thermal stress field development. Moreover, depending on the magnitude of temperature gradient, extremely high thermal stress levels can be developed in the solid casing, which limits the operational duration and affect reliability of such equipment casings. Despite the progress made in the understanding of this phenomenon, practical applications in the operation and maintenance fields still present many research challenges. Problems such as

modeling of flow field and thermal stresses in these components give an insight into the possible failure mechanisms.

The objective of this research is to investigate and provide an explanation of the difficulties of misalignment of the transition-piece, encountered during installation. The effect of flow and heat transfer, on thermal stress levels in the transition-piece of an aero-derivative gas turbine engine (made of A286 Iron-Base Superalloy), is investigated numerically and experimentally. This is conducted under typical operating conditions of the transition-piece, taking into consideration typical operation variations as well as the effect of operating at elevated temperatures, encountered during operation of the aero-derivative gas turbine engine.

In the present study, the flow in the transition-piece resembling the actual aero-derivative gas turbine operating condition is simulated and the temperature field in the metallic casing of the transition-piece is predicted using the actual performance test bed data, which is then used for predicting the thermal stress developed in the casing of the transition-piece. FLUENT CFD code is used to simulate the flow and temperature fields, where the control volume approach is introduced when discretizing the governing equations of flow. While ANSYS FEM code is accommodated for the thermal stress predictions in the transition-piece casing. The material used in this investigation is Iron-Base Superalloy A286 and manufactured by BOHLER EDELSTHL of Germany [2], which is identical to the actual material of the outer casing of the transition-piece under study. The alloy is used widely in the gas turbine industry due to its superior mechanical properties; however, its mechanical behavior, in gas turbine applications at elevated temperature, which result in thermally induced stresses, has not yet been widely researched. Moreover, to resemble the actual hot gas environment and its influence on the thermo-mechanical response of the transition-piece substrate material, A286 alloy is heat treated. The mechanical properties of the heat treated alloy are assessed through tensile and three-point bending tests. Consequently, the properties obtained from the experimental tests are used in the simulation, to

compare the thermal stresses developed in the casing, due to different operational conditions corresponding to the as received and heat treated alloy.

The thesis in hand, is divided into several chapters, chapter one is the introduction while chapter two gives a summary of relevant literature concerning fluid flow simulation, thermally induced stresses simulation and material testing. Various research sources were considered, including journal publications, and conference proceedings. It was noted that literature about the Iron-Base Super alloys is scarce, which drove the thesis author towards widening the search for this type information.

The mathematical modeling part of the report is covered in chapter three. In this chapter the mathematical equations and reasoning used in the fluid flow and thermal stress simulations are covered. It includes continuity, momentum and energy equations, eddy-viscosity models, equations for turbulent kinetic energy and the dissipation energy, wall functions, SIMPLE and SIMPLEC algorithms and the specific computational grid and boundary conditions for the concerned problem.

The experimental procedure is described in chapter four including, 3-point bending and tensile tests, the equipment used, experimental procedure and set-up required to conduct them. The experimental set-up is explained separately in each of the parts as per the ASTM standards. Thermal analysis finite element modeling is presented in the final section of chapter three. This section describes the finite element analysis technique and procedures used in the current research.

The results and discussion of the research are presented in chapter five. The results show a characterisation of the Iron-Base Superalloy A286 including Scanning Electron Microscopy (SEM) and Energy Dispersive Spectrometer (EDS) analysis. Mechanical properties of the tested material that had been studied were discussed.

Mechanical tests result as a whole are correlated with the micro-structural analysis and discussed to conclude the chapter.

Finally, chapter six presents the overall conclusions drawn from the results and provides recommendations for the future work in this area. Future research might include expanding the current study to include other experimental work such as creep testing and its relationship with transient operation of gas turbines, especially in the areas of high temperature application and the aerospace industries. Several articles were drawn up from this work and published, including journal and conference papers, a list of which is referenced in "Publications Arising from this Work" section of the report.

Figure 1, Pratt and Whitney (P&W) FT4-9B Gas Turbine Engine
(Saudi Aramco Gas Turbine Repair Shop)

Figure 2, Pratt and Whitney (P&W) FT4-9B Exhaust Transition- Piece
(Saudi Aramco Gas Turbine Repair Shop)

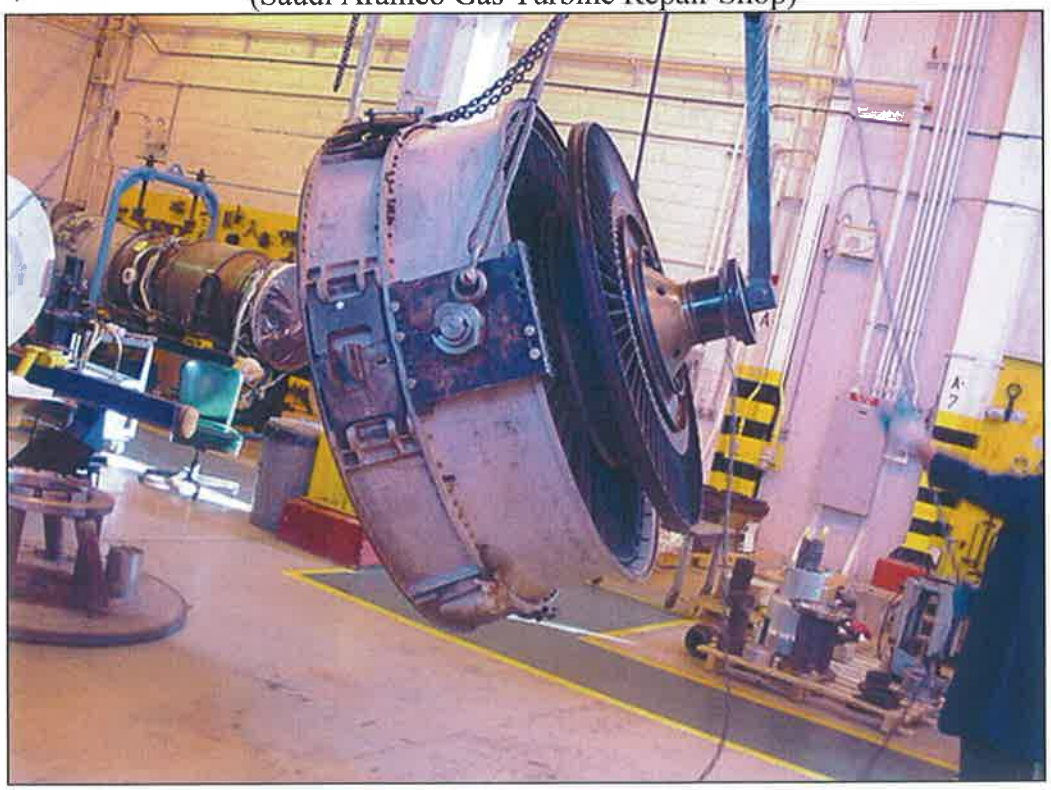

Figure 3.a, Pratt and Whitney (P&W) FT4-9B Free Power Turbine
(Saudi Aramco Gas Turbine Repair Shop)

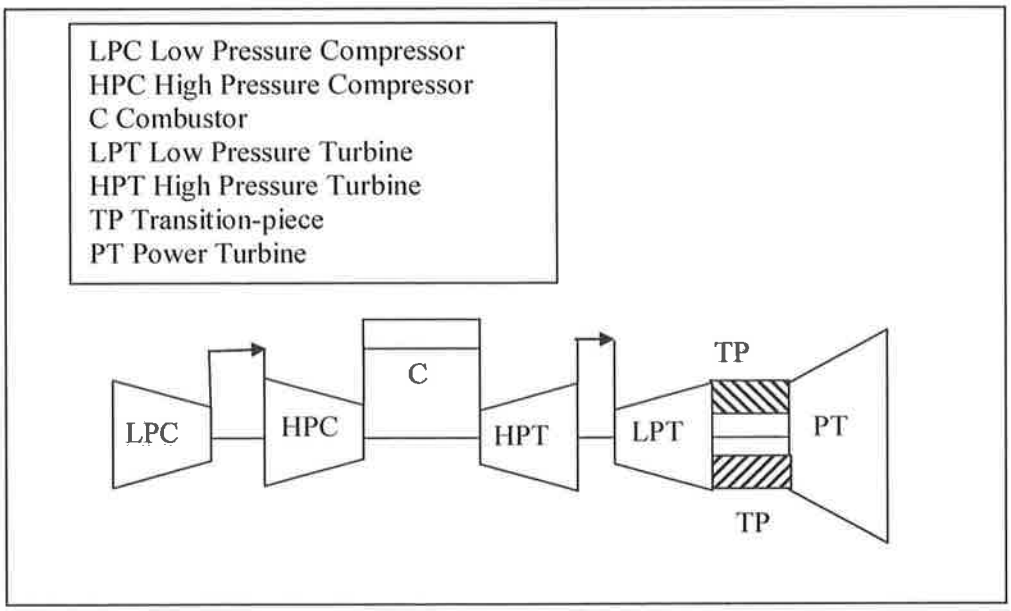

Figure 3.b, Schematic view of gas turbine engine and the location of the transition-piece.

Figure 4, Rolls-Royce RB211-24C heavily eroded 1st stage turbine rotor blades (Saudi Aramco Gas Turbine Repair Shop)

Continuous Duty	Cyclic Duty
-Rupture	-Thermal Mechanical Fatigue
Creep Deflection	- High-Cyclic Fatigue
-High-Cyclic Fatigue	-Rubs/Wear
-Corrosion	-Foreign Object Damage
-Oxidation	
-Erosion	
-Rubs/Wear	
-Foreign Object Damage	

Figure 5, Potential failure modes in hot gas path components [3].

2

LITERATURE SURVEY

2.1 INTRODUCTION

Flow of hot gas through a transition-piece finds wide applications in the power industry such as petrochemical plants, power generation stations and process plants. In aero-derivative gas turbine engines in mechanical drive applications, high temperature gas leaving the gas generator and entering the power turbine is delivered through a transition-piece. The flow field in the transition-piece influences the temperature distribution in the metallic casing. Due to the geometric configurations of the transition-piece, viscous dissipation and heat transfer in the flow field alters temperature distribution in the metal casing of the transition-piece. The high temperature of the combusted gas ($\approx$ 900 K) generates thermal stresses in the transition-piece casing. Since the transition-piece casing is fixed at both ends, the magnitude of the compressive stress level becomes high due to the thermal expansion in the substrate material. Moreover, elastic limit of the substrate material reduces at elevated temperatures; consequently, investigation into the flow field and thermal stress development in the transition-piece casing becomes necessary. In addition, an understanding of the developed thermal stresses in metal casings is important for understanding the service life limitations of the transition-piece.

The literature survey in this chapter focuses on several points, including a section about the fluid flow and heat transfer simulations which will be followed by metallurgy section including the stainless steel alloys, in particular A286 Iron-Base

Superalloy. Finally, a background literature survey associated with the thermally induced stresses will be addressed.

2.2 FLUID FLOW

2.2.1 Fluid Flow Numerical Simulation

Considerable numerical, experimental, and analytical research studies were conducted to examine the fluid flow process in industrial equipment. The following section outlines the early studies performed in this area:

The flow conditions in a closed-circuit wind tunnel were investigated numerically and experimentally to model the flow conditions with the purpose of incorporating Computational Fluid Dynamic (CFD) technique in wind tunnel design and testing [4]. The results showed that the proposed simulation technique reproduced the experimental measurement to within 10% accuracy. The flow field in three different centrifugal fan impellers was investigated numerically [5]. The investigation used FLUENT code to study the effects of tip clearance on the overall performance. It was shown that the impeller with backward-curved blades was very sensitive to tip clearance, while the impeller with radial tipped blades showed weak dependency to tip clearance and impeller with fully radial blades was insensitive to tip clearance. Numerical investigation of flow round rows of cylinders was conducted [6]. It was shown that for flow round one row of cylinders, 180° out-of-phase vortex shedding was observed when the gap separating the cylinders axes was four diameters (4d) and Re was 100. For flow around two rows of cylinders of unequal sizes in an in-line arrangement, the flow pattern was dependent on the separation between the two rows. Investigation of particles tracking with a degree of accuracy and optimization of particle-separation devices was conducted with the results compared with the experimental data [7]. It was shown that for velocities lower than 12.3 m/s, the particle tracking gave results with a relative error below 24%, and for velocities above 48 m/s the simulation is

no longer accurate. The study finally recommended that FLUENT code was to be used in simulations to find a way of reducing the particle emissions.

The effect of upstream air supply system on the air flow distribution in top-spray fluidized bed reactor was investigated numerically comparing the results to laboratory results [8]. It was shown that using two dimensional simulation would deliver more accurate results for a homogenous airflow, but for unequal airflow conditions, three-dimensional simulation was more suitable. The effects of flow velocity on the local heat transfer in a corrugated duct were investigated experimentally and numerically [9]. It was shown that at low Re number ≤ 1000, the secondary vortices perpendicular to the stream-wise direction were generated in the duct, while at $Re \geq 1000$ the effect of the secondary flow disappears as the flow transition from laminar to turbulent occurred. The effect of duct width on fully developed turbulent flow characteristics in a corrugated duct was investigated numerically and experimentally [10]. It was shown that the width aspect ratio had a considerable effect on both the flow pattern and the friction factor. Moreover, the experimental results indicated that a complex flow involving flow separation, reattachment, and recirculation zones existed with the strength of the recirculation and the size of the recirculation region increased with the increase in the corrugation angle. Experimental and numerical investigations were conducted on internal compressible flow at T-type junction to develop a global methodology [11]. It was shown that the Mach numbers simulated were mainly influenced by branch lengths of the junction. Moreover, it was also shown that the correlations obtained could be used in a one dimensional global simulation model.

The use of baffles and/or turning vanes in reducing the required pressure and identification of the optimum baffle angle for pressure drop reduction was investigated [12]. Numerical investigation was performed using CFD code, while experimental investigation was conducted using 1:40 scale model. It was shown that the experimental results confirmed that the introduction of a baffle reduced the pressure loss more than that of the vanes; moreover, using the turning vanes was

not helpful in reducing the pressure loss coefficient. Analyzing flow pattern of isothermal air emitting from an annular orifice was investigated to develop a method for investigating annular melt-blown dies numerically [13]. The results showed that annular jets had significantly different flow characteristics than circular jets and that the presence of inner annular wall induces a large difference in turbulence behavior mainly extending the circulation zone. Large Eddy Simulation (LES) for synthetic jet thermal management in a micro-system packaging application was numerically investigated [14]. It was shown that using LES turbulence model instead of direct numerical simulation allowed the simulation to be completed in a reasonable time, with the model exhibiting a satisfactory accuracy compared to experimental results obtained form the published literature.

2.2.2 Numerical Simulations in Analysis Field

Among the many fields in which numerical techniques are widely used, the field of analysis is the largest, as it is a part of all other fields. The accuracy of the results which could be obtained from numerical techniques has improved dramatically in the last few years in all the fields. The application of numerical techniques in the analysis field is overviewed below.

The possibility of capturing the effect of strongly swirling confined flow using finite-volume procedure in conjunction with a Reynolds-Stress Transport was investigated numerically [15]. It was shown that the Reynolds-stress model captured these features, whereas the isotropic-viscosity κ-ε did not. A finite volume scheme using FLUENT platform was adopted to determine the stiffness and damping coefficients of plain annular seals used in high speed cryogenic pumps [16]. The results showed good agreement with the stiffness coefficients determined from classic analysis, with the results from the classic analysis showing slightly higher values than the numerical analysis. Simulating the atmospheric

boundary layer using sand-grain roughness wall function was conducted to investigate and compare the accuracy with the experimental data [17]. It was shown that the accuracy of the simulation can seriously be compromised when wall-function roughness modifications, based on experimental data for sand grain roughened pipes and channels, were applied at the bottom of the computational domain and this problem was found in all available commercial CFD codes. Numerical techniques were also used to investigate the efficiency of alternative designs for a flow mixing tank in Regenerative Thermal Oxidation (RTO) [18]. It was shown that the results obtained provided an important insight into the flow and temperature distribution for the cases modeled, which led to improved design.

2.3 HEAT TRANSFER

2.3.1 Heat Transfer

The heat transfer process in a square enclosure, heated by a localized source and symmetrically cooled from the sides was investigated numerically and experimentally [19]. It was shown that the heat transfer was generally conductive for $Ra \leq 10^4$ while the convective phenomenon develops completely for $Re \cong 10^5$. Moreover, it was reported that an increase of the heat source dimension produced a rise in heat transfer particularly for high Re. An investigation of the heat transfer rate and Nusselt number in a circular tube entry region was conducted experimentally [20]. Although the study was limited to only circular cross sectional tubes, a single correlation equation was proposed that could be used to evaluate the mean and local Nusselt number for all ranges of dimensionless axial distance, for tubes with noncircular cross sections. Numerical assessment of the transient temperature and thermally induced stress distributions in a rotating hollow disk subjected to a thermal process was conducted [21]. It was shown that the coolant velocity had a significant effect on the converging times, and that the periodic increase and decrease in the thermal stress could cause thermal fatigue. An investigation was conducted to find a solution for a conjugate heat transfer

problem with volumetric heat generation [22]. The calculated drag coefficient and Nusselt number from the developed semi-analytical procedure were compared with the results of the finite volume method; excellent agreement was obtained. An investigation of heat transfer performance of non-uniform airflow distribution in radiators was conducted [23]. It was shown that the loss of performance caused by airflow maldistribution, compared with uniform airflow of the same total flow rate, was relatively minor except under extreme circumstances where the non-uniform factor is large.

The effect of friction and different shapes on the heat transfer in channels with fully developed flow regime was investigated experimentally [24]. It was shown that the square shaped roughened geometry had the highest friction factor and the triangle shaped geometry had the highest heat transfer value. The convective heat transfer coefficient and velocity profile for fully developed turbulent flow in a concentric annulus having rough or smooth walls was investigated experimentally [25]. It was shown that for a smooth annulus, the comparison between the calculated and experimental heat transfer and the velocity profile was close, while for the roughened annulus the difference for the velocity profile was greater than that for the smooth annulus and satisfactory for the heat transfer rate. Natural convection heat transfer in two dimensional semicircular slice pool was investigated experimentally [26]. It was shown that the obtained heat flux profile along the lower wall was in good agreement with the data obtained from literature, with the lowest value of heat flux occurring at the bottom of the vessel and the highest in the upper corner of the vessel. Turbulent opposing mixed convection heat transfer in a vertical flat channel with one-side heating was investigated experimentally [27]. Results recommended a correlation for different air pressures and a general correlation for heat transfer calculation in a vertical flat channel with one-side heated. Several turbulence models used in modeling strongly heated, low-Mach number gas flowing upward were investigated numerically [28]. It was shown that in the case involving constant fluid property assumption, the results obtained using $v^2 - f$ turbulence model, were in close agreement with Dittus-

Boelter correlations. For the variable property, the results showed that $v^2 - f$ model was able to predict the experimental data for wall temperature with acceptable engineering accuracy.

The effect of heating turbulent gas flow within ducts of square cross-section was investigated numerically using large eddy simulation [29]. It was shown that a gradual increase in temperature and reduction of the viscosity near the heated wall yielded a progressive enhancement of the turbulent structures. Moreover, it was shown that heating enhanced both the size and the intensity of the vortices close to the wall. Heat transfer in a tube bundle model was conducted numerically and validated experimentally [30]. It was shown that the circulation velocity and the predicated Nusselt number (Nu) agreed with the experimental data, while the experimental losses from the production tubes and the heating tube were approximately 10% higher than predicted. Heat transfer performance characteristics of automotive radiators were investigated numerically for possible design change [31]. It was shown that the plate design for road transportation radiator had higher heat transfer levels, lower pressure drop levels, lower overall vehicle drag, smaller size and cheaper to manufacture. Heat transfer characteristics of a compact heat exchanger were investigated numerically using FLUENT code [32]. It was shown that the numerical mesh dependency of coarse mesh leads to a better estimation of the difference in heat transfer between the different models and the difference between the experimental and the numerical results was 4.2%.

2.3.2 Conjugate Heat Transfer

The first step in understanding the impact of the heat transfer phenomenon on the transition-piece is to understand the technique and the methodology with which the heat transfer process is predicted.

Conjugate heat transfer in steady flows was studied extensively; cooling of simple

conjugate heat transfer geometry, in a steady shear flow over a heated strip on a flat plate was investigated numerically [33]. A simple correlation for predicting the heat transfer coefficient was presented. Moreover a new combined parameter for accommodating the importance of the fluid axial conduction was suggested. Conjugate heat transfer in fully developed laminar flow with temperature dependent thermal properties and the thermally induced stress were numerically investigated under both steady state and transient conditions [34]. It was shown that the relative temperature in the pipe for temperature dependent thermal conductivity was higher by about 1% than if constant temperature thermal conductivity was used. Conjugate heat transfer and two-phase, three-dimensional flow field inside the face of a disk-shaped miniature heat pipe under various fluid flow situations were investigated numerically [35]. Experimental results were used to improve the numerical modeling. It was shown that an effective model could be built and acceptable results obtained compared to the experimental ones. The conjugate heat transfer in relation to a power-law in a fully developed velocity profile and in contact with a heat tube was investigated numerically [36]. It was shown that the heat transfer characteristics were governed by the diffusion as well as the power-law index.

Unsteady conjugate heat transfer phenomenon was investigated by several researchers for different flow conditions. In general it was observed that the effect of the wall conduction on heat transfer rates was more pronounced for high values of wall-to-fluid thermal conductivity ratio, wall-to-fluid thermal diffusivity ratio, and wall thickness to inner radius ratio [37]. This was particularly true for low values of Peclet Number (Pe). The conjugate heat transfer phenomenon in a circular cylinder and surrounding laminar cross-flow at low Reynolds numbers was investigated numerically [38]. It was shown that the rate of conjugate transfer from a cylinder exhibited the same main characteristics as the rate of the conjugate transfer from a sphere. Transient conjugate heat transfer was investigated numerically in a liquid oxygen seal chamber, using FLUENT code, with turbulent based κ- ε RNG model, standard wall function, and SIMPLE coupling algorithm,

and the results obtained in the steady state solution simulated values compared well with those values obtained analytically [39].

2.3.3 Numerical Simulations in Gas Turbines Applications

Use of numerical simulation in the field of aerospace is a long established process, saying that, research in some areas of the aerospace field, such as space and rockets, is still scarce or not available in the public domain, due to its sensitive nature. In the areas of gas turbine engine design, modification, analysis, and testing the use of numerical simulation is a common practice among the gas turbine manufacturers. The temperature behavior of gas turbine first stage nozzles, with internal and film cooling systems in steady-state conditions, was investigated numerically [40]. It was shown that the coolant flow rate and the temperature values significantly influenced the heat transfer in the nozzle solid body, thus influencing the maximum solid body temperature and temperature profile. The cavitations characteristics of a gas turbine propeller were investigated [41]. It was shown, that for single blades, the results obtained were within reasonable agreement with CFD results, and higher by 20% than the experimental results, however, when the full model was considered the results from both techniques were found to be much closer. Heat transfer in full film cooling of an aero-engine annular combustor was investigated numerically [42]. It was shown that with proper distribution of film cooling holes, the air film was uniform and could protect the combustion tube walls. However, strong injections from the dilution holes would penetrate the cooling film and affect the areas near the dilution holes. A gas turbine engine highly pressurized cavity thermal model was validated numerically [43]. Results from the test rig demonstrated close agreement with the CFD results, once the over tip leakage was taken into account. Moreover, comparison at stabilized conditions indicated good agreement between numerical and experimental results for measured velocity and reasonable agreement with the measured heat flux. Numerical simulation of heat transfer in a space transportation

reusable solid rocket motor was conducted [44]. It was shown that for obtaining an accurate prediction using a two-dimensional model, the selection of numerical schemes and turbulence models should be based on the mass flow rate, vacuum thrust and chamber pressure drop. The influence of the inlet swirl and Mach number on the diffuser pressure recovery and diffuser losses in industrial gas turbines exhaust diffusers was conducted [45]. It was shown that that the pressure recovery was independent from the inlet Mach number, but varied with the inlet swirl due to the flow separation at the struts caused by different incidence angles and no universal correlation could be developed.

2.3.4 Ducts, Pipes, and Nozzles

CFD techniques have been in use vastly to simulate flow in ducts, pipes, and nozzles. The swirling flow through an annular diffuser was investigated numerically to update the mixing length model with the swirl effects [46]. It was shown that the obtained predicted results had a close agreement with the available experimental data. The effect of swirling turbulent flow in a stationary annulus was investigated numerically [47]. It was shown that swirl number increase, led to increase in tangential velocity, turbulent kinetic energy and heat transfer coefficient, while the gas axial velocity remained almost unchanged in the central region and as a result of the increase in the heat transfer, the gas temperature decreased with increasing swirl number.

The influence of free convection and variable viscosity on forced laminar flow fluid in horizontal annular duct heated at a constant heat flux density was investigated numerically [48]. It was shown that a decrease of dynamic viscosity with temperature; induces intensification of the secondary flow and an acceleration of the axial flow in the upper part of the duct. Moreover an increase of the overall heat transfer in forced and mixed convection was observed. The temperature and thermal stress distributions of fully developed laminar flow in a circular pipe under

uniform and non-uniform heat flux were investigated for two mean flow velocities [49]. It was shown that for uniform and non-uniform heat fluxes, the temperature distribution of the pipe inner surface was higher for lower velocity, while the temperature difference between the inner surface and the centerline at the same axial distance was higher with the higher velocity. Moreover it was observed that the stress ratio increased linearly with increasing heat flux. Estimation of unknown outer – wall heat flux in turbulent circular pipe flow with conduction in the wall pipe was investigated numerically [50]. The results showed that the proposed inverse method could be used to solve the steady two dimensional conduction and convection cases with accurate results, even when a measurement error of 3% is introduced. The importance of conjugate heat transfer in flow through a converging-diverging nozzle resembling the flow expansion in passages was investigated numerically [51]. It was shown that cooling of the nozzle wall temperatures below the bulk fluid temperatures was possible, as a result of conjugate heat transfer.

Numerical investigation of turbulent flow in small angle diffusers and contractions using new wall treatment and linear high Reynolds κ-ε model was conducted [52]. It was shown that for contractions with angles of up to 21° the use of parabolic solver could capture the basic features of the flow. Moreover, it was observed that, accelerated flows in convergent ducts reduce turbulence level while turbulence increases in divergent ducts. Numerical investigation of two sets of experimental data for varying converging-diverging nozzles angles and length was conducted [53]. It was shown that the degree of wall cooling and the magnitude of the temperature gradient varied with an effective bubble diffusion coefficient and that the wall cooling increased with increasing wall conductivity and decreasing nozzle length. The influence of turbulence model in modeling wall-to-fluid heat transfer in packed beds was investigated using FLUENT code [54]. It was shown that near-wall modeling was fundamental to obtain more accurate results, for pressure drop and heat transfer values, and the selection of the right turbulent model depended on the geometry proposed and the value for y^+ in the wall. The

performance and flow characteristics for a wide range of geometrical factors in conical walled annular diffusers were investigated experimentally [55]. It was shown that the separation of the boundary layer occurred only on the outer wall with the velocity profile in the outlet section of the diffuser maintained axial symmetry whether the flow separation occurs or not.

2.4 STEEL ALLOYS, TESTING AND THERMALLY INDUCED STRESSES

2.4.1 Stainless Steel AISI 660 (A286)

The Iron-Base Superalloy A286 is widely used in industries such as petrochemicals, power generation, nuclear power, process plants and gas turbine engine parts at intermediate temperature range due to its properties [56]. It is a 25% Nickel (Ni), 15% Chromium (Cr) austenitic alloy containing Titanium (Ti) and Aluminum (Al) additions. It is strengthened mainly by an ageing process at 730 °C for 16 hours, by coherent precipitation of the ordered Face Center Cube (FCC), gamma prime (γ') phase, Ni (Al, Ti) into an austenite matrix. The main feature of this material is that it displays similar mechanical properties both at service conditions and at room temperature, as well as good corrosion resistance due to its chromium content. However, this alloy is unstable when aged at 730 °C for one hour because the metastable γ' shrinks in favor of the stable phase (Hexagonal closed- packed) hcp Ni_3 Ti, which degrades the mechanical performance of the material. Hence, the relatively low strength of this alloy restricts its extensive use in parts that require high strength during high temperature service. The effect of hot working conditions on the grain size of A286 alloy was investigated experimentally to determine the effect of grain size on the mechanical properties [57]. It was shown that finer grain sizes were obtained at lower heating temperature at various hot working conditions. Moreover, it was also reported that the required working ratio at which smaller grain size was obtained, decreased with lower heating temperature. The behavior of A286 in a Boiling Water Reactor (BWR) service environment was investigated when cracks

were found in the core grid screws and core beam of a nuclear power system water reactor. A long term test for investigating the susceptibility of construction materials to Intergranular Service Corrosion Cracks (IGSCC) was carried out earlier [58]. It was shown that the A286 had a clear susceptibility to IGSCC in BWR environment. It was also reported that there was a clear correlation between susceptibility to IGSCC and applied tensile stress.

A study was conducted to investigate the relationship between the structure and the IGSCC performance of Inconel X-750 to Iron-Base A286 and Inconel X-718 alloys [59]. It was shown that no crack initiation occurred on any of the X-750,718 or A286 U-bend specimens during the 6,000 hours exposure to Power Water Reactor (PWR) primary water at 650 °C. It was also reported that crack growth was observed in all the pre-cracked specimens and the crack growth was intergranular in all the specimens, except for one X-750 specimen where the crack growth was transgranular. The effects of Ti content and heat treatment conditions on the properties of a large A286 alloy rotor forging were examined experimentally [60]. It was shown that the Ti Carbides film between the grain boundaries were responsible for the notch brittleness and decrease in the notch-rupture strength. Moreover it was reported that the creep rupture ductility was improved by decrease in Ti content, and the notch creep rupture strength was improved by applying multiple ageing treatments and that tensile, creep rupture and low-cycle fatigue properties of the A286 forgings were comparable to those small forgings with conventional Ti content.

A database was developed to set allowable stresses for A286 in the duplex aged conditions [61]. Tensile tests were performed from room temperature to 1300 °F to establish the yield and ultimate tensile strength trend curves. The study showed that the grain size was the key factor with regard to higher temperature stress-rupture strength and that strength decreased with the decrease in grain size. It was also reported that the duplex heat treatment did not enhance or reduce long term stress-rupture strength. The micro-structural development and creep behavior in A286 superalloy was investigated experimentally focusing on the effect of ageing

treatment on microstructure, hardness and creep behavior [62]. It was shown that the precipitation of the stable η phase degrades the mechanical behavior of the alloy, which could be reduced by a factor of 50 for samples aged in the order of 500 hours at the critical temperature. It was also reported that despite the difference in microstructure produced by the various ageing treatments, all the creep specimens were characterized by intergranular failure mode.

The influence of the initial austenite grain size on the sub-grain and dislocation structure changes in A286 alloy was investigated experimentally [63]. It was shown that all the substructure transformations were not self-contained processes and the temperature had an influence on the size of the sub-grains and dislocation density. Moreover, it was found that the increase of the alloy deformation temperature led to a growth of the sub-grain size with a simultaneous decrease in the internal dislocation density. The influence of prolonged ageing in the process of precipitation in an austenitic alloy of A286 type was investigated experimentally [64]. It was shown that the size distribution of the γ' phase shifted at the maximum limit level towards the classes of larger diameter with increasing ageing time. Moreover it was reported that the application of single stage ageing provoked the precipitation of intermetallic phases as well as carbides. Analysis of hydrogen embrittlement on crack propagation was carried out experimentally on three different alloys, Inconel 718, Inconel 625 and A286 [65]. It was shown that all the alloys tested were susceptible to internal hydrogen embrittlement, with the A286 failing at or near grain and twin boundaries for internally charged hydrogen, and that susceptibility to hydrogen embrittlement was more pronounced for the precipitation hardened alloys (A286) and less pronounced for single-phase alloy (Inconel 625). Finally, it was found that hydrogen enhanced the localization of plastic deformation. Crack initiation and near threshold surface fatigue crack propagation behavior of the iron-base superalloy A286 was investigated experimentally [66]. It was shown that the surface crack growth rates were nearly twice as high in the overaged samples as compared to the underaged microstructure.

Recently by adding Niobium (Nb) element, the modified A286 has been developed. It was reported by several researchers, that the addition of Nb element to iron-base superalloy increases the amount of γ' phase, the main strengthener, and improves the stability of γ' phase to give higher strength; longer fatigue life and creep rupture time than those of commercially A286 alloys [67-72].

2.4.2 Heat Treatment Effects

The effect of cooling rate on the microstructure evaluation of rapidly cooled high-impurity steels was investigated experimentally and analytically [73]. It was shown that the near-net-shape casting process with rapid solidification had led to the creation of ultra-fine grained steels from scrap steels with proved benefits of refinement of the microstructure. Heat treatment of steel parts was investigated experimentally [74]. The research demonstrated the significant effect of the phase transformations on both residual stress and distortion in carburized and hardened steel alloy parts. It was shown that the carburizing and hardening processes were in agreement with the measured values of distortion and residual stress obtained from the experimental study.

The feasibility of obtaining low Al/Si multiphase steels with appreciable amounts of retained austenite was investigated experimentally [75]. It was concluded that the influence of intercritical annealing temperature was important due to the formation of a high fraction of residual austenite at elevated temperature and that Al and Si contents were vital elements for the retention of austenite in multiphase steels for obtaining of the improved mechanical properties. An investigation to establish the appropriate intercritical annealing (IA) and isothermal bainite treatment (IBT) for Transformation Induced Plasticity (TRIP) steel was carried out experimentally [76]. It was shown that the heat-treatment conditions of intercritical annealing and isothermal bainite treatment were vital for the formation of retained austenite. It was also indicated that at the intercritical annealing

temperature, the retained austenite volume fraction increased with the increase of time. Moreover, it was reported that the carbon concentration, examined by X-ray diffraction (XRD), was 0.84% in retained austenite revealing the higher stability, which was confirmed by Optical Microscopy (OM) and Electron Transmission Microscopy (TEM).

The effect of different types of modified heat treatments on the mechanical properties of AISI 4130 steel was investigated experimentally [77]. The results showed that successive austempering improved the mechanical properties compared with the continuous cooling and conventional austempering. It was shown that the best combination of mechanical properties was achieved when an up-quenching heat treatment was used. The influence of the tempering treatment on the cyclic behavior of martensitic steel was investigated experimentally through focusing on the effects of ageing, testing temperature and strain rate on cyclic behavior for various tempered conditions [78]. The results showed that for testing temperatures lower than the tempering temperature, the maximum stress of the tested steel, as well as the stress amplitude, increased with the initial hardness decreased with testing temperature, and the ageing remained nearly constant. The effect of heat treatment on the wear resistance of high-carbon and high nitrogen steels subjected to abrasive wear was investigated experimentally, focusing on the effect of heat treatment on the wear resistance and hardenability of the functional surface subjected to abrasive wear for austenitic steel [79]. It was shown that the dependences of the hardness and wear resistance of the studied steels on the tempering temperature after quenching differed substantially. The wear resistance of the high-manganese steel in the studied temperature range virtually did not change with the tempering time.

2.4.3 Material Characteristics

The behavior of iron-silicon alloys deformed in axisymmetric compression at room temperature was investigated experimentally [80]. The silicon content of the

material was varied, and the samples were heat treated prior to deformation, that followed by examining the microstructure using Light Optical Microscopy (LOM) and Scan Electron Microscopy (SEM). The results showed that the increase in silicon led to increase in yield strength, which increased with deformation. Moreover, it was also shown that the cooling rate exerted had a major effect on the strength of the material. The microstructural and mechanical characterization of C-Mn-Al-Si cold rolled TRIP-aided steel was investigated [81]. The study focused on the retained austenite characteristics and tensile properties in high strength cold-rolled TRIP steel. The results showed that the formability and the amount of retained austenite decreased with the increments of intercritical holding time, and the carbon concentration in retained austenite led to a high degree of stability. The mechanics of ductile fracture in bulk metal forming processes were investigated [82]. A computer program using finite-element method was developed such that the behaviour of crack propagation after ductile fracture could be analysed. The results showed that the effect of the ductile fracture criteria on the behavior of crack propagation obtained numerically agreed with the experimentally obtained results.

2.4.4 Material Testing

Young's Modulus of Elasticity (E) and fracture toughness were investigated experimentally for High Velocity Oxygen-Fuel-Sprayed (HVOF) bioceramic coating [83]. It was shown that the surface coating roughness had a significant effect on the Modulus of Elasticity (E) value and improvement could be possible by fine polishing. (E) values obtained through three points bending test were found to coincide well with the results obtained for the four points bending test. A novel method for the measurement of E for thick – film resistor material by three points bending test was conducted [84]. Test beams were stabilized at the test temperature and a comparison was made between the coated and the uncoated samples. The results showed an agreement with the published values. The

strengthening effect of (Ni, Fe) Al precipitates on the mechanical properties at high temperatures of ferritic Fe-Al-Ni-Cr alloys were investigated experimentally [85]. Four points bending tests were carried out. The four points bending tests study showed that the heat treatment had a strong influence on the brittle to ductile transition temperature. After two-step ageing, the transition temperature was reduced due to the increase in the interparticle spacing.

Coated Ti-6A1-4V alloy was investigated experimentally and numerically to determine the mechanical properties by three-point testing [86]. It was shown that the Von-Mises stress in excess of the elastic limit at coating-base material interface extends in a horizontal direction, which indicated that the crack formation in the coating was unavoidable. As the load level increased, elongated cracks were formed, particularly in the region of maximum deflection. The effect of Cold Work (CW) on tensile properties and the effect of temperature on Low Cycle Fatigue (LCF) behavior prior to (CW) of 316L stainless steel were investigated experimentally [87]. Two conditions of 316L were considered, the 17% CW and the solution treated. Tensile tests and LCF were performed and it was shown that all four strengths measured (yield strength, engineering ultimate tensile strength, true ultimate tensile strength, and fracture strength) for both conditions exhibited a decrease with increase in temperature and the cyclic softening behavior depended strongly on temperature and total strain amplitude. The mechanical properties of the coating and coating-base material interface properties were investigated experimentally and numerically through three points bending tests [88]. It was shown that the compression stress levels developed on the tensile surface of the substrate material and in the coating exceeded the yield point, which facilitated local crack initiation in the coating as well as at the coating-base material interface. Three-point bending test was used to investigate the laser treatment effect on HVOF sprayed Inconel-625 coatings [89]. The results indicated that the elastic limit of the coating reduced after the laser treatment. Moreover, it was shown that the origins of crack sites were initiated at the coating/substrate interface. The stress profile in two different types of coating was investigated experimentally

using four-point bending test [90]. It was observed that the four-point bending stress profile for the coated sample was similar to the tensile test profile.

The ageing of a Fe-Ni-Co-Nb-Ti-Si superalloy under tensile stress was investigated experimentally to determine the effect of a tensile stress on precipitation during ageing [91]. Microstructural observations were conducted with TEM and OM. The study results showed that tensile stress promoted precipitation of ε plates within grains during aging, as well as enhancing the growth of grains at high temperatures.

2.5 THERMAL STRESS MODELING AND RESIDUAL STRESS

2.5.1 Thermal Stress Modeling

Considerable research studies have been carried out on the development of models capable of predicting what happens at various stages of thermal stress development. Thermal stress, due to the developing of temperature field in a uniformly heated pipe from an external source was investigated numerically [92]. It was shown that the pipe wall thickness and diameter were significant parameters affecting the resulting stress distribution. It was also indicated that the stress ratio at the inner pipe radius reached a maximum for all axial planes and reduced to a minimum with increasing radius, which was contributed to the temperature gradient variation in the pipe wall. Moreover, it was also stated that the stress ratio increased when the thickness of the wall increased. The fracture toughness changes in composites based on tetragonal zirconia of alumina and the connection with the differences in stress level in the material was investigated experimentally and numerically [93]. It was shown that the effective improvement of fracture toughness in the alumina-based composites was larger than in the zirconia-based composites, which contributed to the stress state in the material due to the influence of crack type.

A study of residual stresses and distortion in cylindrical samples of spring steel, quenched in an oil bath at different temperatures was conducted numerically [94]. The study was performed to assess residual stress and distortion during heat treatment. It was shown that oil quenchants produced no residual stress after heat treatment, but water quenching generated high levels of stress. A series of rectangular repair welds of letterbox plates made from S690 steels, were investigated experimentally, to validate the numerical modeling techniques used in the determination of the residual stresses generated during repair process [95]. The repair welds were modeled using ABAQUS code software while the experimental work was done using the deep hole drilling technique. Comparison of the predictions and experimental results made on the parents' plate during welding were found to be in good agreement.

Reduction of thermally induced stress in a solid disk heated with radially periodic expanding and contracting ring heat flux by subsequent cooling of the heated segments was considered [96]. The study showed that the increase of coolant heat transfer coefficient lowers both the temperature and thermal stress distribution profiles, peaking at the extremities. It was also reported, that the subsequent cooling process significantly lowers the levels of temperature in the disk. A numerical study of the thermal stress developed in a fully developed laminar flow pipe was performed [97]. It was shown that low Pr number and low thermal conductivity ratios resulted in low radial effective stresses, and that the radial stress generated in the inlet plane of the pipe was higher compared to the corresponding stresses in the axial direction. The development of a finite element model, with emphasis on the guidelines for input parameters such as the corners enhanced strength, initial geometric imperfections and the significance of the residual stresses was conducted [98]. It was shown that from the different grades and shapes modeled, that the press-baked and roll-formed stainless steel cross-sections produced the closest predications to the experimental tests. Also it was found that the observed thermal residual stresses had no significant effect on stub column resistance.

An investigation of the thermal stress induced by temperature difference in tube-sheet of heat transfer equipment using FEM to compute the temperature and the stress fields was conducted numerically, focusing on the effect of tube sheet thickness on the thermal stress [99]. It was found that the thermal stress level was rather significant due to the temperature difference between the upper and lower surfaces and the thickness of the tube. Reduction of the thermal stress was achieved by reducing the tube thickness through adapting a flexible thin tube sheet. A deep-hole method for measuring the residual stress in large metallic components was extended, to allow for the measurements of residual stresses in thick section composite laminated plates, using experimental and numerical techniques [100]. It is concluded that the deep-hole method relies in its formulation on a calculation of the distortion of a hole in a plate subjected to remote loading, and suitable closed-form solutions existed for the isotropic material, but for orthotropic material finite element approach is employed.

The thermal stress due to thermal shock was investigated experimentally by three methods; temperature distribution measurement, strain gauge, and via FEM analysis [101]. It was shown that when the material with large anisotropy was subjected to thermal shock, the thermal stress value measured by strain gauge method was about 16% higher than the value measured by temperature method, but if the material investigated had a small anisotropy degree, the difference between the two techniques was as small as 4%, and this result was confirmed by FEM method. Investigation of the residual stress redistribution due to long-term creep tests at elevated temperature was carried out [102]. Residual stresses were measured on the AR pipes before and after post-weld heat treatment conditions and the data collected were used to validate the finite element modeling. The results obtained from all the different specimens clearly indicated that there was a need to account for the residual stresses in the estimation of the effective applied stresses during creep.

The strain gauge thermal effects during residual stress hole drilling measurements

were investigated, to evaluate the heat flux from the drilling tool to the sample in which the hole is drilled, and to evaluate the residual stress [103]. It was shown that the thermal strain produced by the drilling tool can be a substantial source of errors in the drilling residual stress measuring method if they are not considered. Thermal residual stresses in brush-plated coatings were investigated numerically [104]. It was shown that the stress present in the nickel deposits had a lower stress level than in copper deposits, mainly due to the coefficient of thermal expansion of nickel being closer to that of the steel substrate. It was also noted that the significant increase of the residual stress within the substrate was due to the increase of the coating thickness.

2.5.2 Residual Stress

The residual stress variation in high strength steels due to hydrogen embrittlement was investigated earlier using (XRD) technique [105]. It was shown that the XRD residual stress determination technique was able to detect hydrogen embrittlement in high strength steel. The thermal residual stresses in hard metal alloys such as Tungsten Carbides and Cobalt (WC-Co) arise during cooling due to pronounced difference in the thermal expansion coefficients was investigated analytically by XRD [106]. It was shown that the measured stresses agreed with the calculated results in all range under investigation. The results also, showed that the thermal residual micro- stresses in the centre of a large hard metal piece were more than the stresses on its surface by approximately 1.8 times

The remaining life for a hypothetical pressure vessel containing a defect subjected to thermal shock was examined [107]. Twelve cases of thermal shock loads of different severity were analysed by Finite Element Modeling (FEM). The estimation of remaining life for each case was carried out based on British Standards (PD6493) defect assessment procedure. It was found that more severe thermal shocks accelerate crack growth while less severe shocks may lead to slow

growth or eventual crack arrest.

Experimental Studies

The mean values of internal stresses in various steels which were subjected either to extension deformation or to overall reduction were investigated experimentally [108]. It was shown that an improved agreement between the average stress and the actual stress would be reached for samples with higher residual stresses, otherwise for samples with relatively low residual stresses, grain boundaries and carbide inclusions were likely to make a substantial contribution to the accuracy of the results. Residual stresses in various Depleted Uranium (DU) coatings were investigated experimentally [109]. The study was focused on thick DU coatings and included the stress evaluation as a function of applied negative bias voltage and film thickness. SEM was used to determine the coating thickness and the surface roughness. It was shown that, the stress measured was always compressive, however, increasing the coating thickness and adding bias voltage showed a trend towards more tensile stresses.

The problem of residual stress formation in spiral welded tubes during manufacturing was investigated experimentally [110]. The hole-drilling strain gauge method was used for the residual stress measurements. The residual stress was found to be higher than the yield point of the material at the weld neighborhood locations for tubes. Moreover, the tubes showed significant reduction in residual stress after pressure testing, while an annealing process performed on the tubes reduced the residual stress level at the weld neighbourhood locations. The ability of elastoplastic model, to predict the distribution of strains for duplex stainless steel, was investigated to assess the influence of initial residual stresses on the mechanical behaviour of stainless steel during tension and compression tests [111]. It was shown that the ferritic phase was initially harder than the austenitic phase, and the yield stresses of the phases within the duplex steel were affected not only by the critical resolved stresses of crystallites, but also

by the initial residual stresses that existed within the material. Residual stresses in surface-treated metals were investigated experimentally using laser-ultrasonic spectroscopy [112]. The experimental results obtained showed, that it was feasible to observe a substantial and highly characteristic change in the velocity of surface acoustic wave, when the specimen was heat treated at different annealing temperatures.

Analytical Studies

A method for estimating the influence of elastic gradients on the residual stress state of Functionally Graded Materials (FGM) was considered earlier [113]. Analytical thermal stress solutions as well as finite element calculations were used with two different approaches for the Finite Element (FE) model study. The study showed that for FGM films the results of approximation were similar to the predications of the exact solution. Residual stresses developed in the substrate material during machining were investigated numerically and experimentally [114]. It was shown that a developed new model allowed prediction of residual stresses within reasonable time and with acceptable accuracy as defined by the authors.

2.5.3 Summary

No reports related to the iron-base superalloy A286 thermal response to heat transfer, under turbulent flow situations, could be identified in the above open literature surveyed. On the metallurgy side, the few reports identified referring to the A286, were not in relation to its use at elevated temperature, in gas turbine engine applications. Additionally, assessment of the thermally induced stress development (due to flow situation and heat transfer) in the A286 alloy has not been investigated before either numerically or experimentally. Moreover, in spite of wide use of A286 iron-base superalloy in the gas turbine industry, no attempt was made to link the flow situation, heat transfer and induced thermal stress

assessment in A286 alloy parts used in gas turbine application, to in-service situations.

Work undertaken in this research has not been reported on before. It is an attempt to overcome the gaps identified in literature (available in the public domain) regarding the usage of the iron-base superalloy A286, at elevated temperature in aero-derivative gas turbine applications.

This is research is important due to the unique and specific typical operating conditions of the transition-piece, in the aero-derivative gas turbine engines, in mechanical drive applications. Information reported in open literature related to flow situations and thermal stresses is considered useful input to improve present work and present applications. Although thermal stresses in metallic parts have been reported on earlier studies, the flow situation resembling the flow structure and thermally induced stresses in transition-pieces made of A286 iron-base superalloy were not examined before. Therefore, investigation of the flow structure and thermal stress field in the transition-piece, which is pertinent to the actual operating conditions, becomes necessary.

3

MATHEMATICAL MODELING

3.1 HEAT TRANSFER NUMERICAL SIMULATION

3.1.1 Introduction

Mathematical modelling of the flow field, resembling the actual flow into a transition-piece, with the relevant boundary conditions is presented in this chapter. Heat transfer calculations within the outer casing wall of the transition-piece are formulated in relation to actual airflow situation. Thermal stress analysis associated with the temperature rise in the outer wall casing of the transition-piece is introduced and relevant boundary conditions are stated.

3.1.2 Flow Equations and Turbulence Model

The governing flow and energy equations for a steady flow in a transition-piece can be written in the Cartesian tensor notation as follows;

The continuity equation is;

$$\frac{\partial}{\partial x_i}\left(\rho U_i\right)=0 \qquad (3.1)$$

The momentum equation is;

$$\frac{\partial}{\partial x_i}\left(\rho U_i U_j\right) = -\frac{\partial p}{\partial x_j} + \frac{\partial}{\partial x_i}\left[\mu\left(\frac{\partial U_i}{\partial x_j} + \frac{\partial U_j}{\partial x_i}\right) - \rho\overline{u_i u_j}\right] \tag{3.2}$$

The energy equation is;

$$\frac{\partial}{\partial x_i}\left(\rho U_i c_p T\right) = \frac{\partial}{\partial x_i}\left(\frac{\mu}{\sigma}\frac{\partial T}{\partial x_i} - \rho c_p \overline{u_i \theta}\right) + \overline{S_T} \tag{3.3}$$

To account for the turbulence in the flow field the standard "$\kappa - \varepsilon$" model was used [115].

3.1.3 Equations Governing the Turbulence Model

The "κ-ε" model focuses on the mechanisms that affect the turbulent kinetic energy. This model is based on the presumption that an analogy exists between the action of the viscous stresses and Reynolds stresses on the mean flow. It is experimentally observed that turbulence decays unless there is a shear in the flow field. Furthermore, turbulent stresses are found to increase as the mean rate of deformation increases. It was proposed by Boussinesq in 1877 that Reynolds stresses could be linked to mean rates of deformation. To compute the Reynolds stresses with the "κ-ε" model an extended Boussinesq relationship is used;

$$-\rho\overline{u_i u_j} = \mu_t\left(\frac{\partial U_i}{\partial x_j} + \frac{\partial U_j}{\partial x_i}\right) - \frac{2}{3}\rho\kappa\delta_{ij} \tag{3.4}$$

The extra term on the right hand side which involves "δ_{ij}" make the formula applicable to the normal Reynolds stresses. The pressure p is replaced by the effective pressure "$p + \left(\frac{2}{3}\right)\rho\kappa$", to include this contribution from the normal

stresses. Turbulent transport of other scalar properties is modeled similarly. By analogy with equation 3.4, turbulent transport of a scalar is taken to be proportional to the gradient of the mean value of the transported quantity,

$$-\overline{\rho u_i \phi'} = \Gamma_t \frac{\partial \phi}{\partial x_i} \tag{3.5}$$

where "Γ_t" is the turbulent diffusivity. Since turbulent transport of momentum and heat is due to the same mechanism, eddy mixing, it is expected that the value of the turbulent diffusivity "Γ_t" is close to that of the turbulent viscosity "μ_t" it is usual to write "$\Gamma_t = \frac{\mu_t}{\sigma_t}$". Experiments in many flows have established that "σ_t" is around 1 [115].

The "κ-ε" model allows for the effect of transport turbulence properties by the mean flow and diffusion, and for the production and destruction of turbulence. Two transport equations, one for the turbulent kinetic energy κ and one for the rate of dissipation of turbulent kinetic energy ε, are solved. The underlying assumption of this model is that the turbulent viscosity "μ_t" is isotropic, in other words that the ratio between Reynolds stresses and mean rate of deformation is the same in all directions.

3.1.4 The Eddy Viscosity Hypothesis

On dimensional grounds it is assumed that the kinematics turbulent viscosity "ν_t", can be expressed as a product of a turbulent velocity scale "ϑ" and length scale l, then

$$\mu_t = c_p \vartheta l \qquad (3.6)$$

Using the following functions of "κ" and "ε" to define velocity scale and length scale which are representative of the large scale turbulence.

$$\vartheta = \kappa^{\frac{1}{2}} \qquad l = \frac{\kappa^{\frac{3}{2}}}{\varepsilon}$$

The eddy viscosity is specified as follows,

$$\mu_t = C_\mu \rho \frac{\kappa^2}{\varepsilon} \qquad (3.7)$$

3.1.5 Governing Equation for Turbulent Kinetic Energy (κ) and the Dissipation of Turbulent Kinetic Energy (ε)

Multiplication of each of the instantaneous Navier-Stokes equations by the appropriate fluctuating velocity components, and addition of all the results, followed by a repeat of this process on the Reynolds equations, subtraction of the two resulting equations and very substantial re-arrangement yields the equation for turbulent kinetic energy "κ":

$$\frac{\partial}{\partial x_i}\left(\rho U_i \kappa\right)=\underbrace{\frac{\partial}{\partial x_i}\left[\mu\frac{\partial \kappa}{\partial x_i}-\left(\overline{\rho' u_i}+\rho\frac{1}{2}\overline{u_i u_j u_j}\right)\right]}_{d_\kappa}\underbrace{-\rho\overline{u_i u_j}\frac{\partial U_i}{\partial x_j}}_{P_{\kappa\kappa}}\underbrace{-\mu\overline{\frac{\partial u_i}{\partial x_j}\frac{\partial u_i}{\partial x_j}}}_{\rho\varepsilon} \qquad (3.8)$$

The term "$P_{\kappa\kappa}$" gives a positive contribution in this equation and represents a production term. The viscous dissipation term "$\rho\varepsilon$"gives a negative contribution due to the appearance of the sum of squared fluctuating deformation rates. The dissipation of turbulent kinetic energy is caused by work done by the smallest eddies against viscous stresses. The rate of dissipation per unit mass, whose dimensions are "$\frac{m^2}{s^2}$" is of vital importance in the study of turbulence dynamics and is denoted as, $\varepsilon=-\nu\overline{\frac{\partial u_i}{\partial x_j}\frac{\partial u_i}{\partial x_j}}$. It is always the main destruction term in the turbulent kinetic energy equation, of a similar order of magnitude to the production term and never negligible.

The transport equations for κ and ε are [115]:

$$\frac{\partial}{\partial \chi_i}\left(\rho U_i \kappa\right)=\frac{\partial}{\partial \chi_i}\left[\left(\frac{\mu_t}{\sigma_\kappa}\right)\frac{\partial \kappa}{\partial \chi_i}\right]+P_{\kappa\kappa}-\rho\varepsilon \qquad (3.9)$$

and

$$\frac{\partial}{\partial \chi_i}\left(\rho U_i \varepsilon\right)=\frac{\partial}{\partial \chi_i}\left[\left(\frac{\mu_t}{\sigma_\varepsilon}\right)\frac{\partial \varepsilon}{\partial \chi_i}\right]+\frac{\varepsilon}{\kappa}\left(C_1 P_{\kappa\kappa}-C_2\rho\varepsilon\right) \qquad (3.10)$$

The model contains six empirical constants which are assigned the following values [116]

C_μ	C_1	C_2	σ_κ	σ_ε
0.09	1.44	1.92	1.00	1.30

Table 1, constants employed in the κ-ε model

The production term "$P_{\kappa\kappa}$" is derived from the exact production term in (3.8) by using (3.4) and is given by:

$$P_{\kappa\kappa} = \mu_t \left[\left(\frac{\partial U_i}{\partial \chi_j} + \frac{\partial U_j}{\partial \chi_i} \right) \frac{\partial U_i}{\partial \chi_j} \right] \qquad (3.11)$$

The right hand sides of equations 3.9 and 3.10 are the modeled form of the principal transport processes. The turbulent transport terms are represented using the gradient diffusion hypothesis of the form equation 3.5. Prandtl numbers "σ_K" and "σ_ε" connect the diffusivities of "κ" and "ε" to the eddy viscosity "μ_t". Upon performing an order of magnitude analysis, it can be shown that the first element of the diffusion part "d_κ" in equation 3.8 (i.e. the viscous transport of κ) becomes negligibly small with respect to other terms when the Reynolds number is sufficiently high, and is therefore neglected with respect to the other elements of the diffusion term [115]. Also, the pressure term appearing in "d_κ" in equation 3.8 cannot be measured directly. Its effect is accounted for in the modeled equation 3.9 within the gradient diffusion term.

Production and destruction of turbulent kinetic energy are always closely linked. The dissipation rate "ε" is large where the production of "κ" is large. The model equation 3.10 for ε assumes that its production and destruction terms are proportional to the production and destruction terms of the "κ" equation 3.9.Adoption of such forms ensures that "ε" increases rapidly if "κ" increases

rapidly and that it decreases sufficiently fast to avoid (non-physical) negative values of turbulent kinetic energy if "κ" decreases. The factor "$\frac{\varepsilon}{\kappa}$" in the production and destruction terms makes these terms dimensionally correct in the "ε" equation.

3.1.6 Wall Function for Standard κ-ε Model

As mentioned before an assumption in equations 3.9 and 3.10 implies that "$\mu_t >> \mu$". This is clearly invalid close to a solid wall where the turbulent fluctuations are suppressed by the presence of a viscous sub layer very near the wall. Therefore, adjacent to walls special wall functions are introduced that typically assume a logarithmic dependence of the tangential velocity component on the normal coordinate. If "z" is the co-ordinate direction normal to a solid wall, the mean velocity at point "z_p" with "$30 < z_p^+ < 500$"satisfies the law [115]:

$$U_p = \frac{U^*}{\kappa} \ln\left(\chi z_p^+\right)$$

In addition measurements of turbulent kinetic energy budget indicate that the production of turbulent kinetic energy is equal to the dissipation in the log-law region. Using these assumptions and the eddy viscosity equation 3.7 provide the following wall boundary conditions for "κ" and "ε";

$$\kappa = \frac{U^{*2}}{\sqrt{C_\mu}} \qquad \text{and} \qquad \varepsilon = \frac{U^{*3}}{\kappa z} \qquad (3.12)$$

Where U^*, and z_p^* are the friction velocity and dimensionless distance from point p to the solid wall. These are defined as follows:

$$U^* = \left(\frac{\tau_w}{\rho}\right)^{\frac{1}{2}} \quad \text{and} \quad z_p^+ = \frac{\rho z_p U^*}{\mu} \tag{3.13}$$

Where " τ_W" is the shear stress at the wall, "κ" is the Von Karaman constant, "χ" is the roughness parameter and "Z_p" is the actual distance from the point "p" to the solid wall.

3.1.7 Generalized Wall Functions for Normal and Shear Turbulent Stresses

For cases very near to the wall, the mean velocity vector undergoes a rapid change in direction with distance from the wall; the wall-functions approach is not successful in reproducing the details of the flow. Therefore, reference is made to the case where the turbulent stresses and fluxes at the near wall grid points are calculated directly from their transport equations.

This approach is based on the assumption that the near-wall region lying between the wall and the near-wall computational node at z_p may be represented by two layers; the fully viscous sublayer, defined by "$\mathrm{Re}_\upsilon = z_\upsilon \frac{\sqrt{\kappa_\upsilon}}{\nu} \cong 20$", and a fully turbulent layer above it conforming to the logarithmic-velocity law [116]. On the assumption that local equilibrium prevails in the turbulent layer (i.e. production equals dissipation for the turbulent kinetic energy), the above implies [117],

$$\frac{\frac{U_p}{\tau_w}}{\rho} C_\mu^{\frac{1}{4}} \sqrt{\kappa_p} = \frac{1}{\kappa} \ln\left(\chi z_p \frac{C_\mu^{\frac{1}{4}} \sqrt{\kappa_p}}{\nu}\right) \tag{3.14}$$

which yields, the wall shear stress near the wall as follows:

$$\overline{\upsilon w}\Big|_{z\upsilon} = \frac{\tau_w}{\rho}$$

This serves as the boundary condition for "$\overline{\upsilon\omega}$" transport equation. A similar condition can be found for "$\overline{uw}$" equation, while "$\overline{u\upsilon} = 0$" serves as the boundary condition for the related equation. Regarding normal stresses, the turbulence energy must decay quadratically towards a value of zero at the wall, so that a zero-gradient condition for normal stresses is physically realistic [118]. This condition however is insufficient to ensure an accurate numerical representation of near-wall effects. Thus additional measures are required to account for the very steep variations of turbulence properties within the near-wall cells. Specifically, a more precise approach to that adopted in internal cells is needed in respect of evaluating volume-integrated production and dissipation of normal stresses (these are normally evaluated at cell centers, using linear interpolation, and then multiplied by the cell volume). Taking "$\overline{u^2}$" as an example, since the near-wall flow is very nearly of the Couette type, the volume-integrated production of "$\overline{u^2}$" between the wall and the O-node may be approximated by:

$$\int_{\Delta x}\int_{0}^{z_o} P_{11} d\forall \cong \int_{\Delta x}\int_{0}^{z_o} \overline{uw}\frac{\partial U}{\partial z}\partial z = \frac{2\tau_w}{z_o}(U_o - U_v)\Delta x \qquad (3.15)$$

where "U_o" and "U_υ" follow from the log-law, equation 3.14. no contribution arises from the viscous sublayer since "$\overline{u\omega} = 0$" in this layer. An analogous integration of the dissipation rate with the assumption,

$$\varepsilon = \frac{2\nu\kappa_{\upsilon}}{z_{\upsilon}^2} \qquad 0 \le z \le z_{\upsilon}$$

$$\varepsilon = \frac{C_{\mu}^{\frac{3}{4}}\kappa_{o}^{\frac{3}{2}}}{\kappa z_{\upsilon}} \qquad z_{\upsilon} \le z < z_{o}$$

Leads to;

$$\int_{\Delta X}\int_{0}^{Z} p\varepsilon d\forall \cong \left[\frac{2\nu\kappa_{o}}{z_{\upsilon}} + \frac{C_{\mu}^{\frac{3}{4}}\kappa_{o}^{\frac{3}{2}}}{\kappa}\ln\left(\frac{z_{o}}{z_{\upsilon}}\right)\right]\Delta x \qquad (3.16)$$

An analogous treatment is applied to "$\overline{\upsilon^2}$", while the production of "$\overline{w^2}$" in the viscous and turbulent near wall layers region is zero.

The values resulting from equations 3.15 and 3.16 are added, respectively, to the volume-integrated generation and dissipation computed for the upper half of the near-wall volume, as if this belonged to an ordinary cell.

The final point to note in respect of the wall-law approach is that the near-wall dissipation "ε_o" is not determined from its differential equation applied to the near-wall cell surrounding the node. Instead, and in accordance with the log law, this value is obtained via the length scale from;

$$\varepsilon_{o} = \frac{C_{\mu}^{\frac{3}{4}}\kappa_{o}^{\frac{3}{2}}}{\kappa z_{o}}$$

This serves as the boundary conditions for inner cells.

3.2 The Numerical Technique

A preliminary idea about the task of a numerical method can be obtained by considering a flow situation. A grid is drawn to cover the flow domain and with a sufficiently fine grid, the complete distributions of the relevant variables can be expressed in terms of their values at the grid points. Thus, the task of a numerical method is to evaluate velocity, pressure, temperature or other variables at the chosen grid points. From the differential equations governing the relevant variables, algebraic equations are derived for the grid-point values of the variables.

3.2.1 Control Volume Approach

The particular practice that was chosen for the derivation of the discretisation equations is the control volume approach. The calculation domain is divided into sub-domains or control volumes such that there is one control volume around a grid point. The differential equation is integrated over the control volume to yield the discretisation equation. Thus, the discretisation equation represents the same conservation principle over a finite region as the differential equation does over an infinitesimal region. This direct interpretation of the discretisation equation makes the method easy to understand in physical terms; the coefficients in the equation can be identified, even when they appear in a computer program, as familiar quantities such as flow rates, areas, volumes, and diffusivities. The control – volume approach can be regarded as a special case of the method of weighted residuals, in which the weighting function is chosen to be unity over a control volume and zero everywhere else. The main reasons for choosing the control-volume formulation are its simplicity and easy physical interpretation [119].

3.2.2. Discretisation

In focusing the attention on the values at the grid points, the continuous information contained in the exact solution of the differential equation was replaced with discrete values. The algebraic equations involving the unknown

values of "ϕ" at the chosen grid points (i.e. discretisation equations), are derived from the differential equations governing "ϕ". Piecewise profiles are usually used to express how "ϕ" varies between the grid points, each segment of the piecewise profile describes the variation of "ϕ" over only a small region in terms of the "ϕ" values at the grid points within and around the region. The steady state diffusion in a two-dimensional situation is governed by the following equation [120];

$$\frac{\partial}{\partial x}\left(\Gamma\frac{\partial\phi}{\partial x}\right)+\frac{\partial}{\partial y}\left(\Gamma\frac{\partial\phi}{\partial y}\right)+S=0 \qquad (3.17)$$

A two-dimensional grid is used to subdivide the domain (Figure 6). A cell containing node "O" has four neighboring nodes identified as west, east, south, and north nodes "W, E, S, N", the notation, w, e, s, and n, are used to refer to west, east, south, and north cell faces respectively. Integration of equation 3.17, over the control volume in Figure 6 gives;

$$\left[\Gamma_e A_e\left(\frac{\partial\phi}{\partial x}\right)_e-\Gamma_w A_w\left(\frac{\partial\phi}{\partial x}\right)_w\right]+\left[\Gamma_n A_n\left(\frac{\partial\phi}{\partial y}\right)_n-\Gamma_s A_s\left(\frac{\partial\phi}{\partial y}\right)_s\right]+\bar{S}\Delta V=0 \qquad (3.18)$$

Now discretisation from equation 3.18 can be obtained;

$$\left[\Gamma_e\frac{\left(\phi_e-\phi_o\right)A_e}{\delta x_{oe}}-\Gamma_w\frac{(\phi_o-\phi_w)A_w}{\delta x_{wo}}\right]+\left[\Gamma_n\frac{(\phi_n-\phi_o)A_n}{\delta y_{on}}-\Gamma_s\frac{(\phi_o-\phi_s)A_s}{\delta y_{so}}\right]+\bar{S}\Delta V=0 \qquad (3.19)$$

By re-arranging the above, the discretised equation for interior nodes:-

$$a_o\phi_o = a_w\phi_w + a_e\phi_e + a_s\phi_s + a_n\phi_n + S_u \qquad (3.20)$$

Where;

a_W	a_E	a_S	a_N	ao
$\frac{\Gamma_w A_w}{\delta x_{WP}}$	$\frac{\Gamma_e A_e}{\delta x_{oe}}$	$\frac{\Gamma_s As}{\delta y_{so}}$	$\frac{\Gamma_n A_n}{\delta y_{on}}$	$a_w + a_e + a_s + a_n - S_o$

Table 2, discretisation constants definition

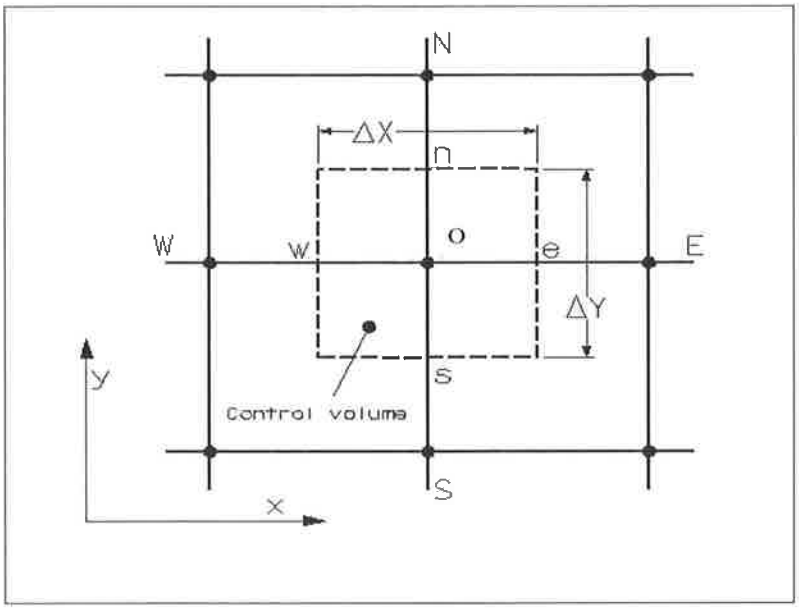

Figure 6, Schematic view of control volume for two-dimensional grid

3.2.3 Calculations of the Flow Variables-The SIMPLE Algorithm

If the pressure field which appears as a major part of the source term, for the momentum equations is assumed, then the following equation;

$$(A_o - So)\phi_o = A_n\phi_n + A_s\phi_s + A_e\phi_e + A_w\phi_w + A_o^0\phi_o^0 + S_0 \tag{3.21}$$

Where $A_p = \sum_n A_n \quad A_p^0 = \frac{\rho_p^0 \Delta V}{\Delta t}$, which is written for each grid node, yields a closed set of algebraic equations, but there is no guarantee that the resultant velocity would satisfy the continuity relation. The two problems of determining the pressure and satisfying continuity are overcome by adjusting the pressure field so as to satisfy continuity. A staggered grid arrangement is used in which the velocities are stored at a location midway between the grid points (i.e. on the control volume faces). All other variables including pressure are calculated at the grid points. This arrangement gives a convenient way of handling the pressure linkages through the continuity equation and is known as the Semi-Implicit Method for Pressure –Linkage Equations (SIMPLE) algorithm. This method is an iterative process to convergence. The mathematical development of this procedure focuses on providing a pressure link between continuity and momentum. This is accomplished by transforming the continuity equation into a Poisson equation for pressure. The Poisson equation implements a pressure correction for a divergent velocity field. The staggered grid arrangement is employed to compensate for non-physical oscillations manifested in the pressure distribution. These oscillations are due to a physical decoupling of the local pressure distribution from the local velocity field, as the pressure gradient in the momentum equations is discretized by central differences. The steady-state convergence is achieved by successively predicting and correcting the velocity components and pressure variable. An initial estimate for the pressure variable at each grid point is required.

Equation 3.21 with the pressure gradient separated out from the source term can be rewritten for the U velocity at the node "e" for example as,

$$\left(A_e - S_e^*\right)U_e = \Sigma A_{nb} U_{nb} + S_0^* + \left(O_o - O_e\right)\Delta\xi_{2e} \qquad (3.22)$$

If "$p^{\dagger}$" represents an assumed pressure at node "o" and "$U_e^{\dagger}$" and "$V_e^{\dagger}$" represents the corresponding velocities calculated by equations similar to equation 3.22, then we can write for the actual pressure;

$$p = p^{\dagger} + p' \qquad (3.23)$$

Here "p'" represents a pressure correction. Consequently, a velocity–correction formula for velocity at node "e" for example can be written as;

$$U_e = U_e^{\dagger} + \frac{\Delta\xi_{2e}}{A_e}\left(p_o' - p_e'\right) \qquad (3.24)$$

In this expression certain assumptions have been made therefore "U_e" does not represent the exact value.

An equation very similar to equation 3.21 can now be written for "p'" by the discretisation for the continuity equation;

$$\left(A_o - S_o\right)p_o' = \Sigma A_{nb} p_{nb}' + S_o \qquad (3.25)$$

The solution for the finite-difference equations proceeds by the cyclic repetition of the following steps:

a. Provide initial estimates of the values of all the variables including pressure $p^{\dagger}$
b. Solve the momentum equations like equation 3.22 to obtain $U^{\dagger}$, and $V^{\dagger}$.

c. Solve the pressure-correction equation 3.25 to obtain "p'".

d. Calculate the pressure p from equation 3.23 and corrected velocities U, V from equations like equation 3.24

e. Solve the equations of the form 3.25 for all other dependent variables

f. Regard the new values of the variables as improved estimates and return to step (a)

g. Repeat until convergence [115]

3.2.4 The SIMPLEC Algorithm

The SIMPLEC (SIMPLE-Consistent) algorithm of Van Doormal and Raithby (1984) follows the same steps as the SIMPLE algorithm in the above section, with the difference that the momentum equations are manipulated so that the SIMPLEC velocity correction equations omit terms that are less significant than those omitted in SIMPLE. The u-velocity correction equation of SIMPLEC is given by:

$$u'_{i,j} = d_{i,j}\left(p'_{I-1,j} - p'_{I,j}\right) \tag{3.26}$$

Where;

$$d_{i,j} = \frac{A_{i,J}}{a_{i,J} - \sum a_{nb}} \tag{3.27}$$

Similarly the modified v - velocity correction equation is;

$$v'_{I,J} = d_{I,J}\left(p'_{I,J-1} - p'_{I,J}\right) \tag{3.28}$$

Where;

$$d_{I,J} = \frac{A_{I,j}}{a_{I,j} - \sum a_{nb}} \tag{3.29}$$

The discretised pressure correction equation is the same as in SIMPLE, except that the d-terms are calculated from equations 3.27 and 3.29. The sequence of operations of the SIMPLEC algorithm is identical to that of SIMPLE algorithm [115].

3.3 The Two-Dimensional Axisymmetric Transition- Piece Geometric Configuration

The computations were performed for a semi-rectangular box-shaped two dimensional domain (Figure 7). The grid used for the simulation was non-uniform to increase the resolution in the regions of large temperature gradients near the wall-fluid interface area.

It can be seen that the flow field has axial symmetry through the transition-piece centre. The calculations domain is therefore chosen to extend from the symmetry plane to a location representing where the outer transition-piece wall is in contact with the atmospheric conditions in the y-axis direction. In the x- axis the computation domain extends from the (0, 0) point representing the exit of the gas turbine low pressure turbine section and the inlet of the transition-piece, while the computation domain end is at the point (0, 0.368) representing the end of the transition-piece and the entrance to the power turbine. Table 3, shows the computation domain dimensions.

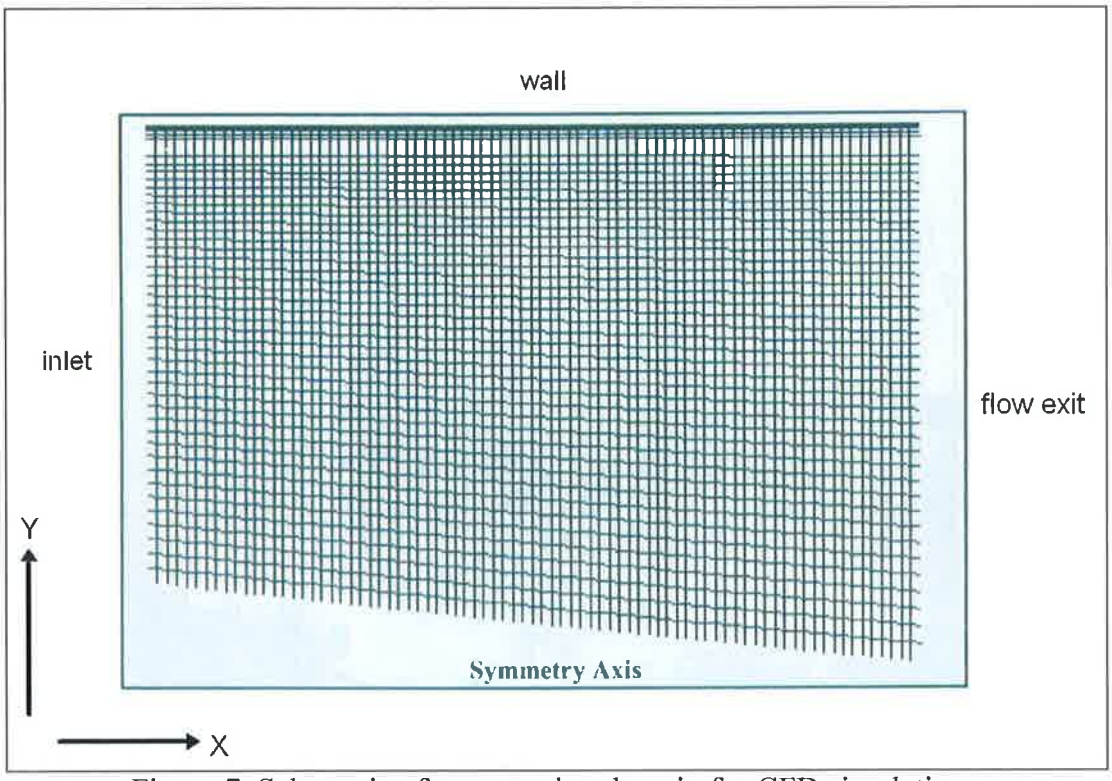

Figure 7, Schematic of computation domain for CFD simulation

	X- Direction (m)	Y-Direction (m)	Z-Direction (m)
Inner Cone (Solid Zone)	0.368	0.207	0
Flow Field (Fluid Zone)	0.368	0.4545	0
Outer Wall (Solid Zone)	0.368	0.465	0

Table 3, Computation Domain Dimensions

3.3.1. Computational Grid and Boundary Conditions

To complete the problem statement, the boundary conditions must be incorporated into the control volume method. The boundary conditions considered for the flow zone are mass –flow inlet, pressure outlet, solid walls with no slip condition for the flow side. Symmetry boundary conditions were used at the transition-piece centerline axis and y = 0 is the symmetry plane for the 2D calculations as shown in table 4, along with divisions generated in each sub-domain for the grid generated in the control volume for the conjugated problem in Figure 7 .

Variable	Divisions		Boundary	Type
X Direction	80		Flow Inlet	Mass-flow-inlet
Y Direction	Inner Cone	24 (30%)	Flow Outlet	Pressure-outlet
	Flow Field	40 (50%)	Case Rear Wall	Wall
	Outer Wall	14 (20%)	Case Front Wall	Wall
			Centerline	Axis
			Exhaust Pipe	Fluid

Table 4, Boundary conditions definition

For the solid side of the transition-piece (i.e. walls) the boundary conditions used were wall with temperature profile through user defined function, for the front face of the transition-piece wall, to take into account the heat spread from the hot section of the engine. For the rear wall, a heat transfer coefficient was calculated and applied to prevent the duct wall from being heat sink while a free stream with temperature of 300 K, in addition to the calculated heat transfer coefficient was applied. The bottom (lower) surface of the duct wall was coupled to the exhaust gas inside the duct.

The numbers of divisions in the different planes of the domain were distributed to achieve the maximum effectiveness where the conjugate interaction occurs (i.e. at the transition-piece outer wall) as follows; the Inner cone is 30% of the total number of the divisions and successive ratio of 1.0.The flow field domain had 40 divisions with a successive ratio of 0.98201m resulting in a concentration of cells near and at the wall. The casing outer wall grid spacing in the X-direction was adjusted to maintain a constant ratio of any two adjacent spacing. In the Y-direction it was designed to be a non-uniform grid, with a gradually decreasing spacing away from the hot exhaust gases towards the atmospheric conditions, a thickness of 14 and a successive ratio of 0.596 thus making the flow field total number of nodes 6557.

3.3.2 Derivation of the Boundary Conditions for the Outer Wall

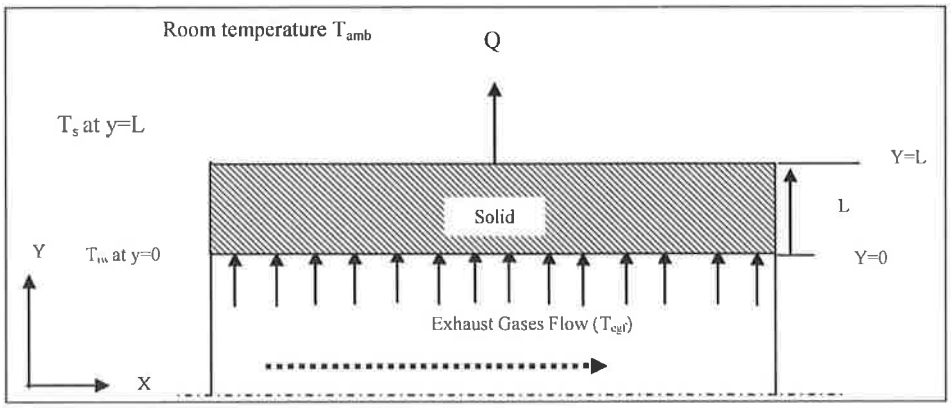

Figure 8, Schematic diagram of the transition-piece outer casing wall

The derivation of the boundary conditions is carried out under the following assumptions;

- The inner wall temperature (at Y=0) is equal to the exhaust gas temperature;

$$T_{iw} = T_{egf}$$

- The room temperature $T_{amb.}$
- The casing outer wall temperature (at Y=L);

$$T = T_S$$

The above can be simulated in one dimension as follows [121];

$$\frac{\partial}{\partial y}\left(K\frac{\partial T}{\partial y}\right) = 0 \qquad (3.30)$$

Integrating the equation 3.30 twice will result in;

$$T = \frac{C_1}{K}y + C_2 \qquad (3.31)$$

Two unknowns C_1 & C_2, two boundary conditions are needed

First boundary condition at y=0, where $T=T_{iw}$

$$C_2 = T_{iw} \tag{3.32}$$

From Figure (8)

$$C_1 = -h\left(T_s - T_{amb}\right) \tag{3.33}$$

Substitute equations 3.32 & 3.33 into equation 3.31

$$T = T_{iw} - \frac{h\left(T_s - T_{amb}\right)}{\kappa} y \tag{3.34}$$

Second boundary condition at y=L where $T=T_s$

$$T_s = \frac{\kappa T_{iw} + hT_{amb} L}{\kappa + hL} \tag{3.35}$$

Substitute equation 3.35 in equation 3.34;

$$T = T_{iw} - \frac{hy}{\kappa + hL}\left[\left(T_{iw} - T_{amb}\right)\right] \tag{3.36}$$

The temperature profile used, at the front face of the transition-piece wall, is calculated assuming the exhaust gas temperature inside the transition-piece "T_f" is equal to the temperature at the inner surface of the transition-piece "T_w". The calculation domain was approximated to a large plates with a turbulent fluid flowing over, for that estimating the heat transfer condition in that condition the below approximation is used [122];

$$h = 1.31 \times (\Delta T)^n \tag{3.37}$$

Using the above approximation produced;

$$h = 1.31 \times (904 - 300)^{0.33} = 10.84 \ W/m^2K \qquad (3.38)$$

where the exponent "n" can be classified as 0.33 for turbulent natural convection

The previous estimation of the heat transfer coefficient produced the linear equation 3.40 for the distribution of the temperature along the y-axis in the front wall of the transition-piece outer wall;

$$T = -268.48x + 904.15 \qquad (3.40)$$

where "x" is axial distance along the transition-piece length. The equation is fed to the simulation through a user defined function.

3.3.3 Simulation Conditions

The simulation of the exhaust gas flow inside the transition-piece is based on true data collected from gas turbine manufacturer [123-124] and actually measured data in the workshop. The initial conditions are imposed before the exhaust gases emerge into the transition-piece (i.e. the control domain).

3.3.4. Initial Conditions

The initial conditions used in the simulation are:

Initial Condition	Steady state (Base case)	+10% Flow	-10% Flow	+10% Temperature	-10% Temperature
Inlet Mass-Flow	180 kg/s	198 kg/s	162 kg/s	180 kg/s	180 kg/s
Inlet Temperature	904.15 K	904.15 K	904.15 K	994.6 K	813.7 K

Table 5, CFD simulation initial conditions

With the fluid and the transition-piece casing wall properties shown in tables 6 and 7 respectively;

Property	Unit	@904K & 272.412 KPa
Density (ρ)	Kg/m^3	1.055
Heat Capacity (C_p)	J/(mol.K)	1021.209
Thermal Conductivity (κ)	W/mK	0.023698
Viscosity (μ)	Kg/ms	8.825E-6
Gas Constant(R)	J/KgK	285.33

Table 6, Exhaust Gas Thermal properties used in the simulation.

Property	Unit	Value
Density (ρ)	Kg/m^3	7920
Heat Capacity (C_p)	J/kgK	460
Thermal Conductivity (κ)		
Temperature (K)	k (W/mK)	
294.15	12.6	
423.15	20.2	
698.15	20.2	
873.15	23.79	
923.15	24.7	

Table 7, Thermal properties of the transition-piece casing wall material

Due to the non equality introduced for the grid generated for the assessment, grid independent tests are performed in order to secure grid independent results. It may be observed that for a flow field domain of 80×78 cells, the outer case temperature resulted is almost the same as for 87 × 86 cells (20% increase in cells count) and

for 71 × 70 (20% decrease in cells count); where the difference is less than 1% as shown in Figure 9.

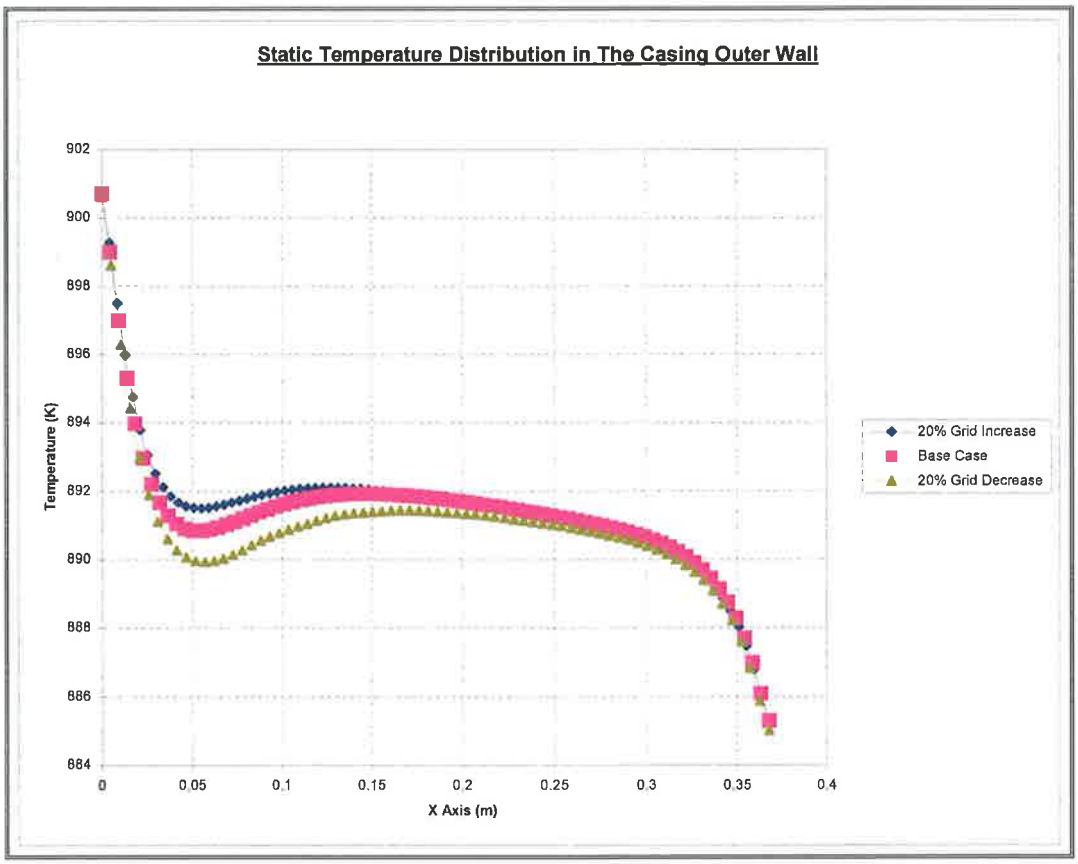

Figure 9, Static Temperature distribution Grid Validation

In the numerical simulations, the residuals were set as 10^{-6} for all the dependent variables, which provided the converge solutions.

3.4. Thermal Stress Analysis in the Transition-Piece

3.4.1. Thermal Stress Modeling

Thermal stresses are generated in the substrate due to the temperature gradient in the localized heated region due to the heat transferred from the hot gases. That can lead to the elastic-plastic displacement in the substrate material. The stresses are related to strains by [125];

$$\{\sigma\} = [D]\{\epsilon^e\} \tag{3.41}$$

Where $\{\sigma\}$ is the stress tensor, and $[D]$ is the elastic matrix.

$$\{\epsilon^e\} = \{\epsilon\} - \{\epsilon^{th}\} \tag{3.42}$$

Where $\{\epsilon\}$ is the total strain tensor and $\{\epsilon^{th}\}$ is the thermal strain vector.
Equation (3.41) may also be written as:

$$\{\epsilon\} = [D]^{-1}\{\sigma\} + \{\epsilon^{th}\} \tag{3.43}$$

Since the present case is axially symmetric, and the material is assumed to be isotropic, the stress-strain relationship can be written in cylindrical coordinates as;

$$\begin{aligned}
\epsilon_{rr} &= \frac{1}{E}\left[\sigma_{rr} - \nu\left(\sigma_{\theta\theta} + \sigma_{zz}\right)\right] + \alpha\Delta T(r,x,t) \\
\epsilon_{\theta\theta} &= \frac{1}{E}\left[\sigma_{\theta\theta} - \nu\left(\sigma_{rr} + \sigma_{zz}\right)\right] + \alpha\Delta T(r,x,t) \\
\epsilon_{zz} &= \frac{1}{E}\left[\sigma_{zz} - \nu\left(\sigma_{rr} + \sigma_{\theta\theta}\right)\right] + \alpha\Delta T(r,x,t) \\
\gamma &= \frac{1}{G}\tau
\end{aligned} \tag{3.44}$$

where E, υ and α are modulus of elasticity, Poisson's ratio, and linear coefficient of thermal expansion, respectively. $\Delta T(r,x)$ represents the temperature rise at a point (r,z) at time=t with respect to that at t = 0 corresponding to a stress free condition. A typical component of thermal strain from equation (3.44) is:

$$\begin{aligned}
\epsilon^{th} &= \alpha_T \Delta T(r,x) \\
&= \alpha_T\left(T_{(r,x)} - T_{ref}\right)
\end{aligned} \tag{3.45}$$

where T_{ref} is the reference temperature at t=0

When α is a temperature function, then equation (3.45) becomes;

$$\epsilon^{th} = \int_{T_{ref}}^{T} \alpha_T(T)dT \tag{3.46}$$

The present study uses mean or weighted-average value of α_T, such that;

$$\epsilon^{th} = \overline{\alpha_T}(T)\left(T - T_{ref}\right) \tag{3.47}$$

where $\overline{\alpha}(T)$ is the mean value of linear coefficient of thermal expansion and is given by;

$$\overline{\alpha_T}(T) = \frac{\int_{T_{ref}}^{T} \alpha_T(T)dT}{T(r,x) - T_{ref}} \tag{3.48}$$

3.4.2. Method of Solution

To develop a finite element procedure for stress computation, the standard displacement-based finite element method is normally used. The basis of this approach is the principle of virtual work, which states that the equilibrium of any body under loading requires that for any compatible small virtual displacement (which are zero at the boundary points and surfaces and corresponding to the components of displacement that are prescribed at those points and surfaces) imposed on the body, in its state of equilibrium, then the total internal virtual work or strain energy (δV), i.e. $\delta U = \delta V$.

The evaluation of the influence of elasticity and temperature on the computation of thermal stresses requires the use of thermo-mechanical analysis. Imposing the temperature field obtained from the numerical solution of the heat conduction equation, displacement and resulting stresses were calculated by Finite Element (FE) analysis. The FE analysis was conducted by the FE package ANSYS. The solid side of the solution domain representing the solid substrate was discretized into 900 eight-noded axisymmetric elements. The temperatures at the nodes were prescribed as body load. The test piece used in the 3-point bending experimental test was modeled using Plane 82, which is 8 nodes element that has compatible displacement shape and is well suited to model curved boundaries. The Plane 82 is defined by 8 nodes having 2 degrees of freedom at each node: translations in the nodal x and y directions. The ANSYS computation domain and the results of base case simulation are in Figures 10 and 11;

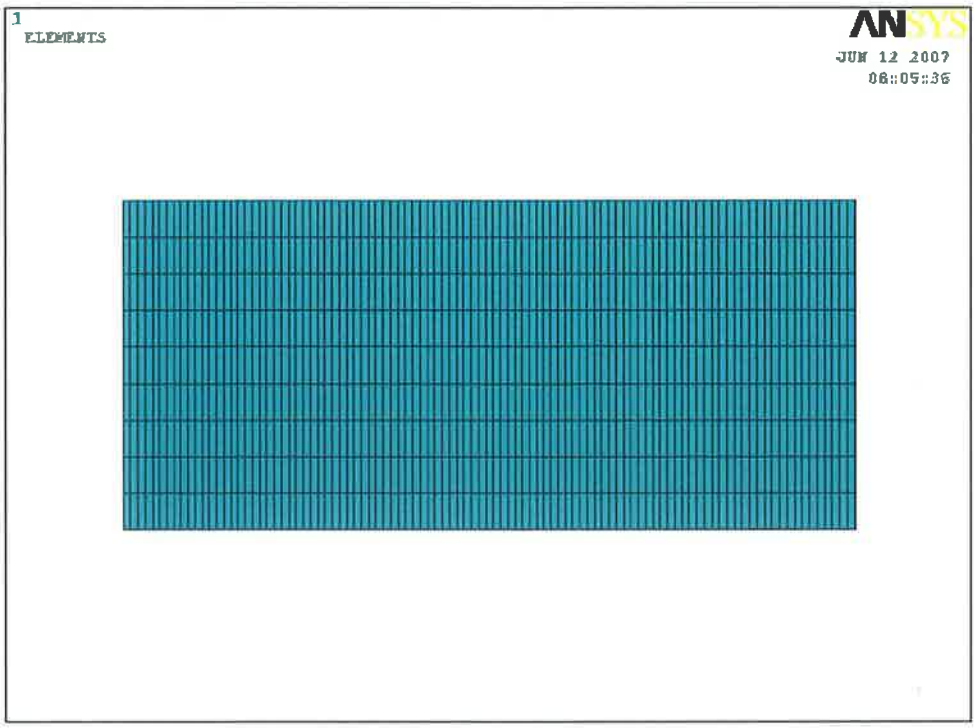

Figure 10, Schematic of computation domain for ANSYS simulation

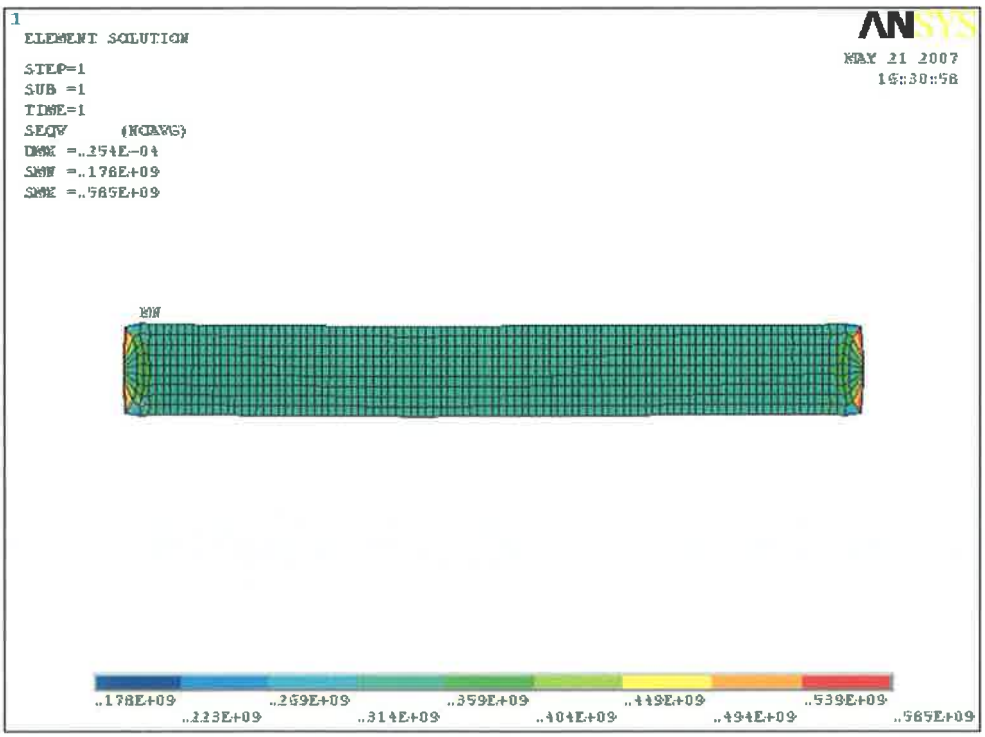

Figure 11, ANSYS simulation results for the base case

3.4.3 Finite Element Modeling

The mechanical properties obtained experimentally from tensile and flexural test, were used in numerically simulating the residual stresses, after inclusion of the elevated temperature operation effect, in the transition-piece outer wall using the commercial finite element package ANSYS 10.0. The AISI 660 (A286) iron-base superalloy was modeled as elastic-plastic material using the Multilinear Isotropic Hardening (MISO) option of ANSYS [125]. MISO uses the Von-Mises yield criteria coupled with an isotropic work hardening assumption. This option is often preferred for large strain analysis. The process of obtaining the properties of A286 alloy experimentally will be explained later in chapter 4.

3.4.4. Effect of Operation at Elevated Temperature

The effect of operation at elevated temperature on the transition-piece material was included in the material modulus of elasticity. It is reported that, the elevated temperature operation reduces the modulus of elasticity of steel alloys [126]. For A286 alloy the below table shows the effect of elevated temperature operation on the modulus of elasticity [61];

Elastic Modulus (Pa)		
Material Condition	Experimental results	Elevated Temperature operation effect
AR Material	2.07 E+11	1.61 E+11
HT Material	1.38 E+11	1.07 E+11

Table 8, ANSYS simulation elastic modulus of elasticity

4

EXPERIMENTAL EQUIPMENT AND PROCEDURES

4.1 INTRODUCTION

In this chapter, the different items of equipment used in this research are described. These equipment includes Scanning Electron Microscope (SEM), Energy Dispersive X-Ray Spectroscopy (EDS), X-ray Diffraction (XRD), microhardness tester, 3-point bending and tensile testing facilities. Information is also given on the preparation of the test specimens. The above will be followed by the description and procedure of each mechanical test conducted.

4.2 EXPERIMENTAL EQUIPMENT

Descriptions of the equipment used in the experimental work are given in the applicable sub-heading.

4.2.1 Three-Point Bending Equipment

The 3-point bending test was carried out using the INSTRON 8801 (Figure 12) [127]. The machine is equipped with a deflection measuring device where the error in the load measuring system was ± 1 % of the maximum applied load. There was no pre-loading in the machine, and each specimen was placed carefully into the test fixture, to preclude possible damage and to ensure alignment of the specimen in the fixture.

The specimen was centered directly below the axis of the applied load, with equal amounts of overhang beyond the outer bearings. The loading nose had a cylindrical surface with radius of 5 mm (0.197 in), to avoid excessive indentation, or failure due to stress concentration directly under the loading nose. The tree-point bending tests were repeated four times at the same temperature (room temperature) and the experimental error based on the repeatability tests was in the order of 4%.

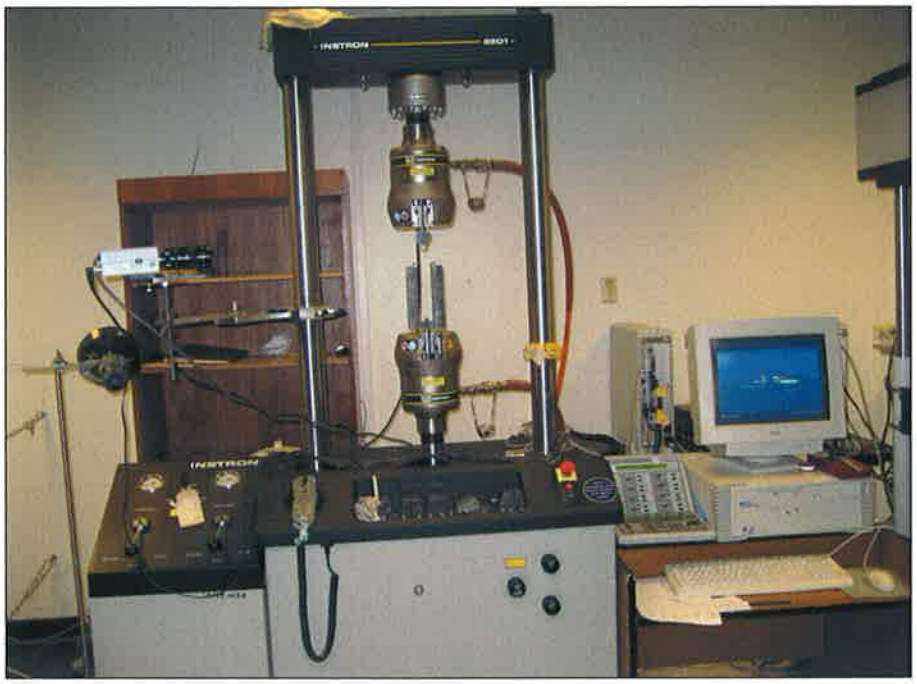

Figure 12, Photograph of the INSTRON 8801 during three-point testing

4.2.2 Tensile Test Equipment

The tensile test was performed using the INSTRON 5569 mechanical tester [128]. The machine is capable of doing a wide variety of mechanical testing (Figure 13). The tester is equipped with instrument control and the data acquisition and analysis are performed through BLUEHILL software with the accuracy of 0.5% of the applied load. The setup is equipped with a temperature chamber that allows testing over a wide range of highly controlled temperatures (-20 to 350 $^{\circ}$C) for conducting tensile tests. The tensile tests were repeated four times at the same temperature (room temperature) and the experimental error based on the repeatability tests was in the order of 3%.

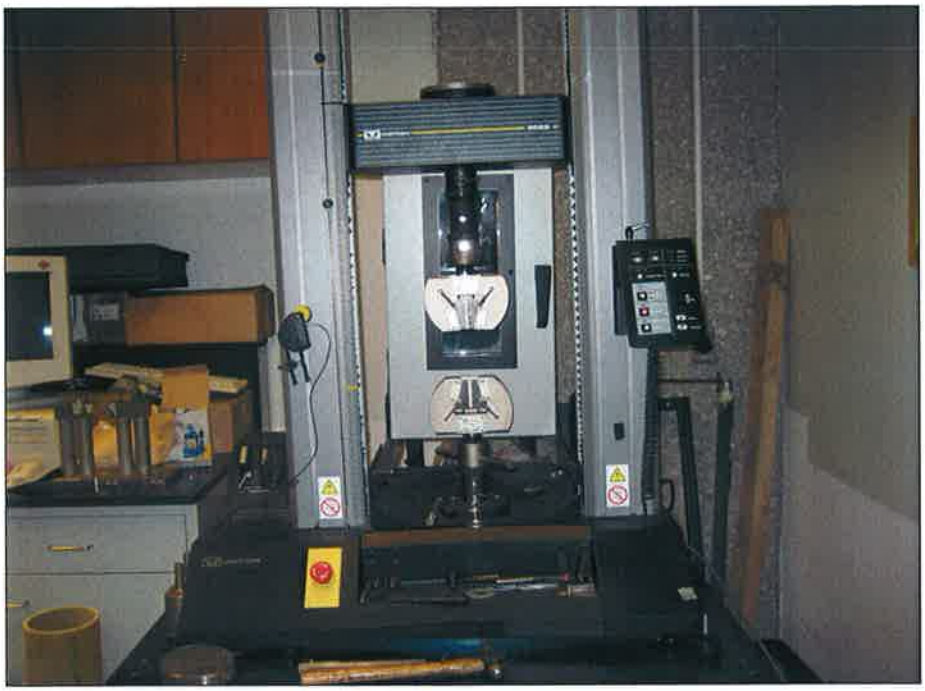

Figure 13, Photograph of the INSTRON 5569 tensile tester

4.2.3. Scanning Electron Microscope (SEM)

Scanning Electron Microscope (SEM), Model 6460 LV Manufactured by SEM - JEOL, Japan and EDS -OXFORD Instruments, UK was used for material analysis [129]. The high-precision system incorporated in this SEM is effectively used with the large flexible chamber that accommodates a maximum 200 mm diameter specimen. Its resolution is 3.0 nm, accelerating voltage is 0.3 – 30 kV and its magnification is ×5 to 300,000 (Figure 14). Polished as received and heat treated samples were placed in the SEM vacuum chamber, and analysed to reveal the material characteristics.

Figure 14, Photograph of the SEM

4.2.4 Energy Dispersive X-Ray Spectroscopy (EDS)

Energy dispersive X-Ray spectroscopy (EDS) is defined as an analytical method used in the determination of elemental chemical composition, and normally performed in conjunction with a scanning electron microscope (SEM) [130]. The technique utilises X-Rays, which are emitted from the sample during the bombardment by the electron beam, to characterise the elemental composition of the analysed material. It was reported that features as small as about 1μm can be analysed [131]. When the test sample is bombarded by the electron beam, electrons are ejected from the atoms along the sample's surface. A resulting electron vacancy is filled by an electron from a higher shell, and an X-Ray is emitted from the sample to balance the energy difference between the two electrons. The EDS X-Ray detector measures the number of emitted X-Rays versus their energy. The energy of the X-Ray is characteristic of the element from which the X-Ray was emitted.

A spectrum of the energy versus relative counts of the detected X-Rays can be obtained and evaluated, for qualitative and quantitative determinations of the elements present in the sampled volume. It is important to note that EDS analysis of light elements such as oxygen is at best semi-quantitative, and the relative accuracy depends on the amount present in the sample. For example, errors in the analysis for concentrations below 5 % can be as high as ± 50% [132].

In the current research the SEM with an EDS X-ray instrument used and the analysis was used to measure the amount of elements contained in the specimen material such as; Oxygen, Aluminium, Silicon, Nickel, Chromium, and Molybdenum.

4.2.5 X-Ray Diffraction (XRD) Equipment

X-Ray Diffraction (XRD) is a non-destructive technique for analysing of a wide range of materials. Its areas of application include qualitative and quantitive phase analysis, crystallography, texture and residual stress investigations. The equipment used in this research is XRD-D8 manufactured by Bruker of Germany as shown in Figure 15 [133]. These quantitative procedures have been demonstrated to produce error distributions characterized by a standard deviation of less than 3% relative when the samples are in the ideal form of a metallographically polished bulk solid

Figure 15, Photograph of Bruker XRD Equipment

4.2.6 Tube Furnace

For producing heat treated condition of the AISI 660 (A286 Iron-Base Superalloy) specimens a tube furnace was used. It is manufactured by Lindberg with a temperature range of 200 – 1200 ^{o}C as shown in Figure 16, [134]. The furnace is suitable for quenching, tempering, annealing, normalizing and general heating processes.

Figure 16, Photograph of Tube Furnace

4.2.7 Micro Hardness Tester

For measuring and comparing the hardness of the two conditions of the samples a micro hardness tester was used. It is manufactured by Buehler, USA with load range of: 1, 5, 10, 50, 100, 300, 500 and 2000 g. The tester is suitable for thin and thick sections (Figure 17), [135]. The error related with the hardness tests was in the order of 1%.

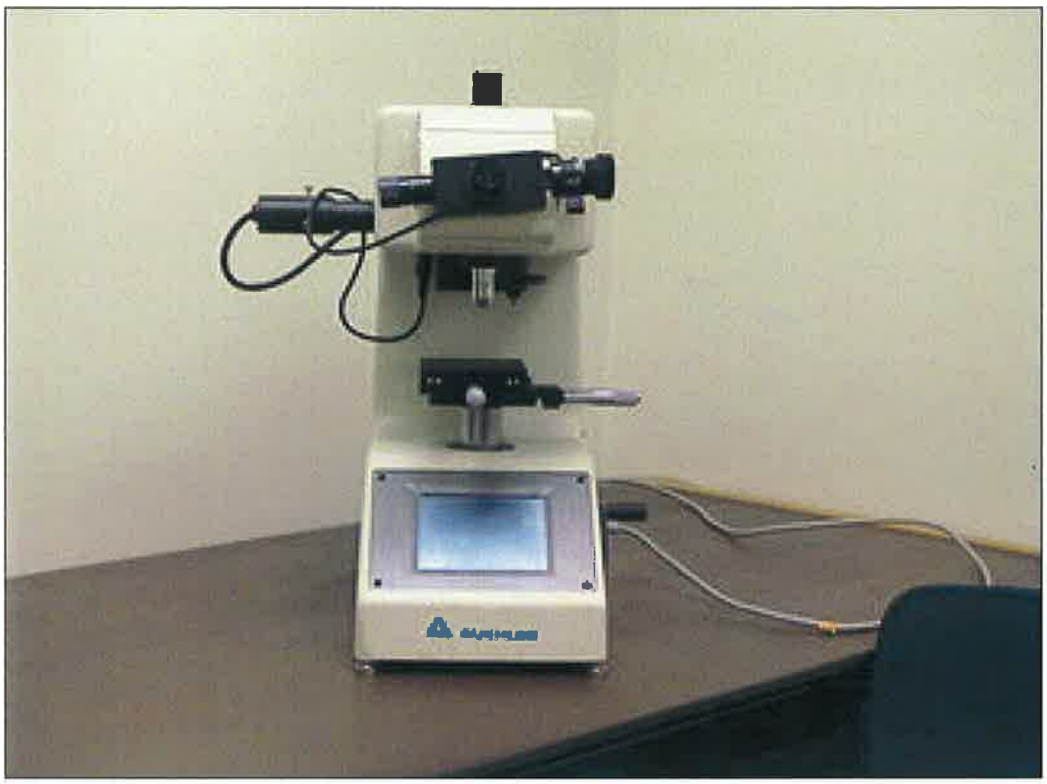

Figure 17, Photograph of Micro hardness Tester

4.2.8 Polishing Wheel

For polishing the test specimens a polishing wheel manufactured by Polimet Polisher, USA was used [136]. The machine is suitable for polishing regular and irregular specimens by using different size grit powder from coarse to fine polishing. A maximum of 9 samples can be mounted at the same time. The plate size of the machine is 12" and its speed is 50 - 490 rpm (Figure 18).

Figure 18, Photograph of Polishing Wheel

4.2.9 Mounting Press

For the mounting of samples in Lucite for optical and electron scanning microscopes, a mounting press manufactured by Buehler, USA was used (Figure 19), [137].

Figure 19, Photograph of Mounting Press

4.2.10 Optical Microscope

Optical Axioplan 2 Imaging Microscope manufactured by Zeiss, Germany (Figure 20) was used to study the microstructures by reflection and transmission modes [138]. The microscopy is also suitable to carry out multiphase analysis and grain size measurement.

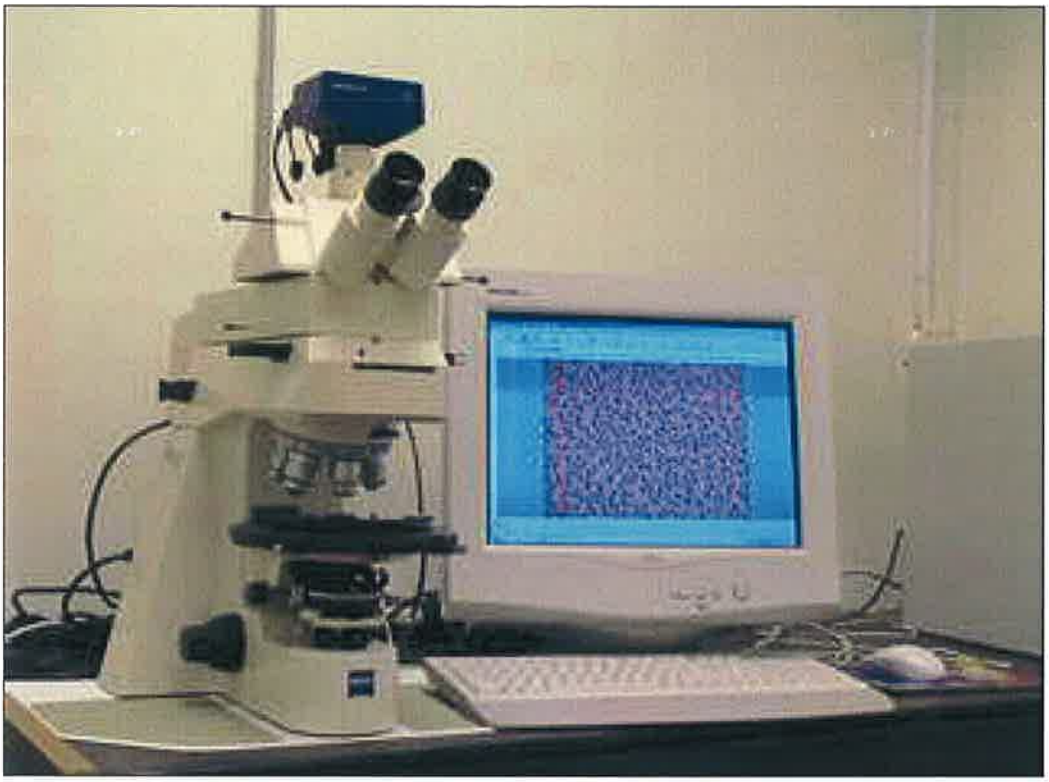

Figure 20, Photograph of Optical Microscopy

4.3. EXPERIMENTAL PROCEDURES

The material used in this investigation is AISI type 660 stainless steel (Iron-base A286 superalloy) supplied by Bohler Edestahl of Germany [2]. The chemical composition of the material was confirmed by the EDS and XRD as in Table 9.

Element	Al	B	C	Cr	Mo	Fe	Mg	Ni	P	S	Si	Ti	V
wt%	0.17	0.0047	0.034	15.2	1.16	Bal	1.21	24.96	0.016	<0.003	0.3	1.96	0.25

Table 9, Chemical composition of A286 iron-base superalloy

4.3.1 Specimens Preparation

The test specimens of A286 Iron-Base Superalloy were obtained from hot rolled bar 28.525 mm in diameter and a length of 3 meters. The bar was machined producing 20 test specimens of two configurations;

1. The rectangular configuration as in Figure 21a

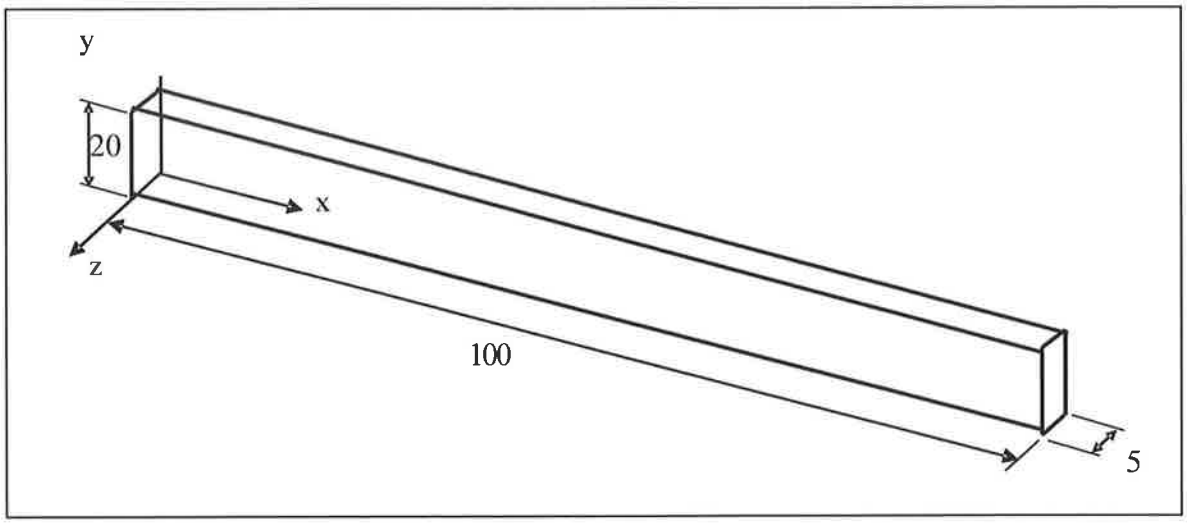

Figure 21a, Rectangualr specimens configuraion dimensions (in mm) [141]

2. The dog bone configuration with dimensions of as shown in Figure 21b.

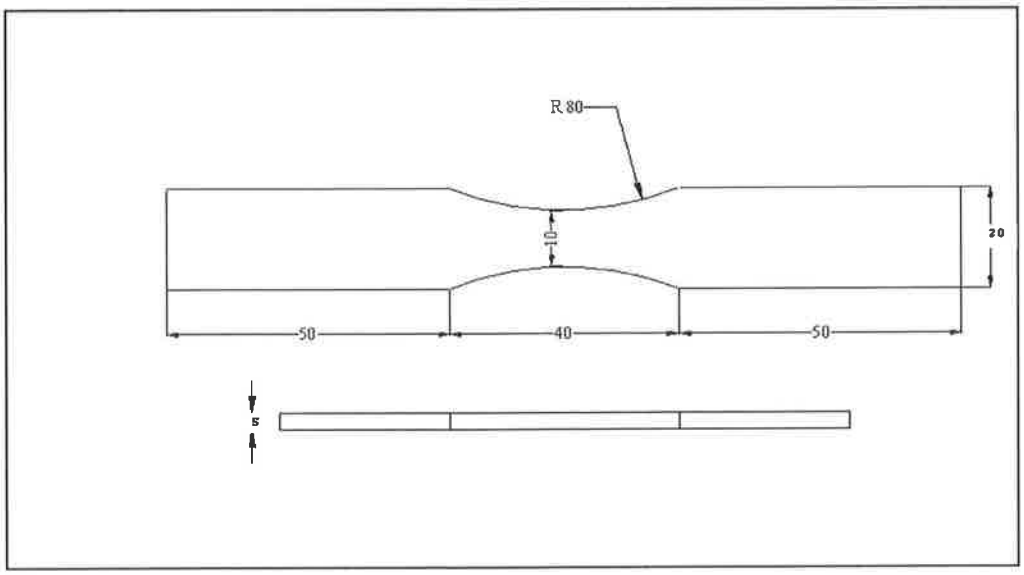

Figure 21b, Dog bone test specimens configuraion dimensions (in mm) [142]

The following definitions are used in this thesis;

As Received Condition: - Solution Annealed 980 °C for 1.5 hours and then water quenched. Precipitation Hardened: 710 °C for 16 hours and air cooled. Ten test specimens were produced in this condition resembling the original material used in the P&W gas turbine engine FT4-9B transition-piece.

Heat Treated Condition: - the as received specimens were solution treated for one hour at 930 °C; air cooled and aged for 16 hours at 730 °C to retain the original material properties and to relieve the residual stresses developed from the machining process during the preparation of the test specimens. Ten test samples were produced in this condition.

4.3.2 Metallographic Preparation

Metallography is the technique of taking images for topographical or microstructural features on prepared surfaces of materials [139]. The properties and performance of the material may be controlled by studying the microstructures using metallography. Metallographic specimen preparation is an important tool for the characterisation of the material. The metallographic process can be divided into five different stages; sectioning, mounting, grinding, polishing and etching.

(1) Sectioning

Sectioning is a necessary step before mounting to reduce the size of the test sample to explore its hidden cross-section. The test specimens were sectioned using an ISOMET low speed diamond cutting saw manufactured by BEUHLER ISOMET, a water-based lubricant cutting fluid which is used as the cooling medium. The low speed cutting saw was used to minimise stresses and distortion of the sectioned surface, which can often be introduced by cutting processes.

(2) Mounting

There are two basic techniques of mounting; cold and hot. Cold mounting requires very simple equipment consisting of a cylindrical ring which serves as a mould and a flat piece of glass for the base of the mould. The sample is placed on the glass within the cylinder and the melted resin poured in and allowed to set, which takes about 40 minutes to complete. Hot mounting uses both heat and pressure to thermoset resin, and in some cases, this method is not preferred particularly if the sample is sensitive to temperature and has a loose layer on its surface which is not for the research in hand. In hot-mounting the sample is surrounded by an organic polymeric powder (bakelite powder) which melts under the influence of heat (up to 120 ^{o}C). Pressure is also applied by a piston, ensuring a high quality mould, free of porosity and with intimate

contact between the sample and the polymer. In the current research, the hot mounting machine SIMPLIMET 2000 made by BUEHLER was used.

(3) Grinding

The prepared mount (sample contained in a thermoset mould) was then subjected to a series of grinding steps, with the aim of producing a surface which would reveal its microstructure characteristics, produce a flat surface and regular face. In the current work, only the P240, P320, P400 and P600 grit papers were used to fine grind the different samples, as this was found to be adequate for revealing the characteristics of the concerned material. Each paper was used for duration of 4 minutes. Grinding was performed at a contact pressure of approximately 100 to 150 kPa and using water as a lubricant.

(4) Polishing

The objective of the polishing stage was to remove the abrasion-damage layer that may appear as scratches, or as slip/twin/shear damage beneath the surface caused by the grinding stage. Optical microscopy requires that a specimen must be both flat and highly reflective [140]. There were two steps involved in the polishing procedure; diamond polishing and fine oxide particle polishing. Diamond abrasives are very effective during the polishing stage and considered as an adequate tool to prepare a sample for general microscopic examination. The most common diamond particle sizes are 6, 3 and 1 microns. Normally each abrasive size can be used for 5 minutes in turn, starting from 6 microns finishing with 1 micron. In the current research, Aluminium oxide polish (Al_2O_3) compound with 0.05 micron particle size was used for duration of 10 minutes to prepare the specimens. Polishing was performed at a contact pressure of 100 to 150 KPa using water as a lubricant.

(5) Etching

The previous procedure was finally followed by chemical etching in a solution of distilled water 25 ml, Nitric acid (1.4) 20 ml, hydrochloric acid (1.19) 20 ml,

hydrogen peroxide (30%) 10 ml. A trial and error technique was used to determine the period needed between the etching and examining the specimen, using the SEM, to prevent under etching or over etching.

4.4 MECHANICAL TESTING PROCEDURES

The mechanical tests carried out and described in this chapter include; tensile and bending tests. These tests were performed according to international standards; ASTM D 790 [141] and ASTM E8M-00B [142] for bending and tensile tests respectively. The following sections will explain in details the preparation of each test.

4.4.1 3-Point Bending Test

The 3-point bending test has been carried out in this research specifically to determine the modulus of elasticity and how it varied for the two conditions; AR and HT. The 3-point bending test was carried out using the 3-point bending test configuration according to the international standards [141] (Figure 22 and 23).

Test specimens of rectangular cross-section were placed on two supports and loaded by means of a loading nose midway between the supports. The tests were carried out at room temperature 25 ± 2°C and 50 +/- 5% relative humidity. The strain rate used was 2.5 mm/min, and to ensure accuracy and repeatability of the results a total of four samples for each material condition were tested. The measurement error based on the repeatability is within 5%. During the tests, the load and displacement characteristics were recorded. The tests were terminated when the sample failed or it reached the 5% of its flexural strain. The experimental error based on the repeatability tests was in the order of 4%.

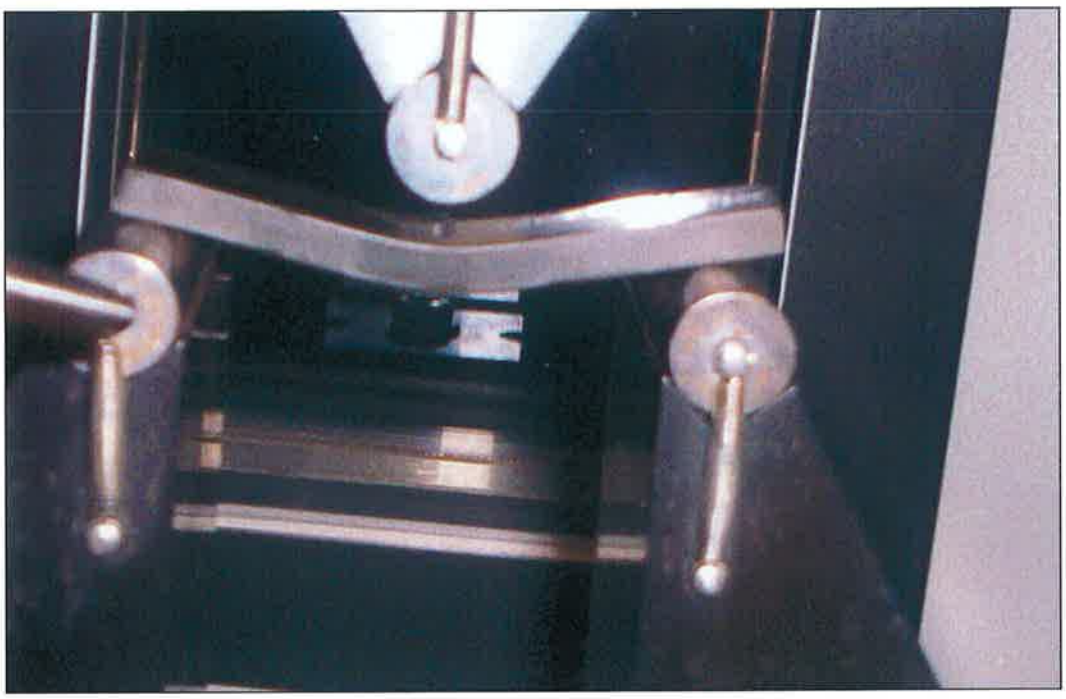

Figure 22, Photograph of flexural test in progress.

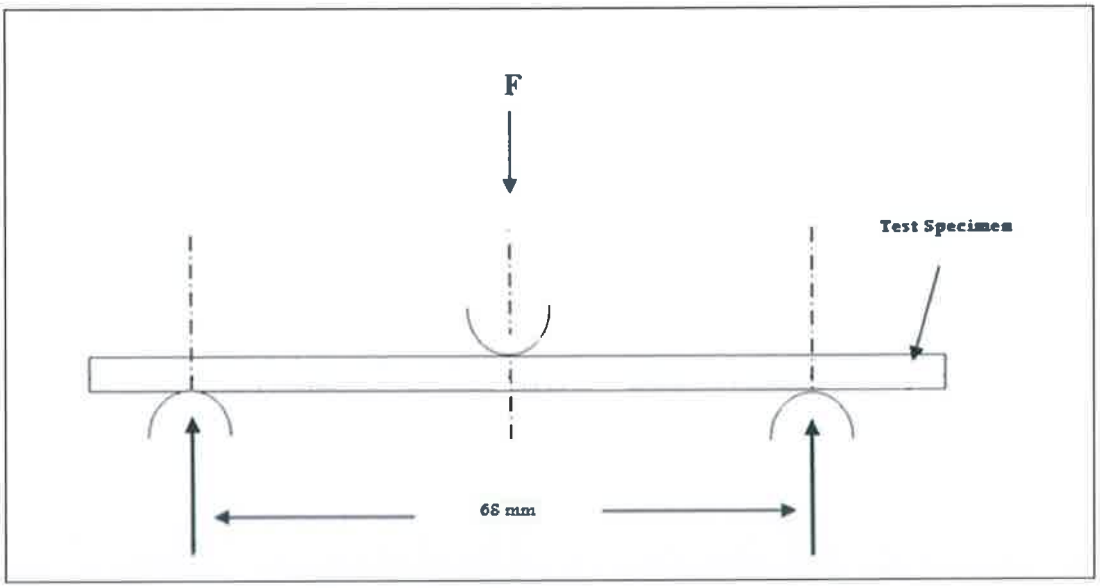

Figure 23, Flexure test configuration.

4.4.2 Tensile Testing

The tensile test was carried out using the international standards [142]. Tensile tests are carried out for any metallic materials, in any form at room temperature, for determination of yield strength, yield point elongation, tensile strength, elongation and reduction of area, thus providing information on the strength and ductility of materials under uniaxial tensile stresses. The aim of conducting the tensile test specifically in this research, is to evaluate the modulus of elasticity change in the iron-base A286 superalloy associated with the different heat treatment conditions. The test specimens employed for determining the stress-strain behavior of the materials were dog-bone shape to reduce the cross-section at area and force the failure to occur in the specimen mid-section (Figures 24). The test specimen was placed in between the upper and lower self aligning mechanical grips, with the grips placed 25 mm from each end. A minimum of four specimens were tested for each condition at room temperature of 25 ± 2°C and 50 ± 5% relative humidity. The test pieces were set-up in the testing machine with zero loads. The tensile tests were conducted at a cross head speed of 3 mm/min. The elongation was measured at the parallel distance of the dog-boned test piece. The original gauge length is 25 ±5% mm. The tests were repeated four times to ensure repeatability. The repeatability of tests was limited by four times due to the limited number of test specimens available. It was found that the relative error based on the repeatability is within 3%.

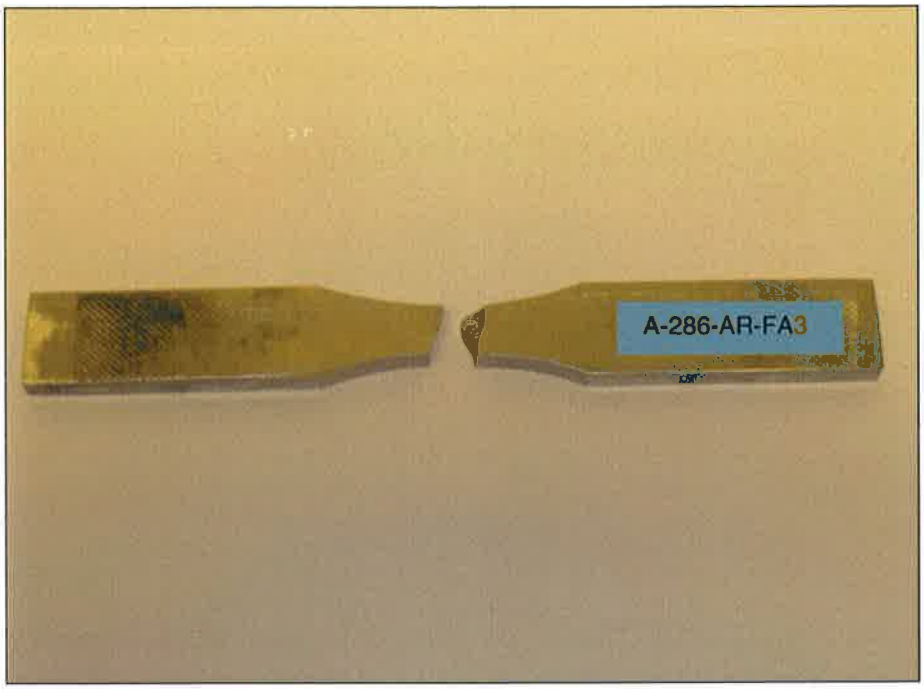

Figure 24, tensile test specimen after failure.

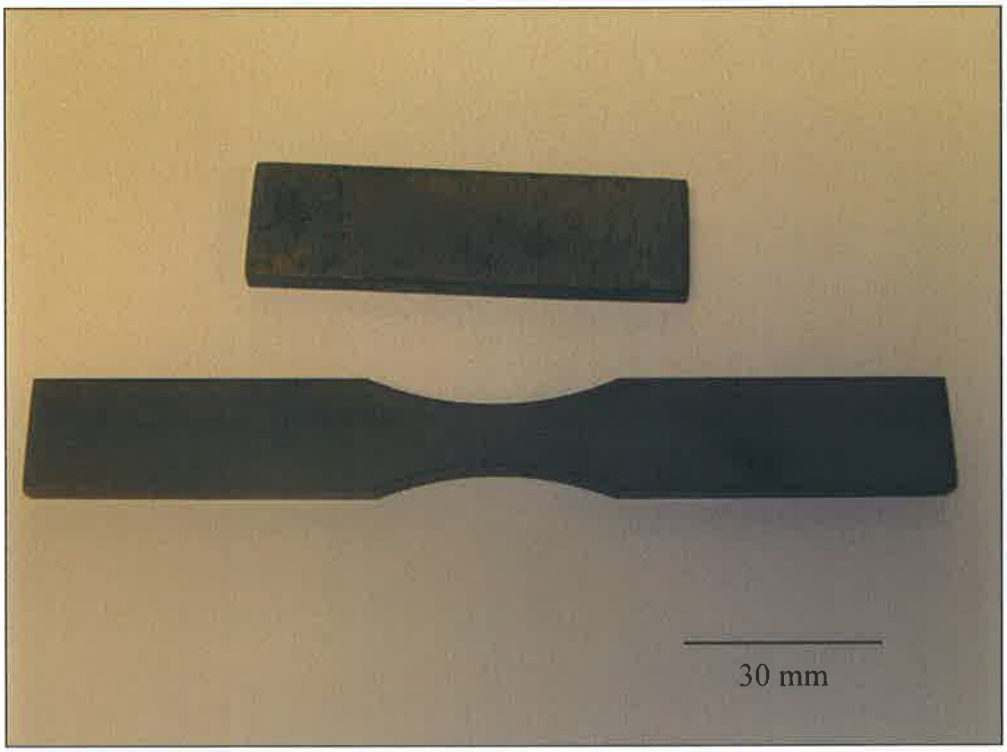

Figure 25, Photograph Heat Treated Test specimens

4.5 DETERMINATION OF MODULUS OF ELASTICITY

4.5.1 Flexural Strength (Bending) Testing

It was assumed that the beams were subjected to pure bending with no shear. The beams were simply supported, and loaded with a concentrated load, applied in the middle of the span. The equation used for calculating Young's Modulus of Elasticity (E) of the test specimens for the two conditions is [84];

$$E = \frac{FL^3}{48dI}$$

Where:-

F: - Applied force (N)

L: - Span between the two the roller bearings (m)

d: - Sample deflection (m)

I: - Second moment of area (m^4)

Table 10, below gives the calculation results;

Sample	L (m)	I (m^4)	d (m)	F(N)	E (Pa)
As Received (AR) Analytical	0.068	2.0833E-10	0.0067	4455	2.08E11
Heat Treated (HT) Analytical	0.068	2.0833E-10	0.00255	1126.556	1.38E+11

Table 10, Elastic modulus results of 3-point bending test.

$$E_{HT} = E_{AR} \times 66.3\%$$

where

E_{HT} Modulus of elasticity of the heat treated material

E_{AR} Modulus of elasticity of the as received material

4.5.2 Tensile Testing

The elastic modulus was determined for the as received condition, and for the heat treated condition, from the tensile test by measuring the load and position data throughout the test, then determining E within the elasticity range. The following relationship was used;

$$E = \frac{\sigma}{\varepsilon}$$

Where:-

E: - Modulus of Elasticity (Pa)

σ = Stress (Pa)

ε = Strain

Table 11, below gives the calculation results;

Sample	σ (MPa)	ε	E (Pa)
As Received (AR)	340.9574	0.001829419	2.07E+11
Heat Treated (HT)	312.0188	0.002288951	1.37E+11

Table 11, Elastic modulus results of tensile test.

$$E_{HT} = E_{AR} \times 66.2\%$$

where

E_{HT} Modulus of elasticity of the heat treated material

E_{AR} Modulus of elasticity of the as received material

Difference in E calculated values obtained for the as received test specimens between the 3 points bending test and the tensile test is 0.005 %, while difference

in E calculated values obtained for the heat treated test specimens is 0.007 %. The results obtained from the 3-point bending are in line with the published values for this material in as received condition [2], while the E values calculated for the as received test specimen from the tensile test is not in line with the other two values (i.e. published values and values from the 3 points bending test).

The difference can be attributed to several factors including homogeneity of the material, repeatability of specimen preparation, test conditions and measurements of test parameters. Instrumental factors such as stiffness, damping capacity, natural frequency can also affect the test results. Based on the above, the E values obtained from the 3-point bending tests were used in the thermal stress mathematical simulation.

4.5.3 Micro-Hardness Testing

Microhardness test was carried out to determine the ductility difference between the two material conditions. The test was repeated four times at different locations in each specimen using 500 g load, and the results were as follows:

- The average reading of four tests at different locations for the AR specimen was; 383 HV
- The average reading of four tests at different locations for the HT specimen was; 272.25 HV.

5

RESULTS AND DISCUSSION

5.1 INTRODUCTION

The present research aims to investigate numerically and experimentally, the effects of flow and heat transfer, on the thermal stress levels in the transition-piece of an aero-derivative gas turbine engine made of A286 iron-base superalloy. The typical operating conditions of the transition-piece are taken into consideration in the simulation, in which case, the typical variation of the affecting parameters, namely mass flow rate and entry temperature during operation of the aero-derivative gas turbine engine were considered. The experimental part of this study is carried out, to determine the elastic modulus of the AR and HT transition-piece material, taking into account the effect of elevated temperature operation on the elastic modulus to resemble the actual operating conditions. Tensile and 3-point bending tests were carried out in this regard and the elastic moduli obtained from the experimental work were employed in the numerical simulation to predict the thermally induced stresses in the transition-piece.

In this section, the effect of operating with nominal conditions, and the resulting developed thermal stress level in the AR material of the transition-piece casing was discussed. That is followed by discussion of the effect of varying the operating entry mass flow rate and the operating entry temperature independently, on the developed thermal stress level on the induced thermal stress level in the transition-piece casing. Finally, the influence of the material properties and the effect of the heat treatment of the substrate material on the thermally induced stress were discussed.

5.2 THERMAL STRESSES DEVELOPED IN THE TRANSITION-PIECE CASING DURING STEADY STATE OPERATION

(BASE CASE OPERATION)

The flow field inside a typical transition-piece of an aero-derivative gas turbine engine was simulated. Velocity and temperature fields' distributions inside the transition-piece were predicted numerically using the FLUENT CFD code. The control volume approach was introduced when discretizing flow governing equations. Thermal stress developed in the outer casing of the transition-piece was computed, using ANSYS FEM code and modulus of elasticity of as received A286 alloy.

Figure 26, shows the physical domain while Figure 27, shows velocity magnitude contours values in m/s inside the transition-piece for the base case with the nominal values of operation parameters (Table 5). Since the flow field is axisymmetric, half the flow solution domain is shown. It was noted that the velocity magnitude reduced along the axial direction from a maximum value of 371 m/s at the inlet towards the transition-piece exit, where the velocity reached value between 334m/s at the middle of the exit plane in the y direction to zero value at the wall. This is more pronounced in the flow downstream close to the exit. This is due to the flow expansion enlargement of the transition-piece towards the exit. Moreover, the flow deceleration in the radial direction is more pronounced in the region close to the outer casing of the transition-piece. This due to the transition-piece geometry, which is annular, consequently, fluid close to the outer casing attains lower velocity than that corresponding to the region close to the inner casing. Moreover, radial deceleration of the fluid did not result in flow separation or circulation zone in the region close to the outer casing. This is mainly because the axial momentum change of the fluid is considerably higher than that occurring in the radial direction. Consequently, secondary flow due to separation of the fluid in the downstream did not occur.

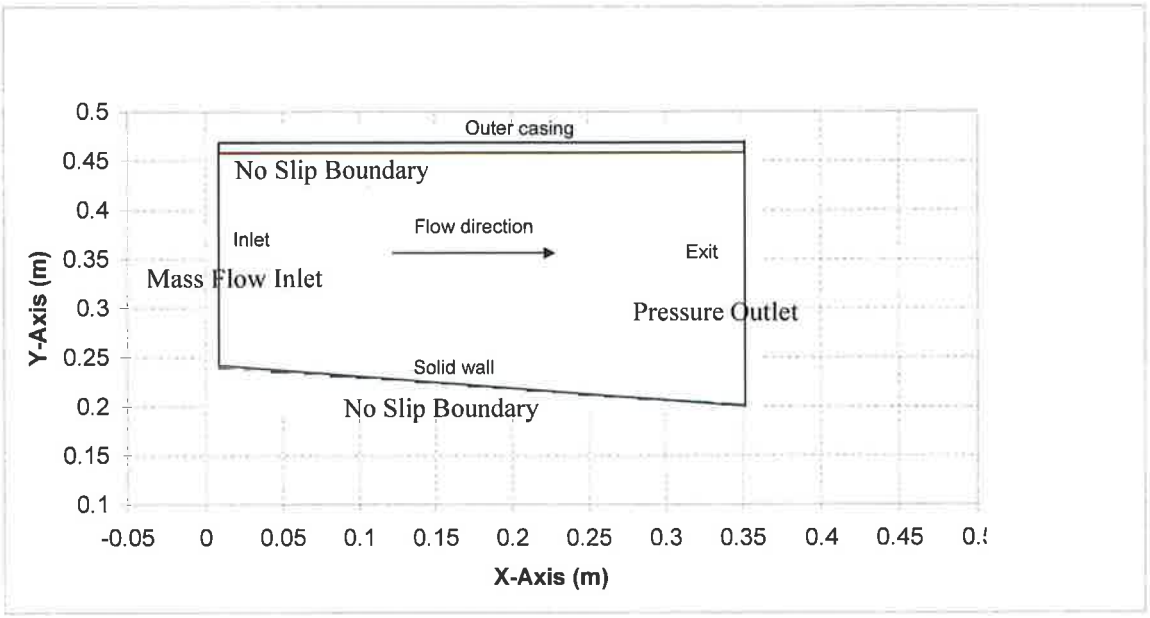

Figure 26, Physical domain of the transition-piece.

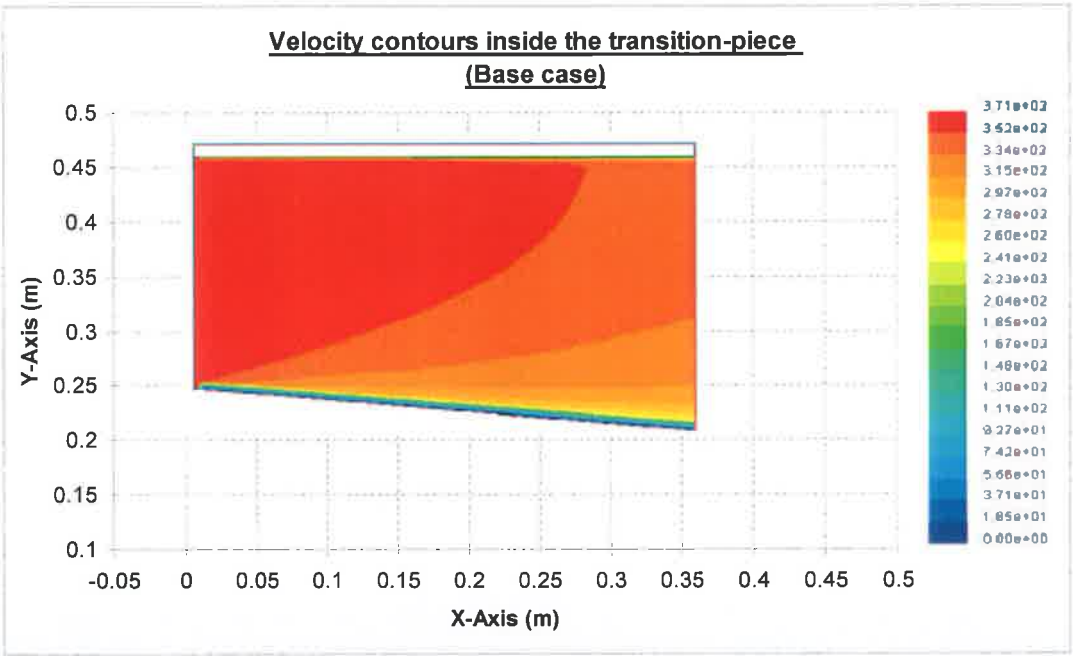

Figure 27, Velocity magnitude inside the transition-piece for the base case. Velocity unit is in m/s.

Figure 28 shows pressure contours inside the transition-piece. The gradual increase in the pressure from a minimum value of 200 MPa at the lower corner of the inlet plane to a maximum value of value 267 MPa across the exit plane is evident. Moreover, rapid

expansion of the fluid in the entry region, due to conical expansion of the transition-piece, resulted in a pressure drop in that region. This is particularly true, in the region close to the lower casing of the transition-piece. In this case, sudden expansion in the entry region resulted in acceleration of the fluid in the radial as well as in the axial directions. The radial acceleration resulted in the development of low-pressure region in the entry region of the lower casing. However, as the flow progresses downstream of the transition-piece, the axial diffusion suppresses the radial diffusion. That in turn increases pressure gradually in the exit of the transition-piece. The flow in this region loses its kinetic energy; as a result, constant pressure lines are straightened in the radial direction downstream of the transition-piece.

Figures 29a and 29b show temperature variation in the outer casing of the transition-piece. Temperature at the inner surface of the casing is high and it reduces with increasing radial location towards the outer surface. It should be noted that; at the outer surface the transition-piece natural convection boundary is considered. Moreover, temperature variation in the axial direction is significant in the entry and exit region of the outer casing of the transition-piece. The attainment of high temperature in the entry region is associated with the boundary condition at the inlet, in which case, convective cooling of the outer surface of the transition-piece is lowered by the low heat transfer coefficient. The sharp drop of the temperature in the casing exit region of the transition-piece resulted from expansion of heated gas in this region. Consequently, the radial acceleration of the heated gas towards the inner casing lowers the heat transfer rates in this region. Moreover, as the flow progresses inside the transition-piece, temperature in the casing increases slightly in the inner surface along the axial direction from a value of 891.2 K at the inlet to 892 K in the middle of the transition-piece to 889.8 K at the exit of the inner surface due to diffusion deceleration of the flow. However, the downstream temperature in the casing reduces further. The attainment of low casing temperature in this region can be associated with the conduction heat transfer as well as low heat transfer rates from fluid to casing in this region i.e. low fluid velocity at the exit lowers the rate of convective heating of the casing in this region. This situation can also be seen in Figure 30, in which the heat transfer coefficient along the inner surface of the outer casing is

shown.

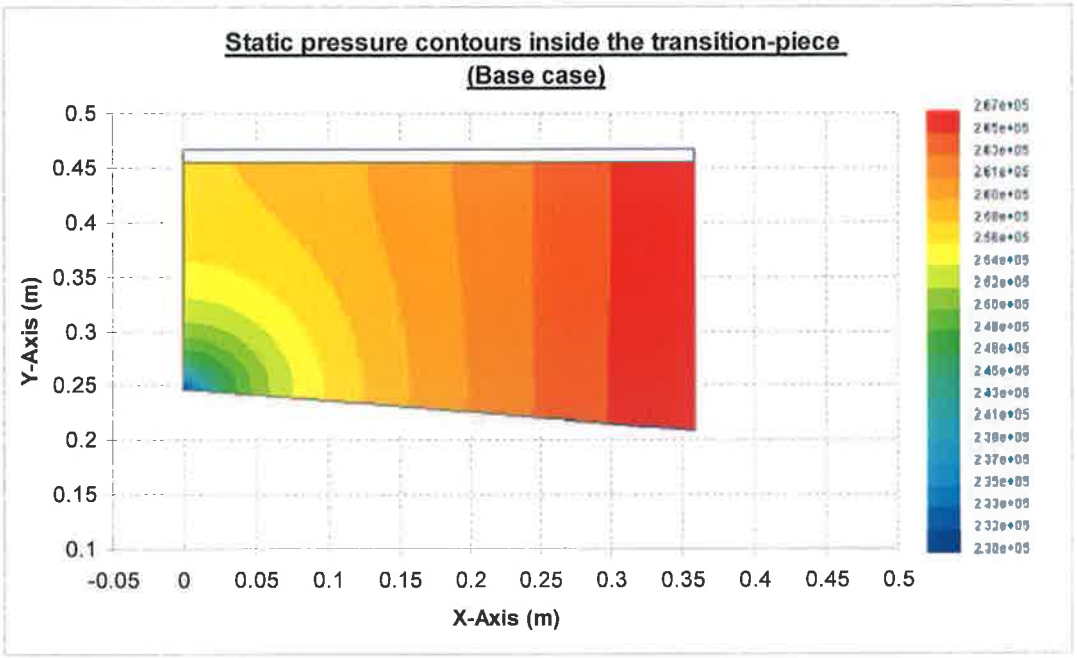

Figure 28, Static pressure contours inside the transition-piece for the base case. Pressure unit is in Pa.

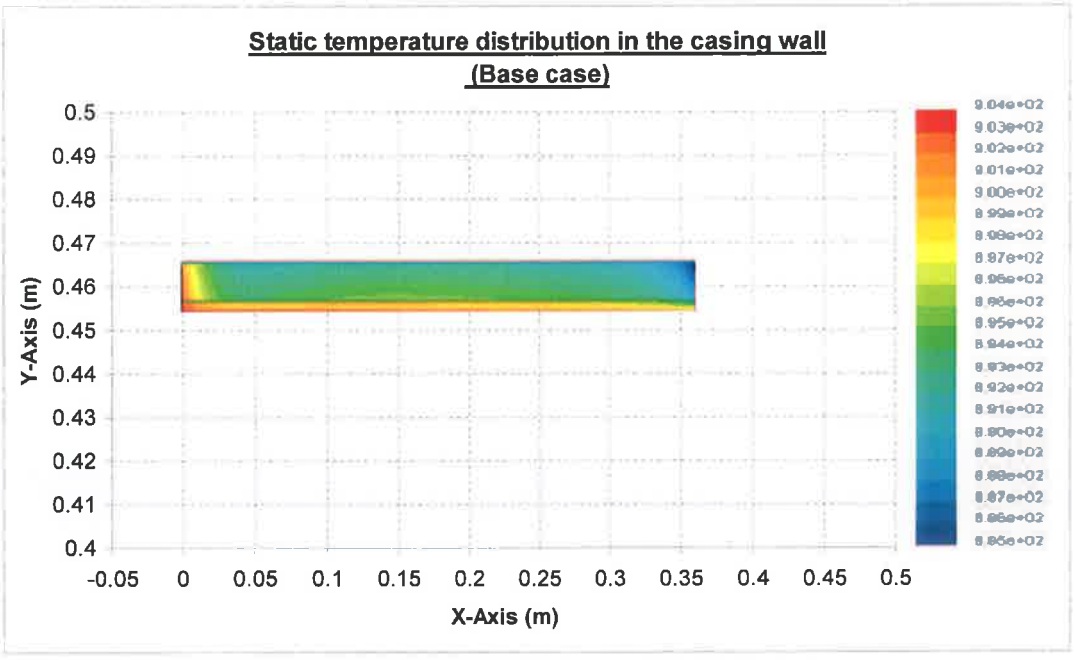

Figure 29a, Static temperature in the transition-piece casing for the base case. Temperature unit is in K.

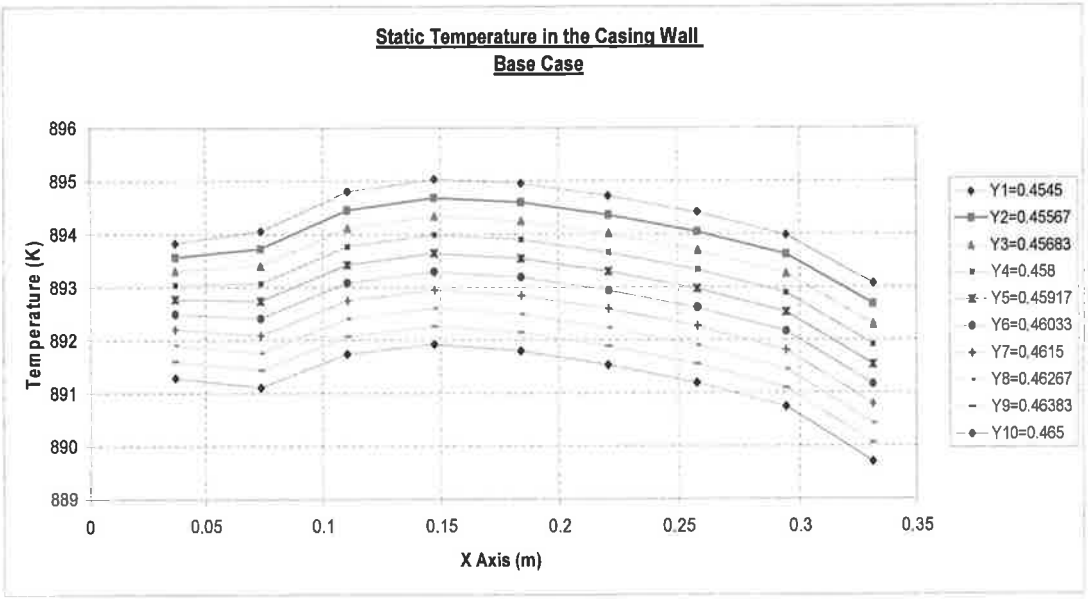

Figure 29b, Static temperature in the transition-piece casing for the base case.

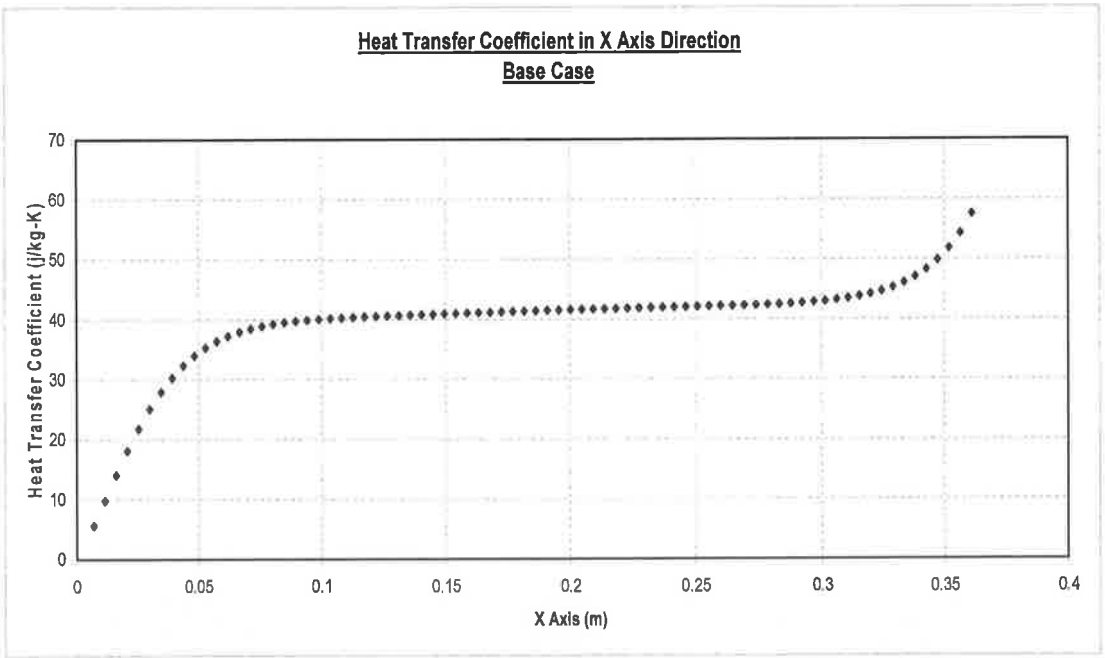

Figure 30, Heat transfer coefficient along the inner surface of the outer casing

Figure 31 shows axial stress components at three locations in the metallic casing of the transition-piece, the radial locations of inner, central, and outer represent the transition-piece inner surface, mid-plane, and outer surface, respectively. The axial stress component is compressive and attains a steady value along the axial distance, except at the inlet and the exit sections of the casing. The compressive stress component is due to the fixed end of the casing, i.e. thermal expansion in the axial direction results in almost uniform compressive thermal stress in the casing along the axial direction. The magnitude of the stress component remains about 350 MPa for all locations in the casing provided that axial stress component in the middle plane of radial location, and at the inlet and the exit of the casing attains higher values corresponding to the same locations in the other planes. Moreover, radial stress component remains low for all radial planes along the axial distance (Figure 32). This is due to free expansion of the casing in the radial direction. It should be noted that the temperature gradient in the radial direction is low; however, radial stress gradient attains slightly higher values at the inlet and exit regions of the casing, due to radially and axially fixed ends of the casing.

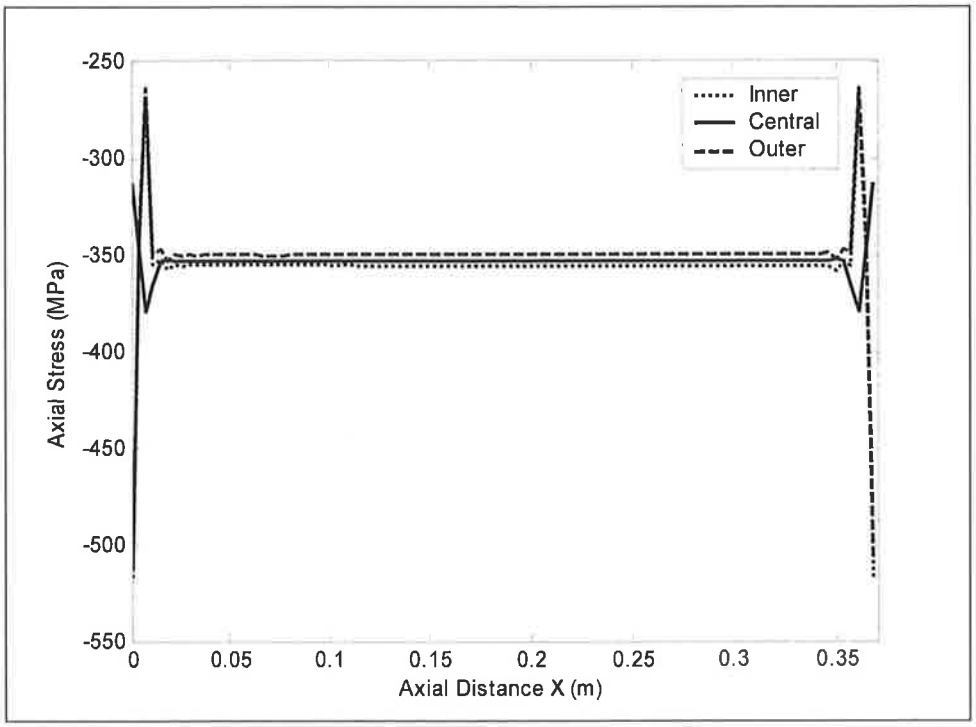

Figure 31, Axial thermal stress along the x-axis in the casing for the base case.

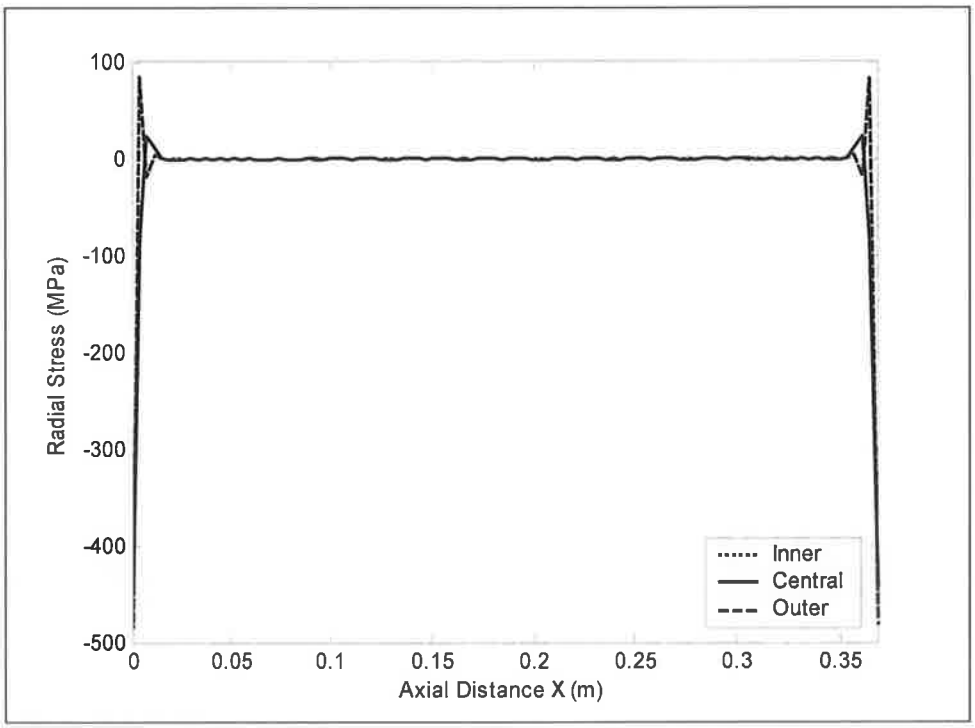

Figure 32, Radial thermal stress along the x-axis in the casing for the base case.

Figure 33 shows von-Mises stress along the axial direction for three radial locations for the as received materials. von-Mises stress shows similar behavior to that occurring for axial stress component. The magnitude of von-Mises stress is less than the yielding limit of the substrate material; consequently, the material response to heating load is elastic.

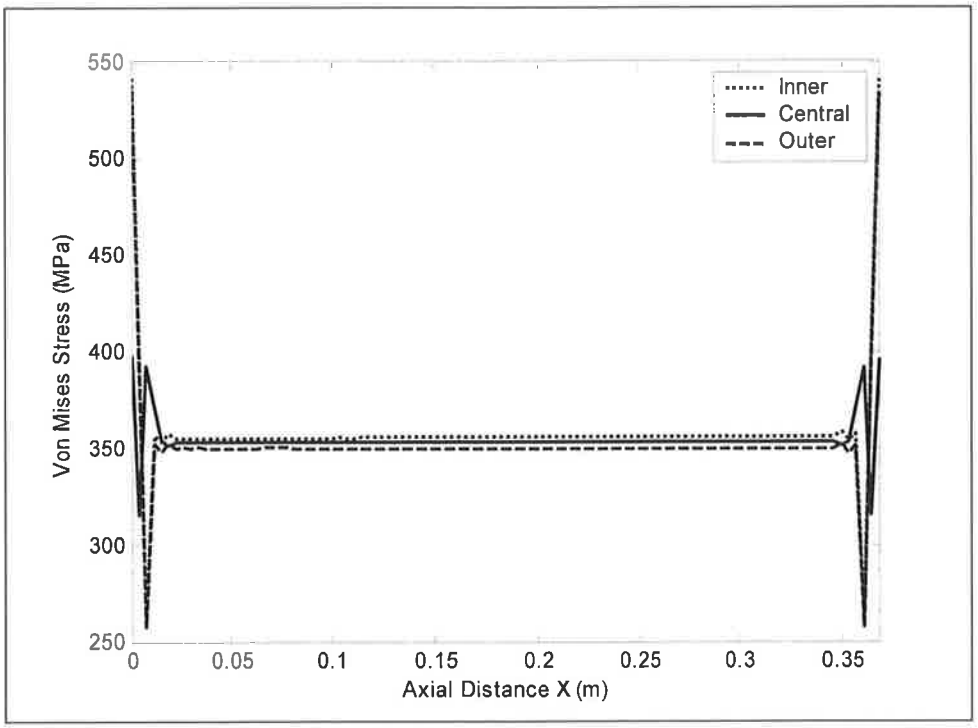

Figure 33, von-Mises thermal stress at the inner casing wall for the base case.

5.3 EFFECT OF MASS FLOW VARIATION ON THE THERMAL STRESSES DEVELOPED IN THE TRANSITION-PIECE CASING

To account for the variation in operating conditions of the concerned aero-derivative gas turbine engine, due to the variation in output demand, and to evaluate the effect of that variation, on the thermally induced stress in the transition-piece casing, the entry mass flow rate was varied in the FLUENT simulation by ±10% from the nominal value in Table 5.

Figures 34 and 35 show the velocity contours in the solution domain for +10% and -10% in the mass flow rate respectively and there is no significant change in the flow structure inside the transition-piece between the two cases. Moreover, there is no significant change in the flow structure between the two cases of ±10% flow variation, compared to the flow structure for the base case (i.e. Figure 27). The only notable difference, is the maximum velocity magnitude change which is approximately 10% higher for the +10% mass flow rate at 408 m/s compared to the base case and 10% lower at 334 m/s for the -10% mass flow rate case. The change in velocity magnitude noted, is by the same magnitude as the mass flow rate compared to the base case (i.e. nominal value). This noted observation between the mass flow change and the corresponding velocity change can be explained by the mass conservation principle (i.e. as the area and the fluid properties are constants, any change in mass flow will show as a variation in velocity with the same magnitude).

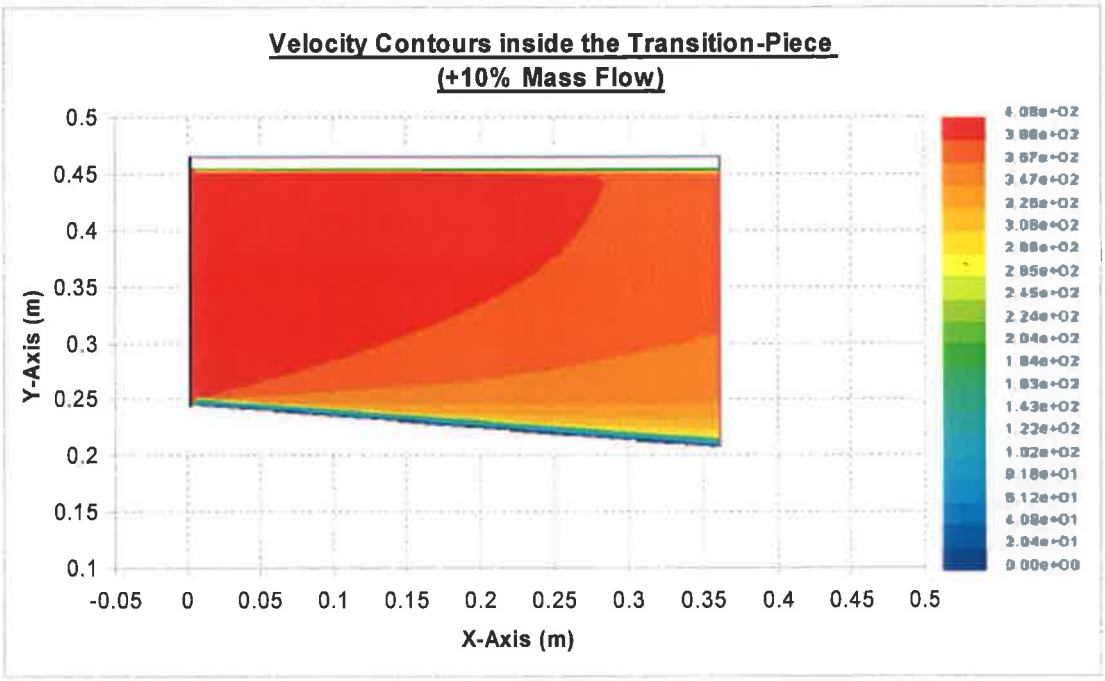

Figure 34, Velocity contours for +10% of nominal mass flow rate. Velocity unit is in m/s.

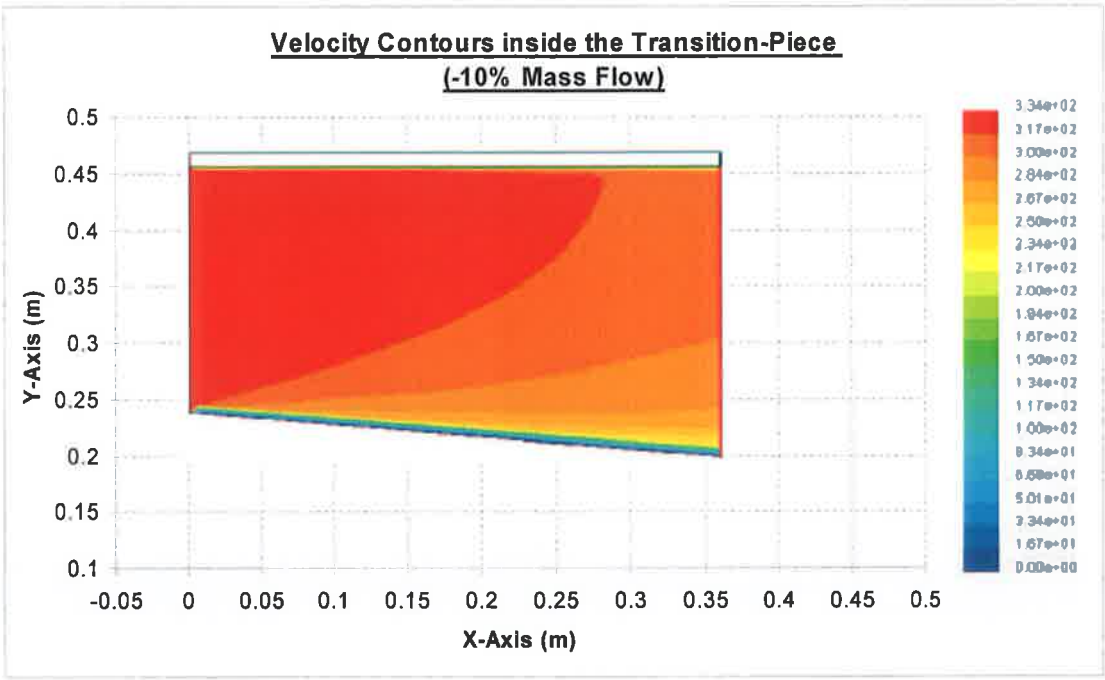

Figure 35, Velocity contours for -10% of nominal mass flow rate. Velocity unit is in m/s.

Figures 36 and 37 show pressure contours in the solution domain for ±10% of the nominal mass flow rate. Comparing the results of the two cases, it can be noted that there is no significant difference either in the magnitude or the pressure distribution inside the transition-piece. Again, comparing Figures 36 and 37 with Figure 28 for the base case, it can be noted there is no difference in magnitude or the pressure distribution. Moreover, the increasing distance from the entrance region of the transition-piece in the axial direction, gives rise to pressure increase towards the exit region of the transition-piece, identical to the base case with no indications of secondary flow development. As a result, it can be stated that the mass flow rate variation does not change the static pressure distribution inside the transition-piece, provided that all other parameters remain the same, and that the difference in pressure due to ±10% mass flow rate change is not significant enough to result in pressure distribution modification inside the transition-piece.

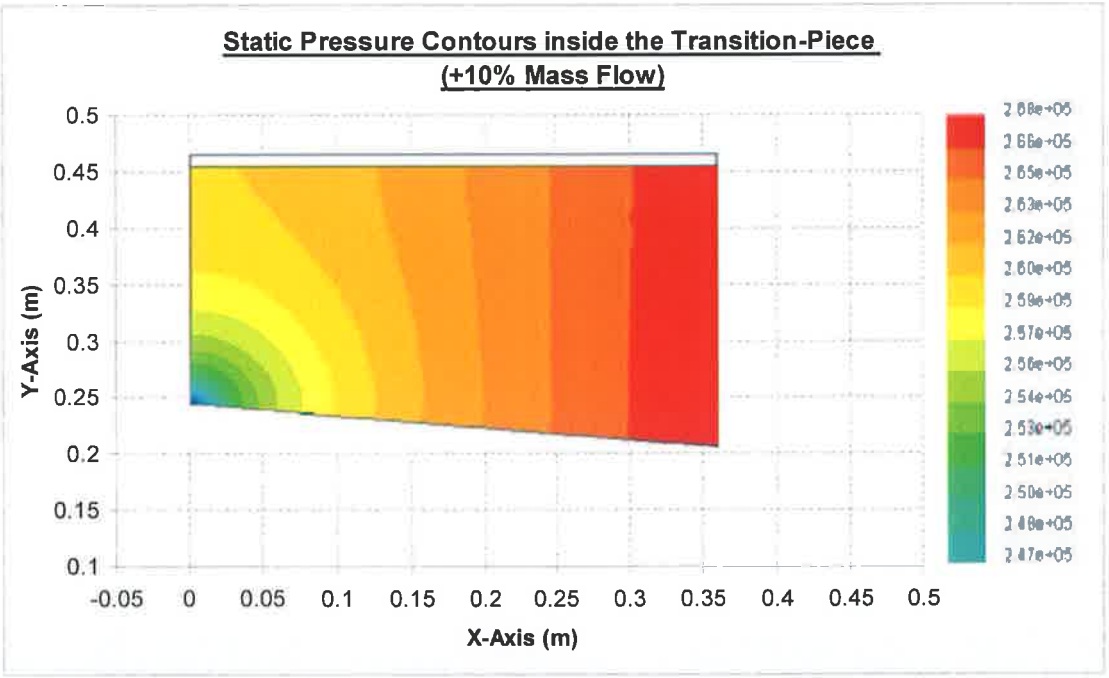

Figure 36, Pressure contours for +10% of nominal mass flow rate. Pressure unit is in Pa.

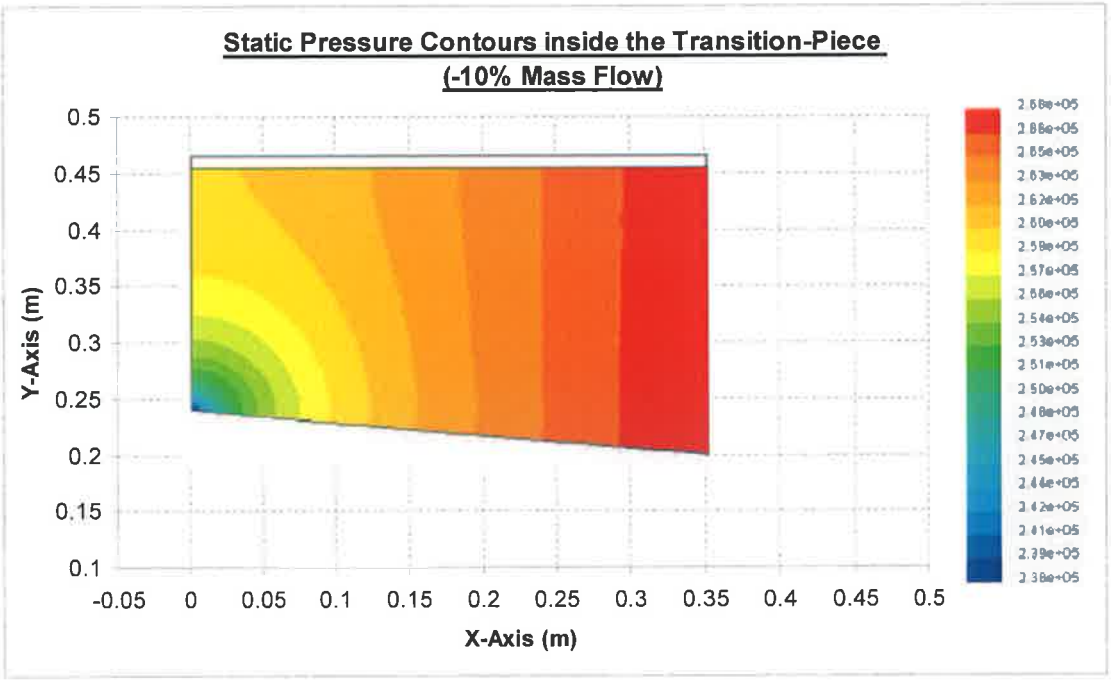

Figure 37, Pressure contours for -10% of nominal mass flow rate. Pressure unit is in Pa.

Figures 38 and 39 show the static temperature contours in the outer casing of the transition-piece for ±10% of the nominal flow rate variation. It was noted that, there is no notable difference in the temperature distribution and magnitude between the two cases, as well as between the mass flow rate variation cases and the base case. The main feature of the static temperature distribution in the transition-piece casing that, the temperature attains high values at the entry region of the casing, and as the distance in the axial direction increases towards the exit, the temperature reduces to within 20°C. It should be noted, at the inlet, natural convection is considered, since the transition- piece is being exposed to the atmosphere.

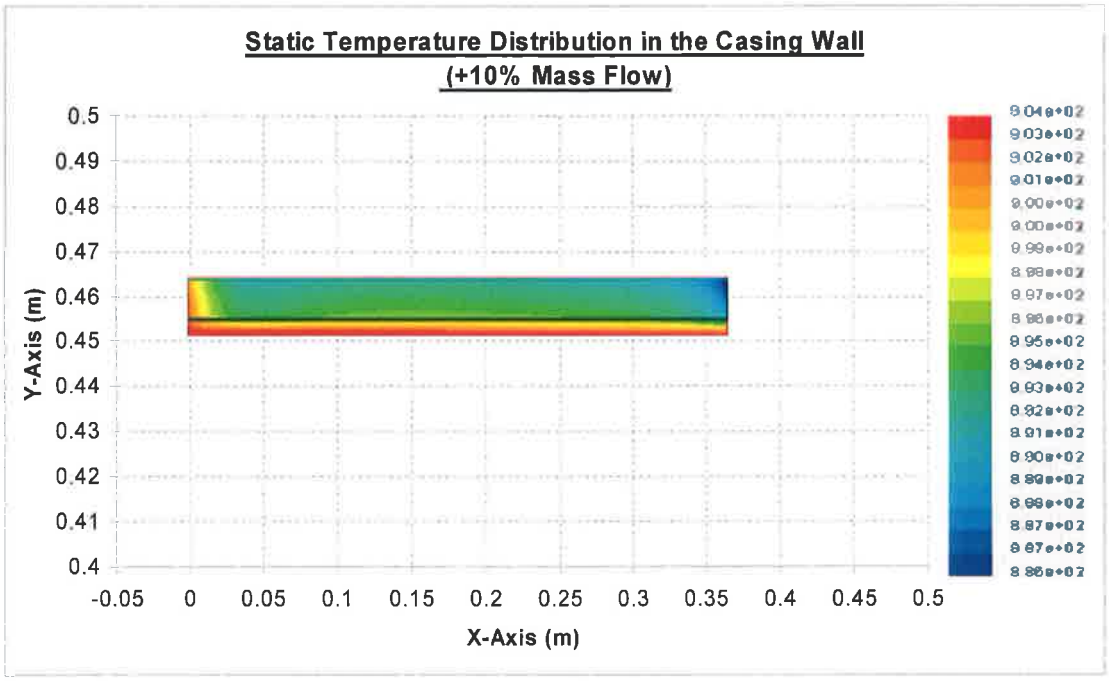

Figure 38, Temperature contours the outer casing for +10% of nominal mass flow rate. Temperature unit is in K.

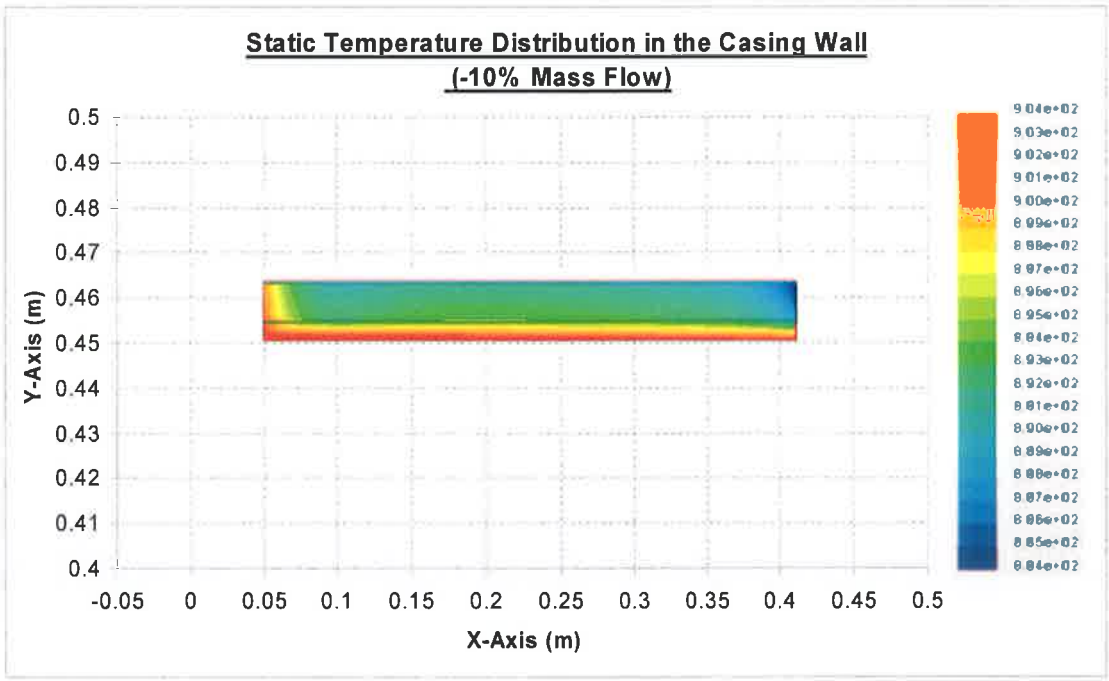

Figure 39, Temperature contours the outer casing for -10% of nominal mass flow rate. Temperature unit is in K.

The variation of the static temperature in the transition-piece along the axial direction is also evident from Figures 40 and 41. The temperature gradient is high at the entry and exit regions of the transition-piece. This indicates a high rate of energy diffusion from the transition-piece outer surface. In the case of -10% of mass flow rate, the temperature reduces slightly in the transition-piece. This is due to heat transfer from the high temperature fluid to outer casing. In this case, low mass flow rate at high temperatures reduces the convection heat transfer from the fluid to the transition-piece outer casing.

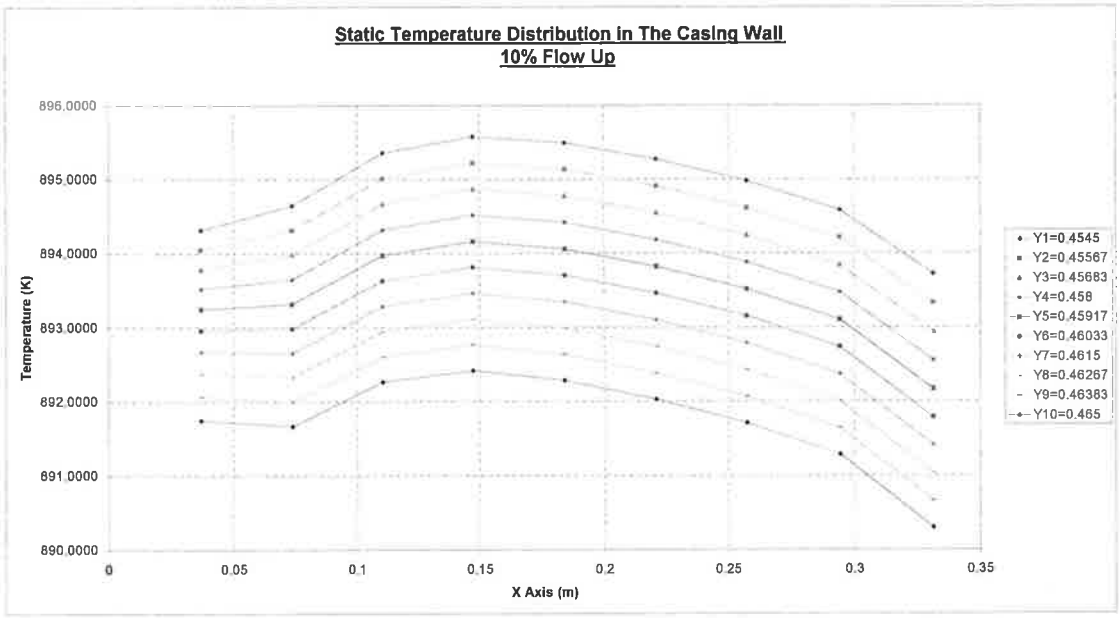

Figure 40, Temperature distribution the outer casing for +10% of nominal mass flow rate at different radial locations.

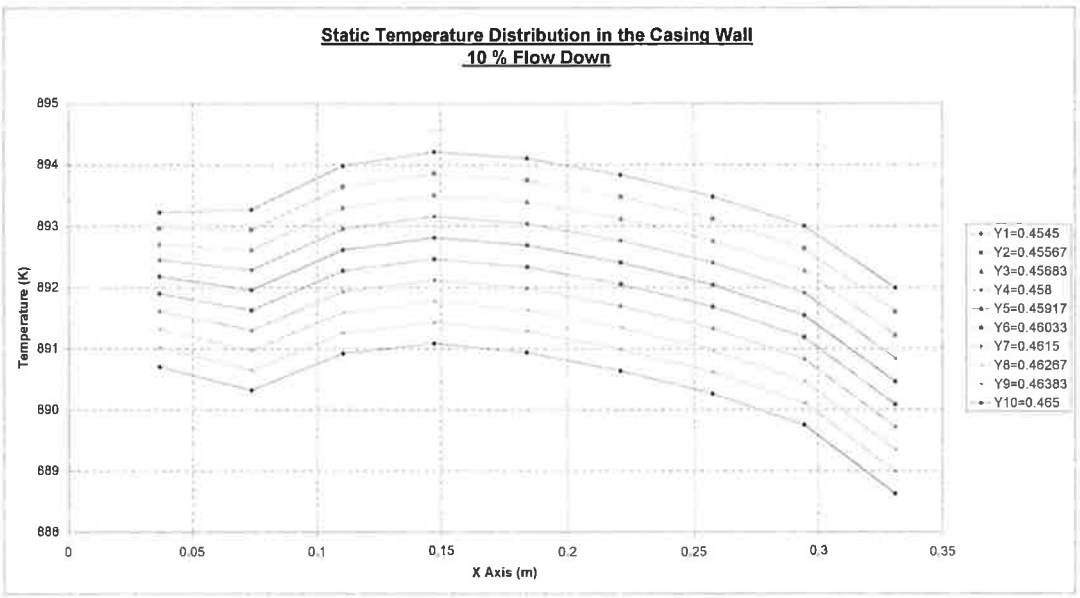

Figure 41, Temperature distribution in the outer casing for -10% of nominal mass flow rate at different radial locations.

Figures (42,43 and 44) show thermal stresses developed for ±10% mass flow rates in the outer casing at different planes. The axial stress component at the entry and exit of the outer casing of the transition piece attain high values and this is mainly due to high temperature gradients in this region. This situation is also true for radial stress. The magnitude of radial and axial stress differs in this region is due to the difference in the temperature gradient in the two cases (i.e. ±10% mass flow variation). The axial stress is compressive, while radial stress is compressive within the vicinity of the entry region, and becomes tensile in the region next to the entry. The compressive nature of the axial stress is associated with the axial expansion of the transition-piece as stated in section 5.2 for the base case. In the case of the radial stress component, radial expansion of the transition piece, next to the entry and exit regions, enables it to develop small tensile stress components in this region. Aside from the entry and exit regions, axial and radial stress components remain almost constant along the axial direction. This is due to the temperature gradient, which remains almost the same in this region. The magnitude of radial stress component becomes zero, due to expansion of the outer casing, while the axial stress component remains compressive in this region. The magnitude of the stress component does not exceed the yielding limit of the substrate material, indicating that plastic deformation, particularly at the entry and exit regions of the transition piece is

unlikely. The trend of von-Mises stress is the same for the two cases (i.e. ±10% mass flow variation). The magnitude of the stress components in both cases is the same, which indicates the insignificant effect of the flow variation in that range on the thermal stresses developed in the transition piece.

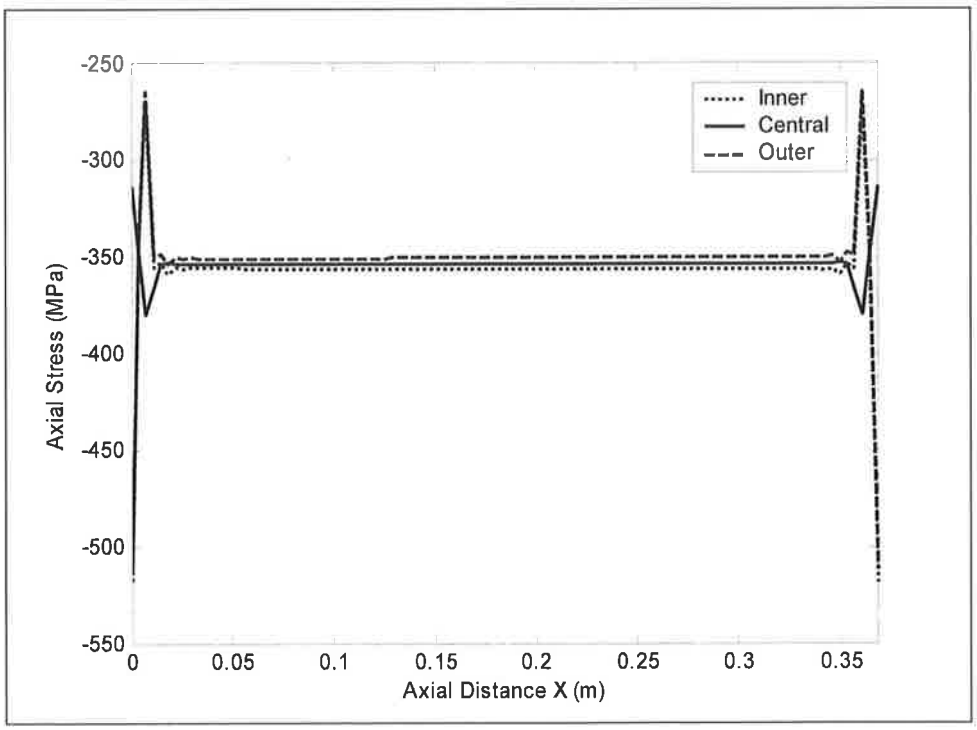

Figure 42, Axial stress component for the ±10 mass flow rate cases.

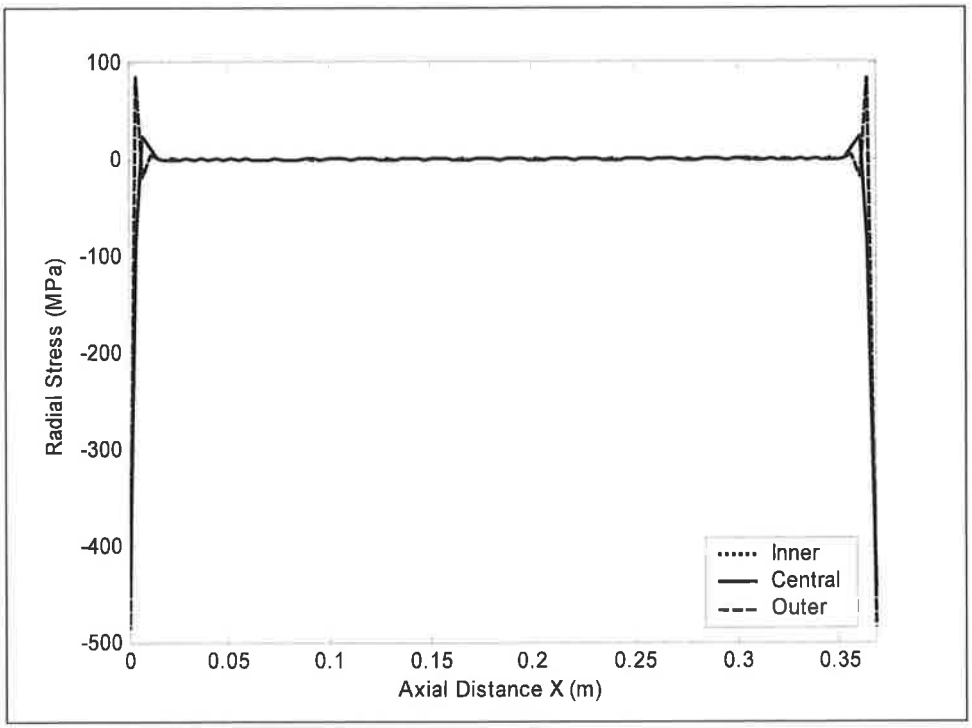

Figure 43, Radial stress component for the ±10 mass flow rate cases.

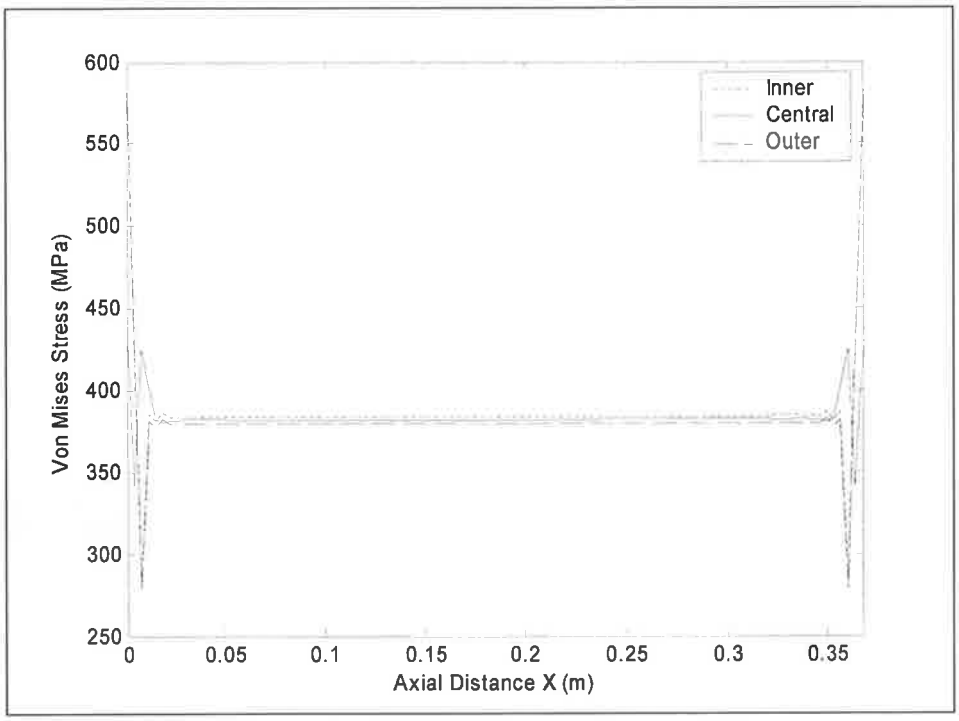

Figure 44, von-Mises stress at the inner wall for the ±10% mass flow rate cases.

5.4 EFFECT OF ENTRY TEMPERATURE VARIATION ON THE THERMAL STRESSES DEVELOPED IN THE TRANSITION-PIECE CASING

The second operational parameter to be considered for evaluation of its effect on the thermally induced stresses in the transition-piece is the exhaust gas entry temperature. The variation of the entry temperature is due to varying output demand of the engine which is initiated by the change in fuel flow introduction to the combustion chamber. In this section, the entry temperature to the transition-piece is varied by ±10% from the nominal value (i.e. Table 5).

Figures 45 and 46 show the velocity contours in the solution domain for the +10% and -10% of the nominal entry temperature respectively. Comparing the two Figures it can be noted that there is a significant difference in the flow structure and the velocity magnitude between the two conditions. For the +10% entry temperature case, the flow velocity magnitude is the highest in all the cases investigated (i.e. over 20% higher than the base case). This can be related to the increase in kinetic energy of the flow due to the increase in temperature at the entry of the transition-piece. In spite of the velocity magnitude increase relative to other investigated cases, the flow velocity magnitude decreased gradually in the axial direction towards the transition-piece exit plane, due to the conical shape of the transition-piece. This is true all over the transition-piece for both cases, with exception of the lower corner of the transition-piece casing, where the velocity magnitude reached the maximum value of 460 m/s in the +10% entry temperature case, and this can be related to enforcement of the exit boundary conditions (i.e. pressure outlet) in this case.

In both cases, the effect of convection acceleration is evident, as the velocity magnitude at the entry region is higher relative to other locations within the transition-piece. In the case of -10% entry temperature case, although there is a considerable difference in the flow structure inside the transition-piece between the two cases of ±10% entry temperature, the flow structure is comparable to the previously investigated cases in sections 5.1 and 5.2.

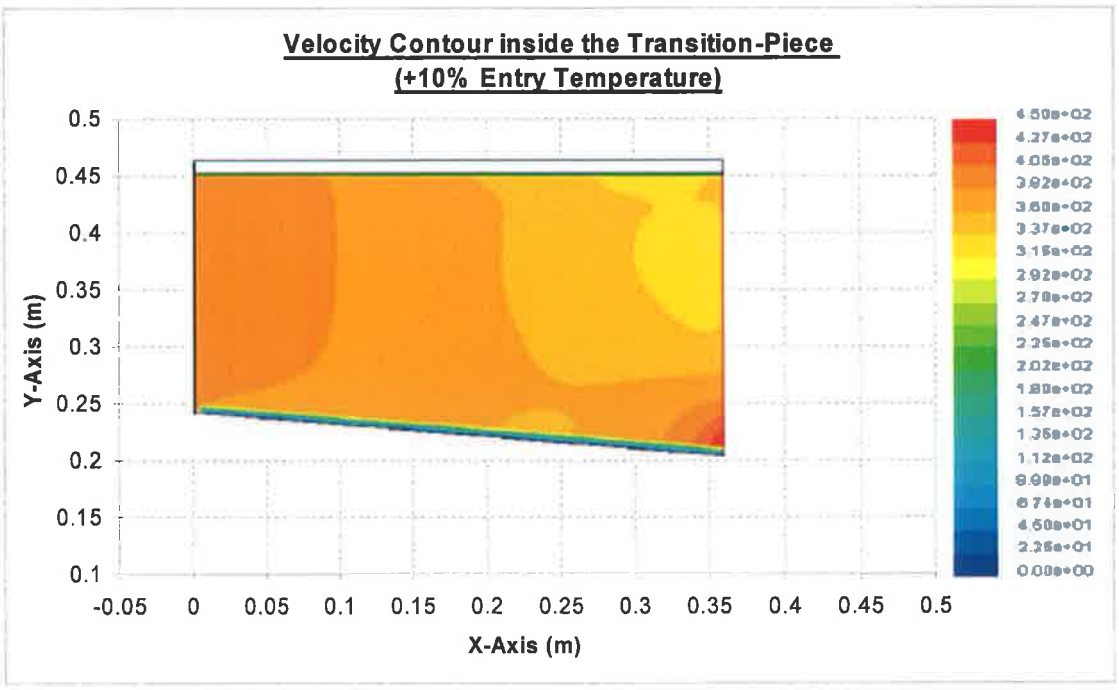

Figure 45, Velocity contours for +10% of entry temperature nominal value. Velocity unit is in m/s.

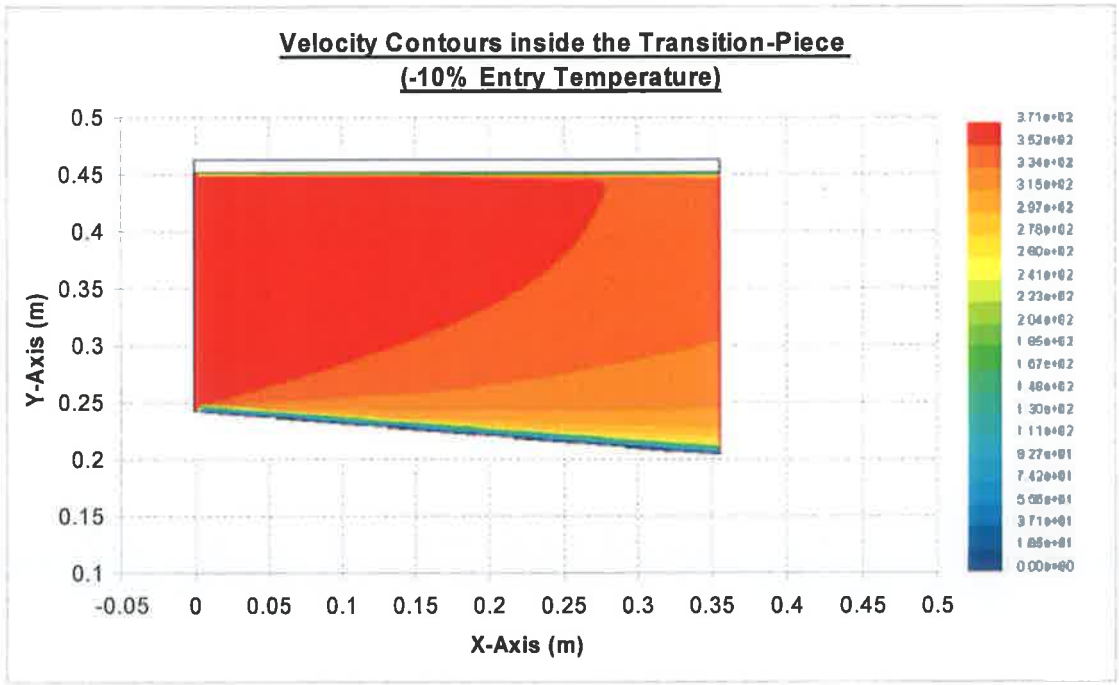

Figure 46, Velocity contours for -10% of entry temperature nominal value. Velocity unit is in m/s.

Figures 47 and 48 show pressure contours in the solution domain for ±10% of the entry temperature nominal value. For both cases, there is a pressure reduction in the entry region of the transition-piece close to the inner wall. This occurs because of the flow expansion in this region as discussed in sections 5.2 and 5.3. In the case of +10% of the entry temperature over the nominal value, the magnitude of the pressure increase is notably higher than the one encountered in the case of the -10% entry temperature nominal value, with a notable difference in the pressure distribution. This can be related to the pressure temperature relationship stated by the gas law.

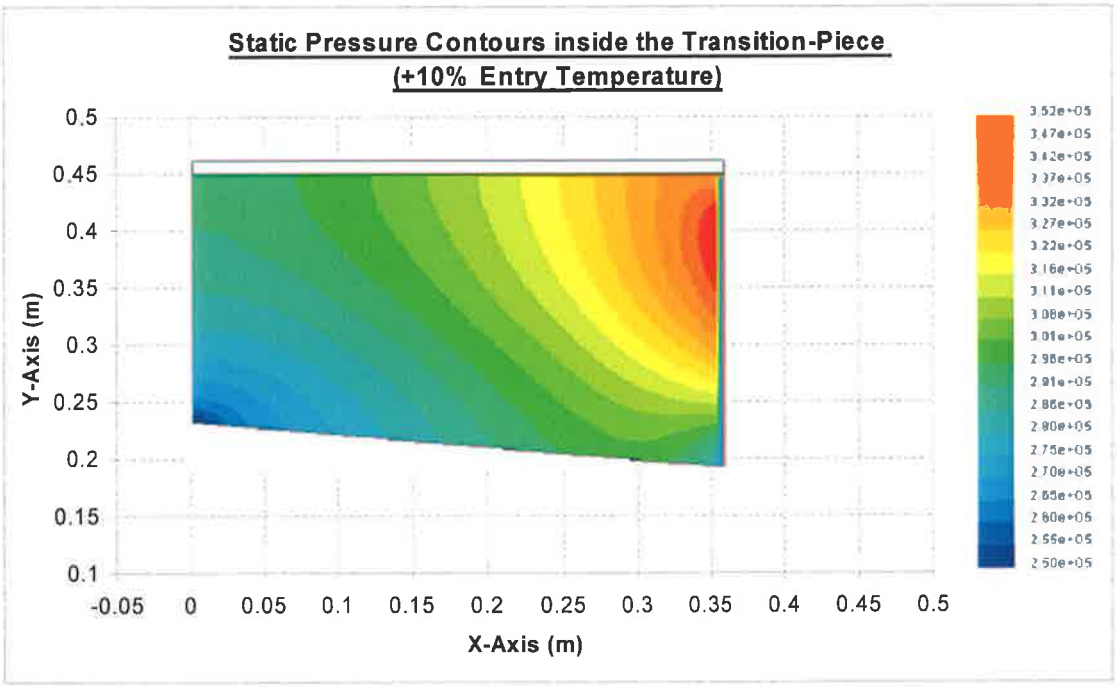

Figure 47, Pressure contours for +10% of entry temperature nominal value. Pressure unit is in Pa.

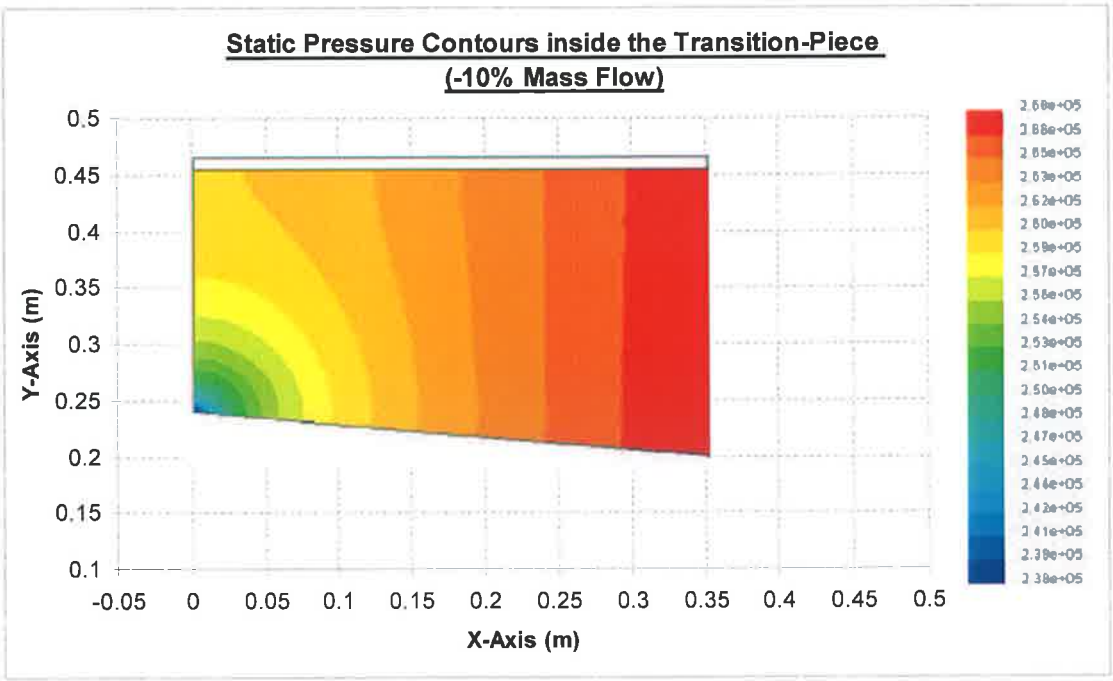

Figure 48, Pressure contours for -10% of entry temperature nominal value. Pressure unit is in Pa.

Figures 49 and 50 show the static temperature contours in the casing of the transition-piece for ±10% of the nominal entry temperature variation. The temperature attains high values at the entry region and as the distance in the axial direction increases towards the exit of the transition-piece, temperature reduces to within 27°C. It should be noted, that at the inlet natural convection is considered, due to the transition-piece being exposed to the atmosphere, in the same way as the previously investigated cases.

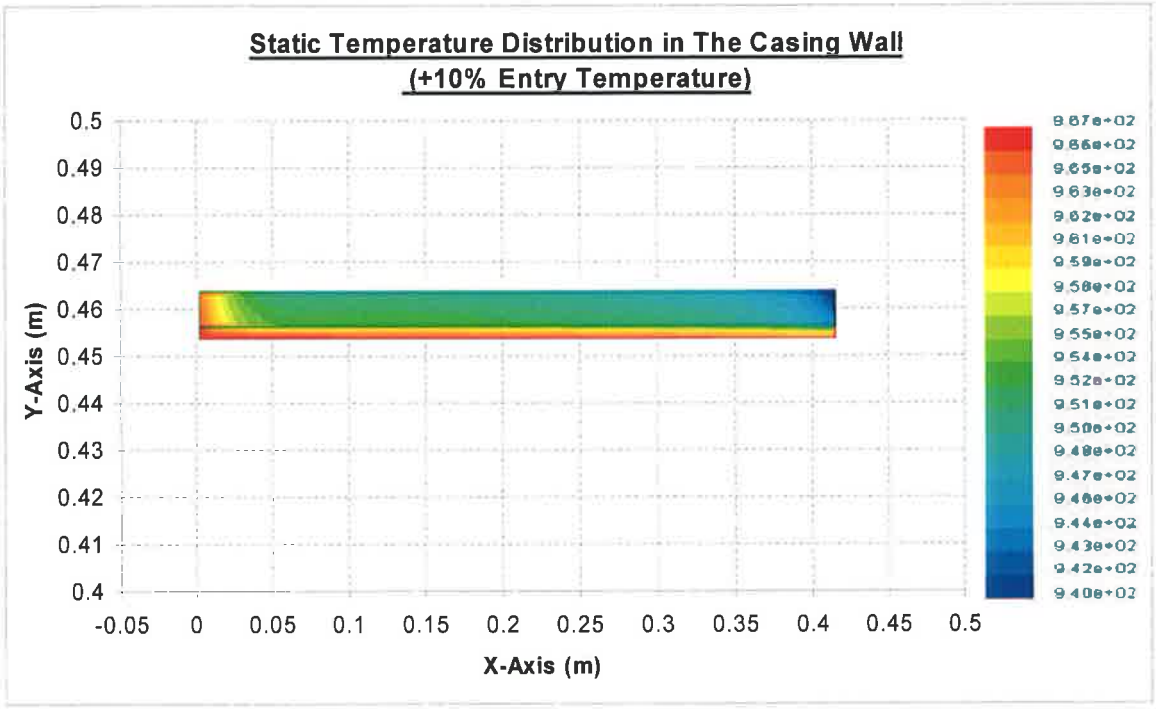

Figure 49, Temperature contours for +10% of entry temperature nominal value. Temperature unit is in K.

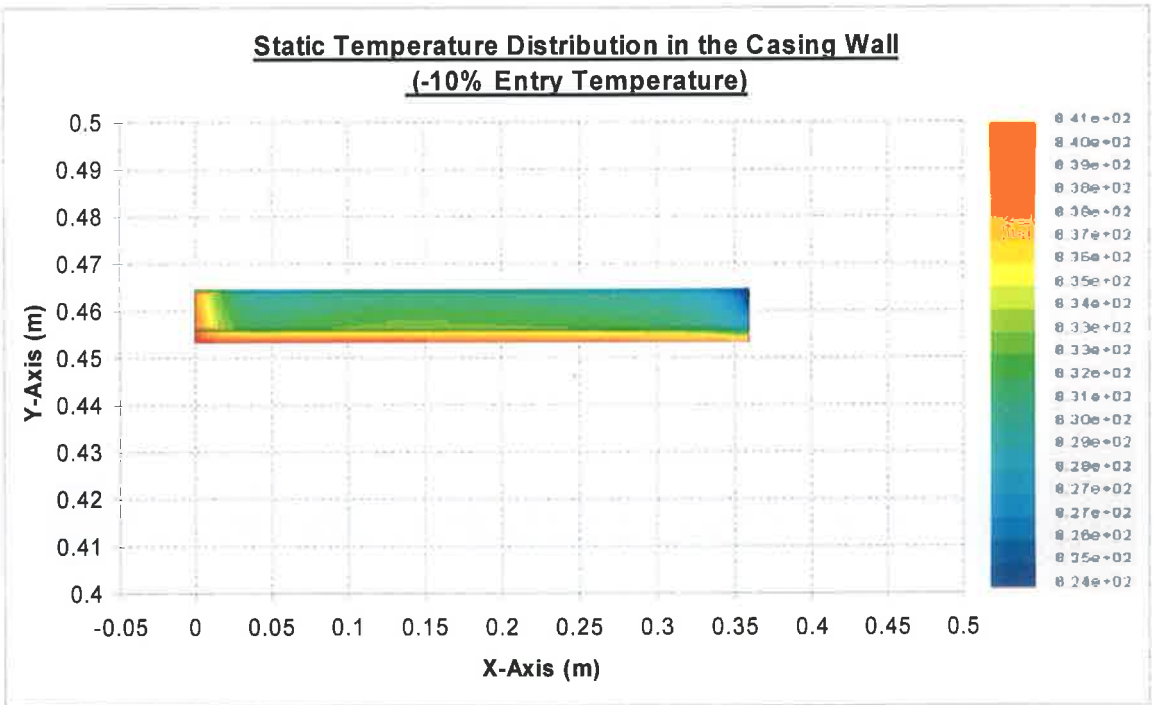

Figure 50, Temperature contours for -10% of entry temperature nominal value. Temperature unit is in K.

Variation of temperature in the transition-piece casing along the axial direction is also evident from Figures 51 and 52, in which the temperature variation is shown. In the case of -10% of entry temperature, temperature reduces in the transition-piece along the axial direction more than the reduction attained in the +10% case. This is due to the high heat transfer rate from the outer casing, which lowers the temperature within the transition-piece.

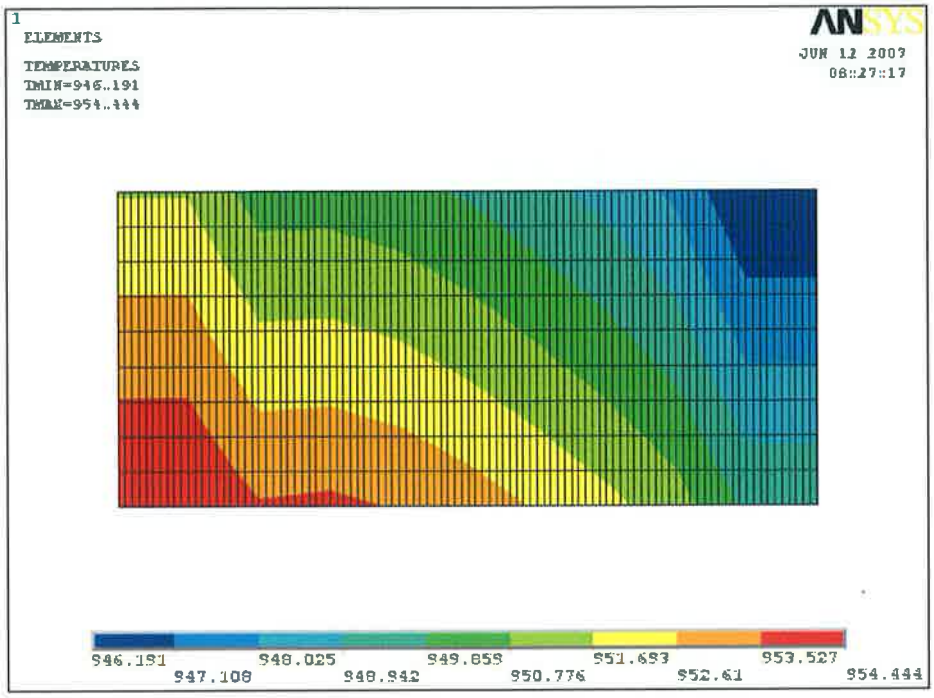

Figure 51, Temperature distribution the outer casing for +10% of entry temperature nominal value along the axial direction. Temperature unit is in K.

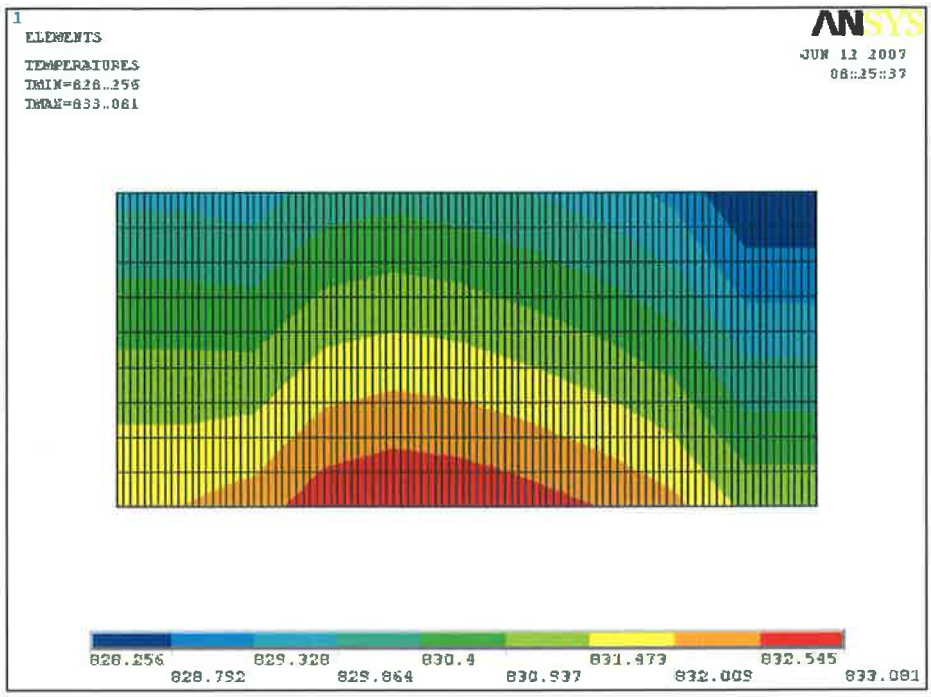

Figure 52, Temperature distribution the outer casing for -10% of entry temperature nominal value along the axial direction. Temperature unit is in K.

Figures 53 to 58 describe the development of the thermally induced stresses in the transition-piece casing, at different radial planes, due to the variation of the transition-piece entry temperature within ±10% of the nominal entry temperature value. The axial stress component of the thermally developed stress, in Figure 53 and 54 are showing uniform stress levels all along the axial direction in the three radial locations. The only exception is at the inlet and exit where the stress level is showing a notable change due to the change in the temperature gradient at those locations. It is also noted that the shape and nature of the stresses are similar to the resulting stresses in sections 5.2 and 5.3 with a differing magnitude, indicating the change in the material thermal expansion, due to the change in the temperature influencing the transition-piece casing. This situation is also true for radial stress variation in Figures 55 and 56 as the stress level maintains the zero value all along the axial direction, due to freedom of the material to expand radially. The exception to the zero level stress is noted at the entry and the exit regions where the stress level attains a slight change, due to the fixing at the both ends and suppression of the material expansion in both radial and axial directions. The magnitude of stress

components still do not exceed the yielding limit of the substrate material, similar to the situation in sections 5.2 and 5.3, indicating that plastic deformation of the transition-piece is unlikely. There is no change in the trend of von-Mises stress (Figures 57 and 58); however, the only notable difference is in their magnitudes.

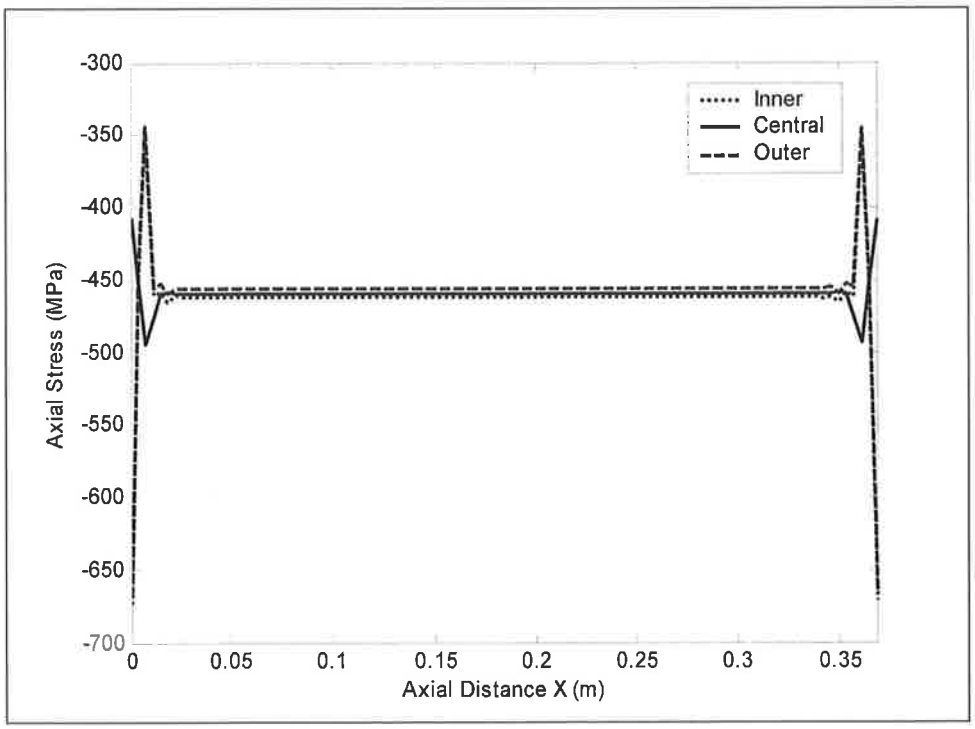

Figure 53, Axial stress component along the axial direction at three radial locations for +10% of entry temperature nominal value.

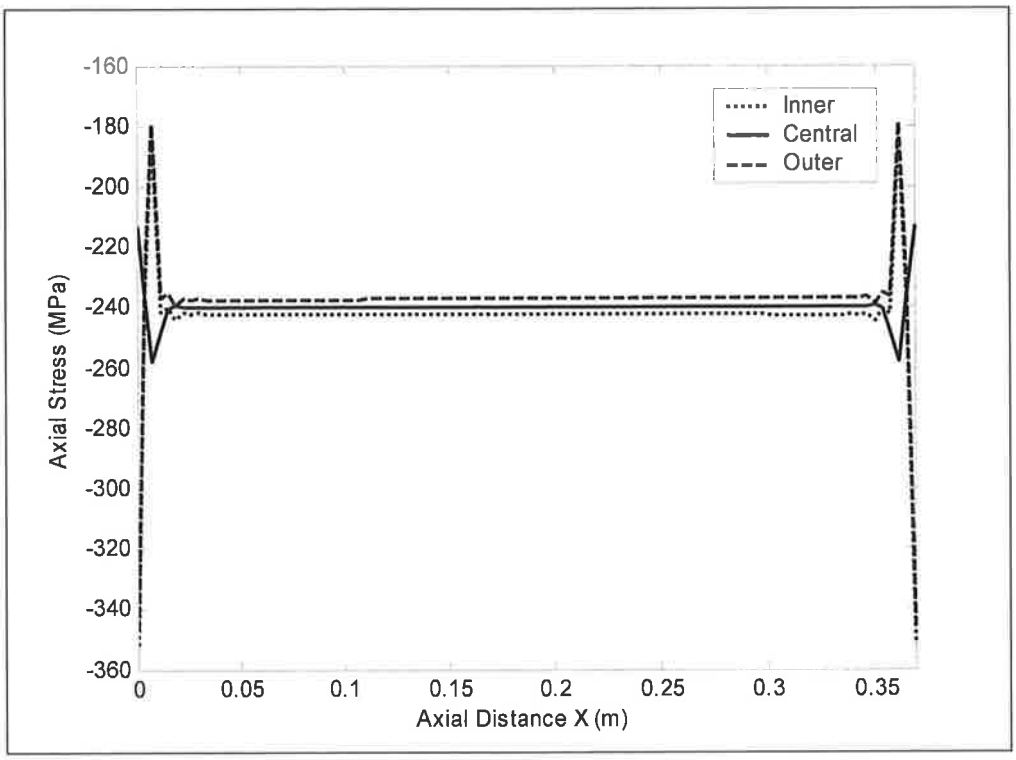

Figure 54, Axial stress component along the axial direction at three radial locations for -10% of entry temperature nominal value.

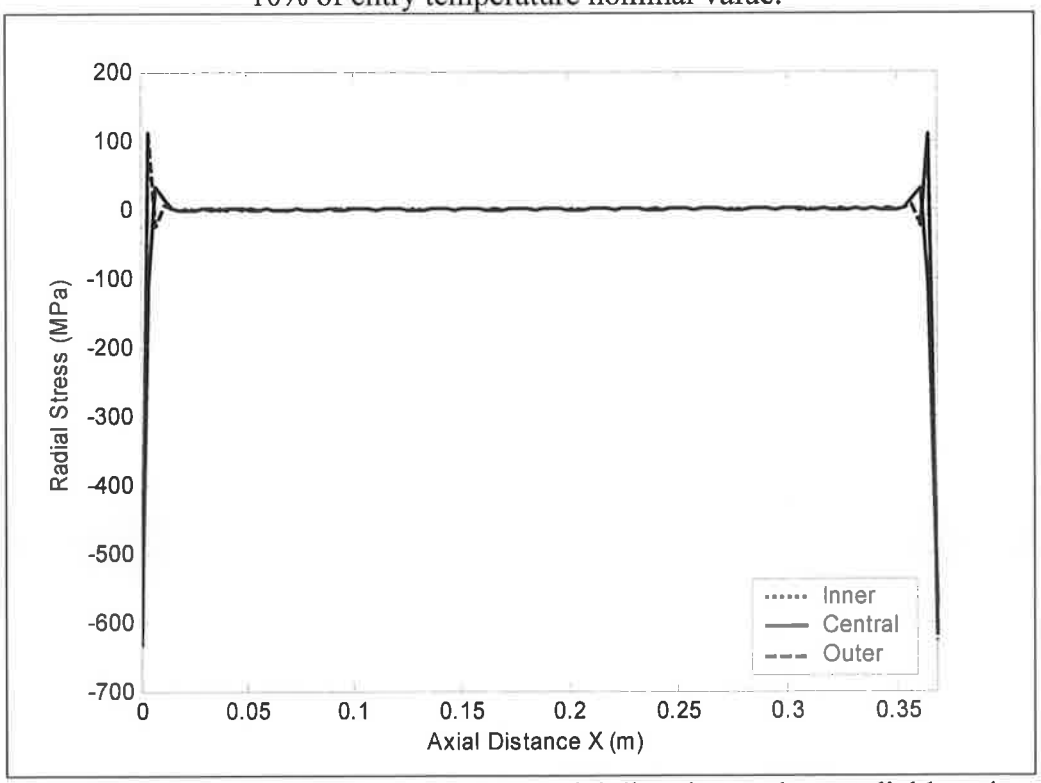

Figure 55, Radial stress component along the axial direction at three radial locations for +10% of entry temperature nominal value.

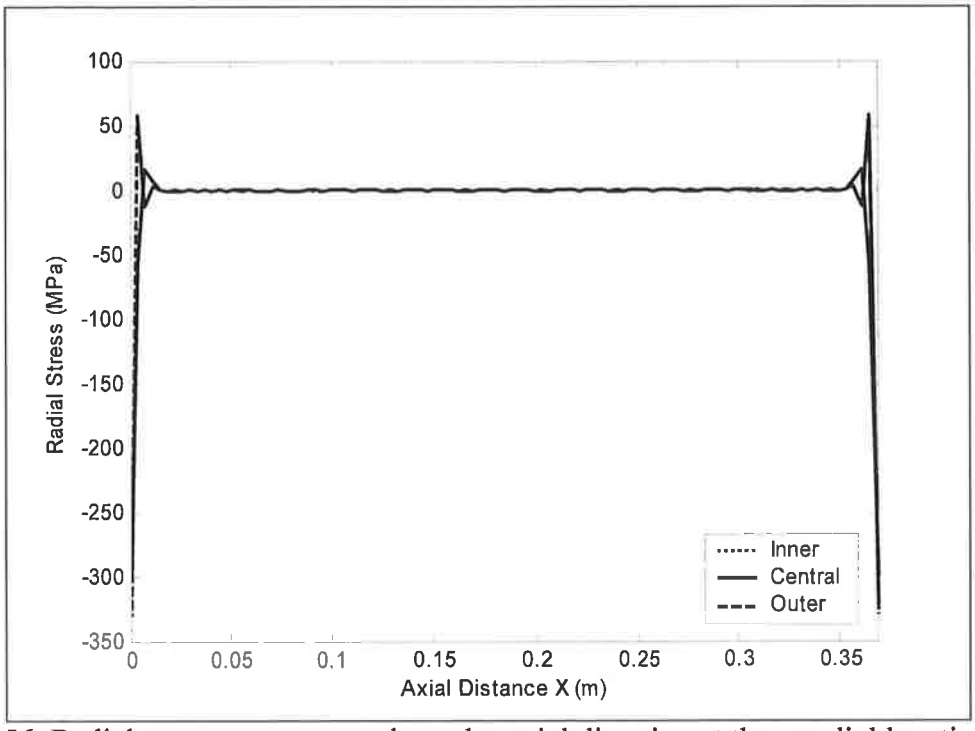

Figure 56, Radial stress component along the axial direction at three radial locations for -10% of entry temperature nominal value.

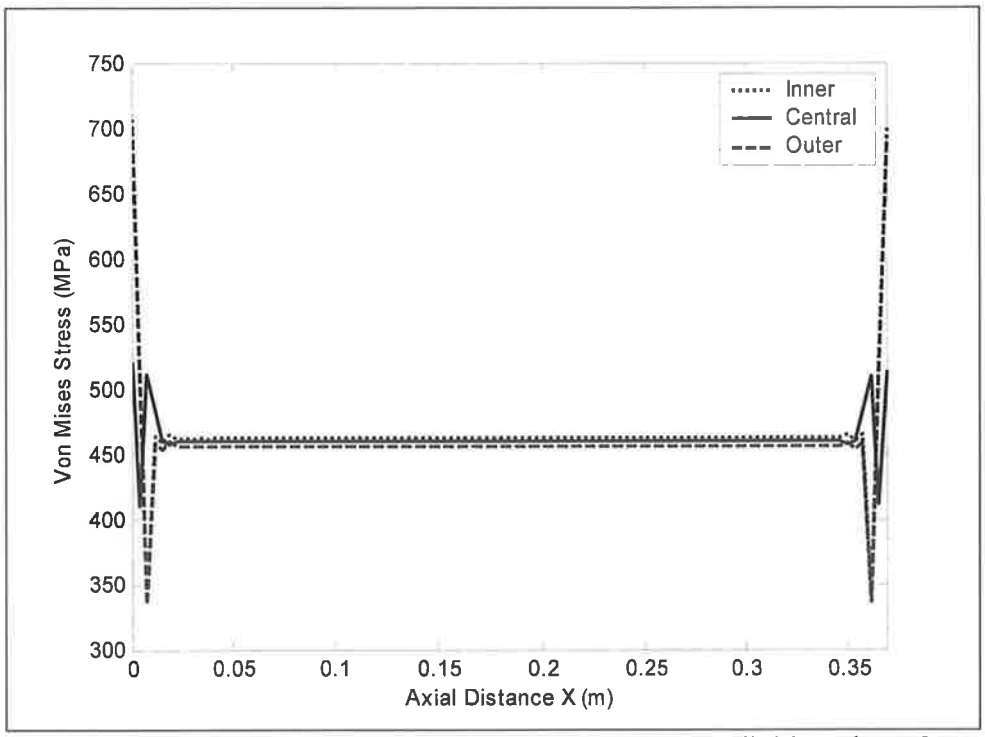

Figure 57, von-Mises stress along the axial direction at three radial locations for +10% of entry temperature nominal value.

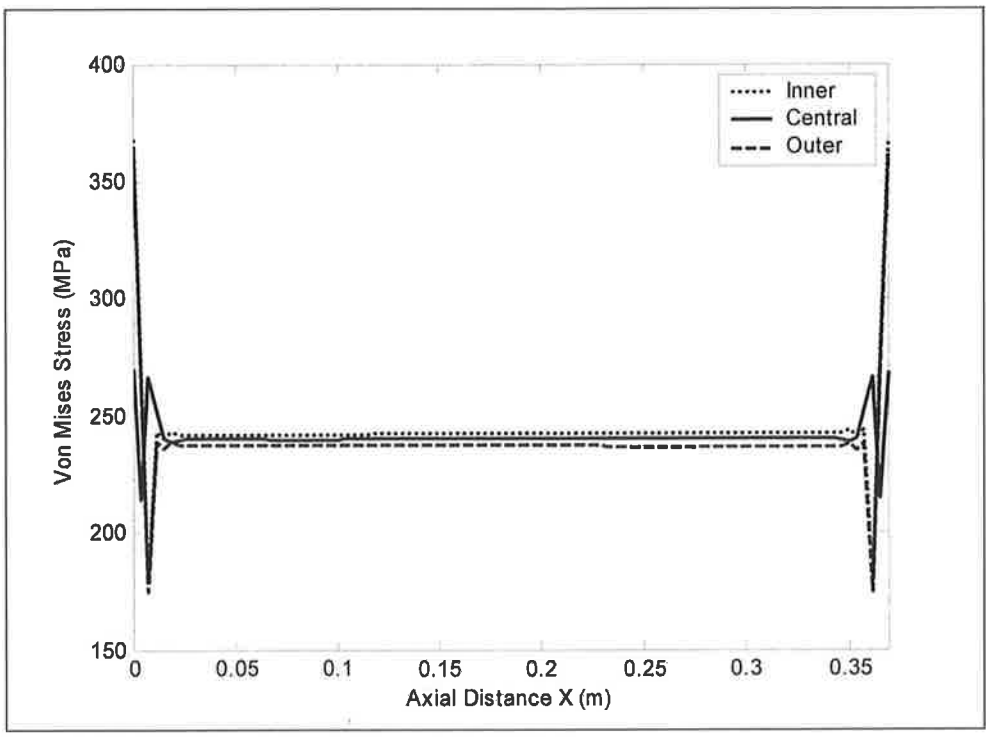

Figure 58, von-Mises stress along the axial direction at three radial locations for -10% of entry temperature nominal value.

5.5 INFLUENCE OF MATERIAL PROPERTIES ON THE INDUCED THERMAL STRESS LEVELS

To resemble the high temperature environment in which the transition-piece is operating, the substrate material (A286 Iron-Base Superalloy) was heat treated to 950 °C for 1.5 hours. The tensile and three-point bending tests were carried out to determine the modulus of elasticity for the material in the as received and heat treated conditions. The modules of elasticity for both conditions were accommodated in the simulation after the incorporation of the elevated temperature operation effect to predict numerically the thermally developed stress field in the transition-piece casing. Microstructural changes in the alloy before and after the heat treatment were examined by SEM, EDS, and XRD.

Figures 59 and 60 show SEM micrograph of the as received and heat treated A286 alloy. The untreated alloy shows almost equiaxed grain structure with the average grain diameter of about 30 μm. However, the grain size increases significantly after the heat treatment and uni-equiaxed grains with different sizes are formed. The finer grains are smaller than the original columnar grains. The increase in the grain size is responsible for low hardness after the heat treatment process. It is also possible that γ' depletion near the grain boundary lowers the brittleness of the material after the heat treatment. Close examination of the grain boundaries suggests that locally scattered and discontinuous formation of carbides occurred. Although grain boundary carbides formation increases the brittleness while lowering the ductility, locally discontinuous formation minimizes this effect.

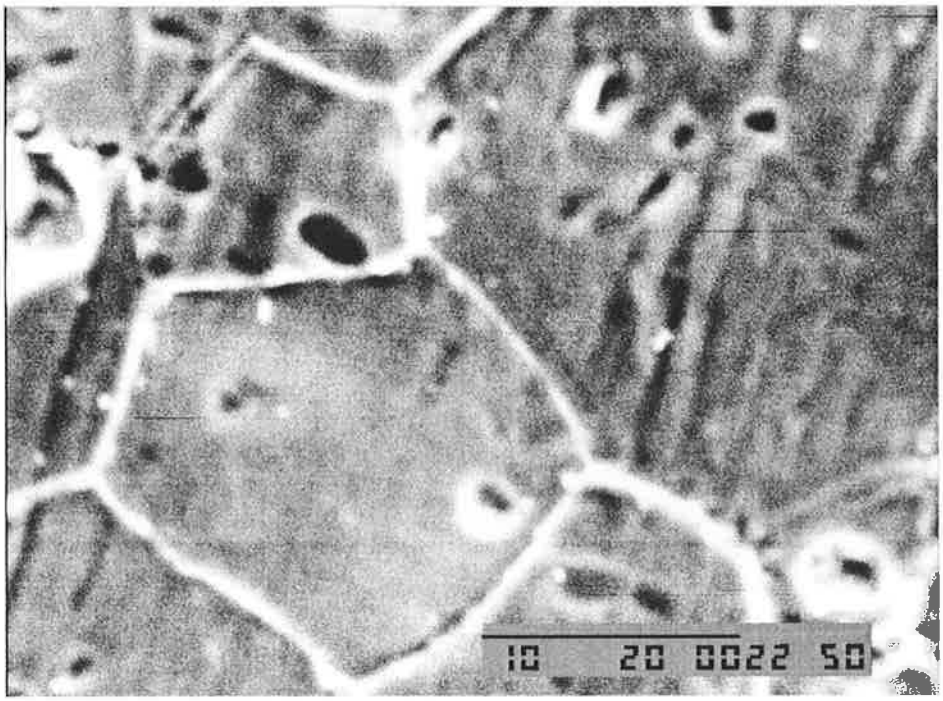

Figure 59, SEM micrograph of as received material.

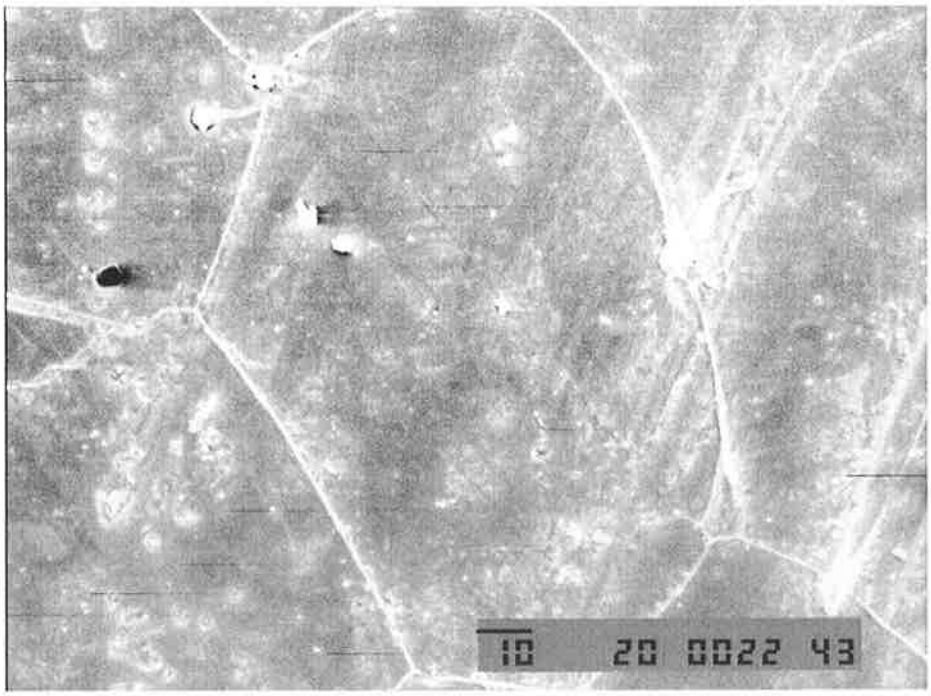

Figure 60, SEM micrograph of heat treated material.

Table 10 (Section 4.5.1) gives three-point bending test parameters and the results of the elastic modulus while table 11 (Section 4.5.2) gives the tensile test results. It can be observed that the modules of elasticity determined from the three-point bending and the tensile tests are in good agreement. The elastic limit of the alloy decreases significantly after the heat treatment process, and the increase in ductility is attributed to grain coarsening after the heat treatment.

In addition, short duration heat treatment causes dissolution of γ' and formation of η-phase (hexagonal closed- packed- hcp-Ni_3T_i phase) as seen from the XRD result in Figure 61, lowering the mechanical performance of the material. The formation of η-phase at the grain boundary can also act as the nucleation site of the crack where the material fails. This situation is observed during the three-point bending test, in particular at the tensile surface of the specimen.

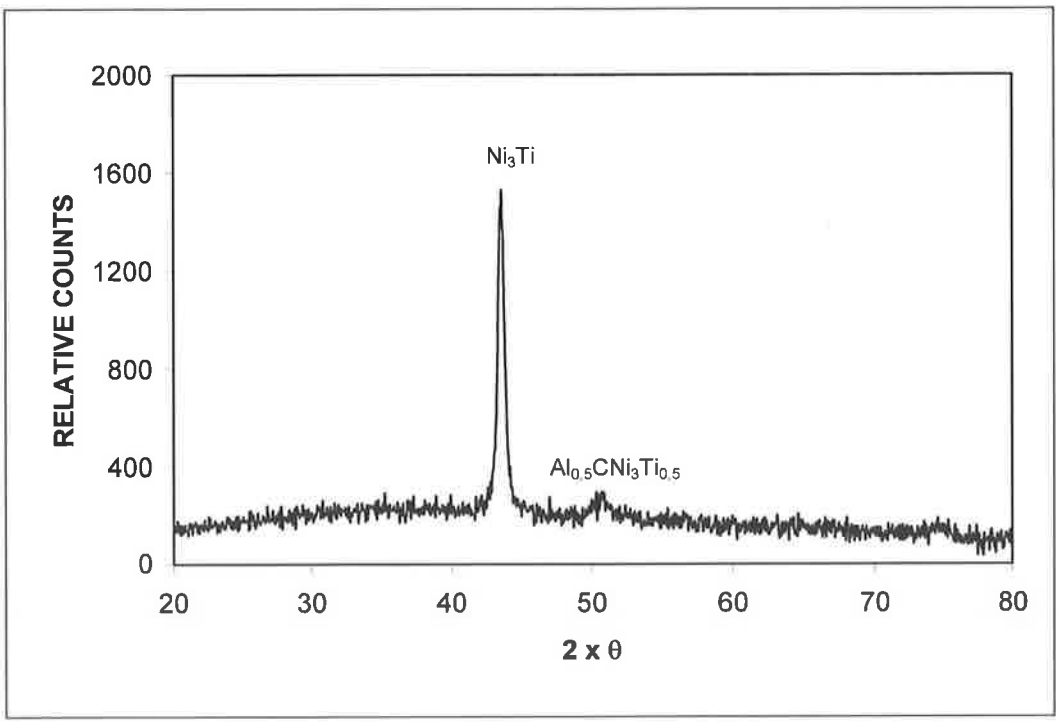

Figure 61, XRD results for the heat treated work piece.

Using the Modulus of Elasticity results from the three-point bending tests and tensile tests in tables 10 and 11 as input for the numerical simulation, showed the difference in the level of the thermally developed stresses between the as received and heat treated material. Figures 62-77 show the Von-Mises stress along the axial direction in the casing of the transition-piece, at different radial planes, using the Elastic Modulus for the as received material (i.e. 2.07 GPa) and the heat treated material (i.e. 1.38 GPa), determined from the tensile and the 3-point bending tests after the heat treatment process.

Figures 62-66 describe the von-Mises stress along the axial direction in the outer wall of the transition-piece. From Figures 62-64 it can be noted that the levels of the thermally developed stresses are the same for the first three cases (i.e. base, +10% mass flow rate and -10% mass flow rate), for the as received and for the heat treated material conditions. The von-Mises stress level for the as received material condition for the three cases was 350 MPa in the middle section, and approximately 500 MPa maximum and 250 MPa minimum at the edges of the transition-piece. For the heat treated material condition the level of Von-Mises stress was 270 MPa in the middle section and reached approximately a maximum of 420 MPa and a minimum of 210 MPa at the transition-piece edges.

In Figure 65, it can be noted that the level of the thermally developed stress for the as received material changes from approximately of 450 MPa in the middle section to a maximum of 550 MPa and a minimum of 340 MPa when the entry temperature to the transition-piece is increased by 10% from the nominal value. However, for the heat treated condition, the thermally developed stress level of 350 MPa in the middle section changes to a maximum of 450 MPa at the fixed ends, and reduces to approximately 275 MPa in the vicinity of the fixed ends.

For Figure 66, the von-Mises stress in the middle section for the as received material attains a value of 240 MPa which reduces to a value of 160 MPa in the section before the fixed ends and reaches a maximum of 350 MPa at the fixed ends. Meanwhile, the value of the von-Mises stress value at the middle section showed a value of approximately 180

MPa reduces to 140 MPa in the vicinity of the fixed ends and climbs up to a maximum value of 275 MPa at the fixed ends.

This noted change in the thermally developed stresses is due to the change in the transition-piece entry temperature as introduced in the simulation (i.e. ±10 of the nominal entry temperature). The high values attained by the von-Mises stress at the edges of the transition-piece are due to the attainment of the high temperature gradient in these regions and the mechanical constraints at both ends of the transition-piece. In the simulation, both ends of the transition-piece were fixed to resemble the actual situation; in which case, one end of the transition-piece was joined to the gas generator exit and the other was joined to the power turbine inlet. It was noted that the change in the level of the von-Mises stress developed is related to the change noted earlier in the Modulus of Elasticity between the as received and the heat treated material.

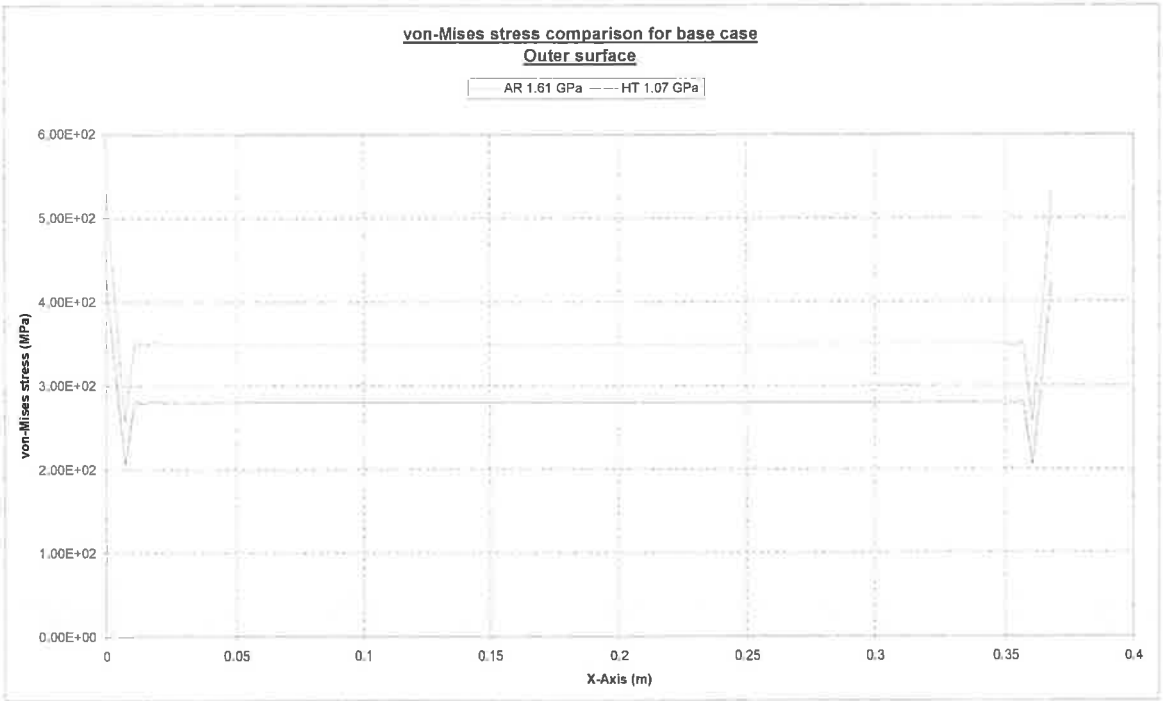

Figure 62, von-Mises stress along the axial direction in the in the outer wall of the casing for the base case.

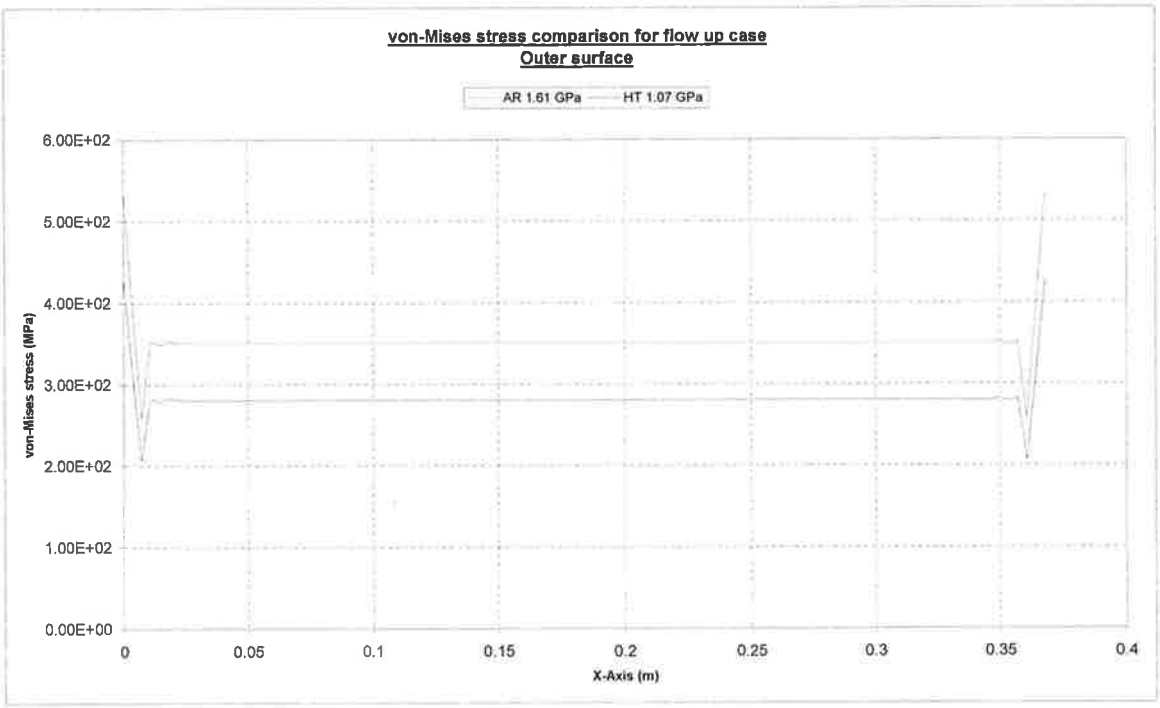

Figure 63, von-Mises stress along the axial direction in the outer wall for the +10% mass flow rate case. AR represents as received while HT corresponds to heat treatment.

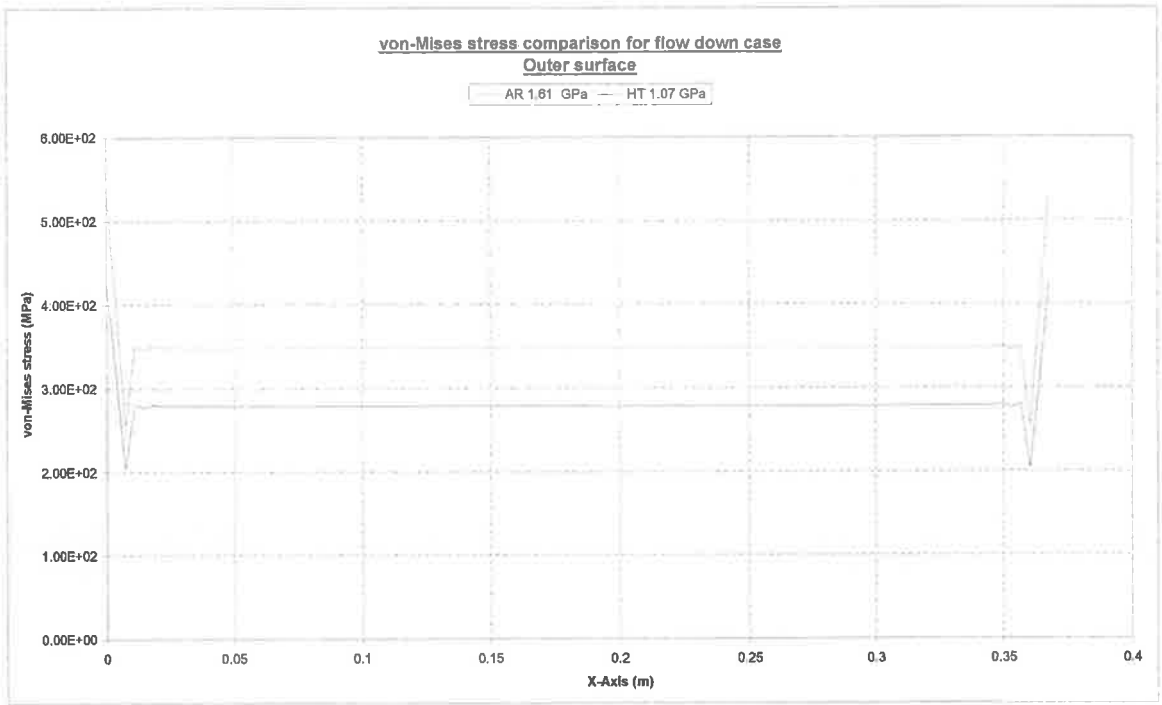

Figure 64, von-Mises stress along the axial direction in the outer wall for the -10% mass flow rate case. AR represents as received while HT corresponds to heat treatment

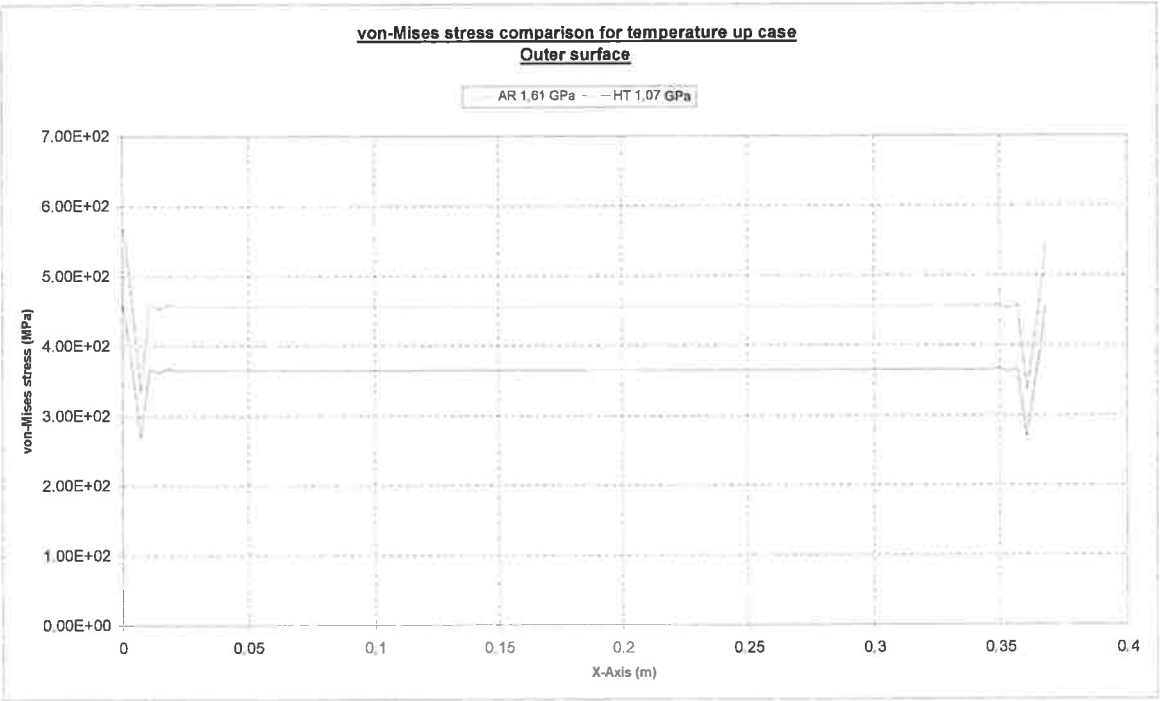

Figure 65, von-Mises stress along the axial direction in the outer wall for the +10% entry temperature case. AR represents as received while HT corresponds to heat treatment.

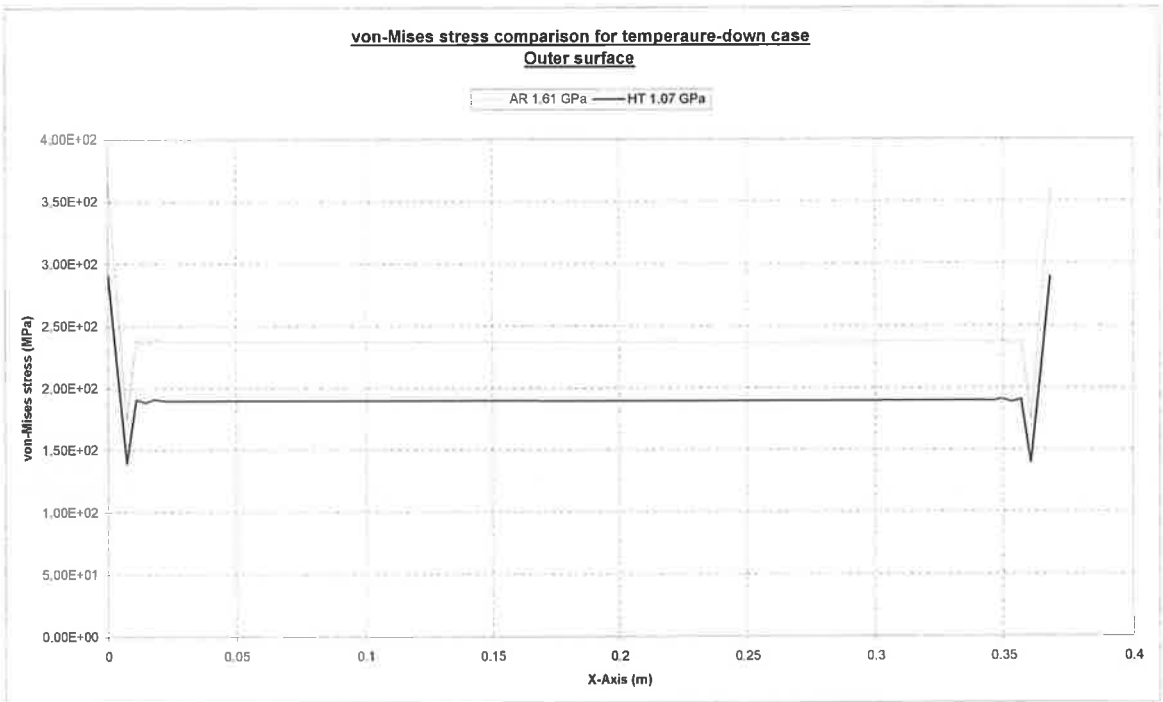

Figure 66, von-Mises stress along the axial direction in the outer wall for the -10% entry temperature case. AR represents as received while HT corresponds to heat treatment.

In the case of mid-plane (Figures 67-71), von-Mises stress attains high values at the fixed ends of the transition-piece. Therefore, similar observations can be made for Figures (67-69) as those made for Figures (62-64) concerning the first three cases (i.e. base, +10% mass flow rate and -10% mass flow rate). This is because of temperature distribution at the mid-plane which is similar to the temperature distribution of the outer wall. The von-Mises stress level in the middle section of the transition-piece of the three first cases is approximately the same at 350 MPa and 270 MPa for the as received and heat treated cases, respectively. While at the edges next to the fixed ends, the von-Mises stress level is a maximum of 390 MPa and a minimum of 200 MPa, for the as received case, and a maximum of 170 MPa and 250 MPa for the heat treated version.

In the case of entry temperature increase by 10% (Figures 70), the von-Mises stress distribution along the axial distance in the middle section of the transition-piece attains a value of 450 MPa and 350 MPa for the as received and heat treated material conditions, respectively. For the region at the fixed ends, the values differ significantly from that of the outer-plane in the same region, with a maximum of 520 MPa and a minimum of 410 MPa, for the as received material condition. For the heat treated condition the von-Mises stress level at the fixed ends reached a maximum value of 410 MPa and a minimum value of 340 MPa.

In Figure 71, it can be seen that the von-Mises stress level for the case of 10% reduction in entry temperature for the as received material was approximately 240 MPa in the middle section of the central plane and it peaks up to a maximum of 250 MPA and reduced to 220 MPa at the fixed ends region. While for the heat treated condition, the Von-Mises stress value was approximately 280 MPa at the middle section and a maximum of 220 MPa and a minimum of 175 MPa at the fixed ends.

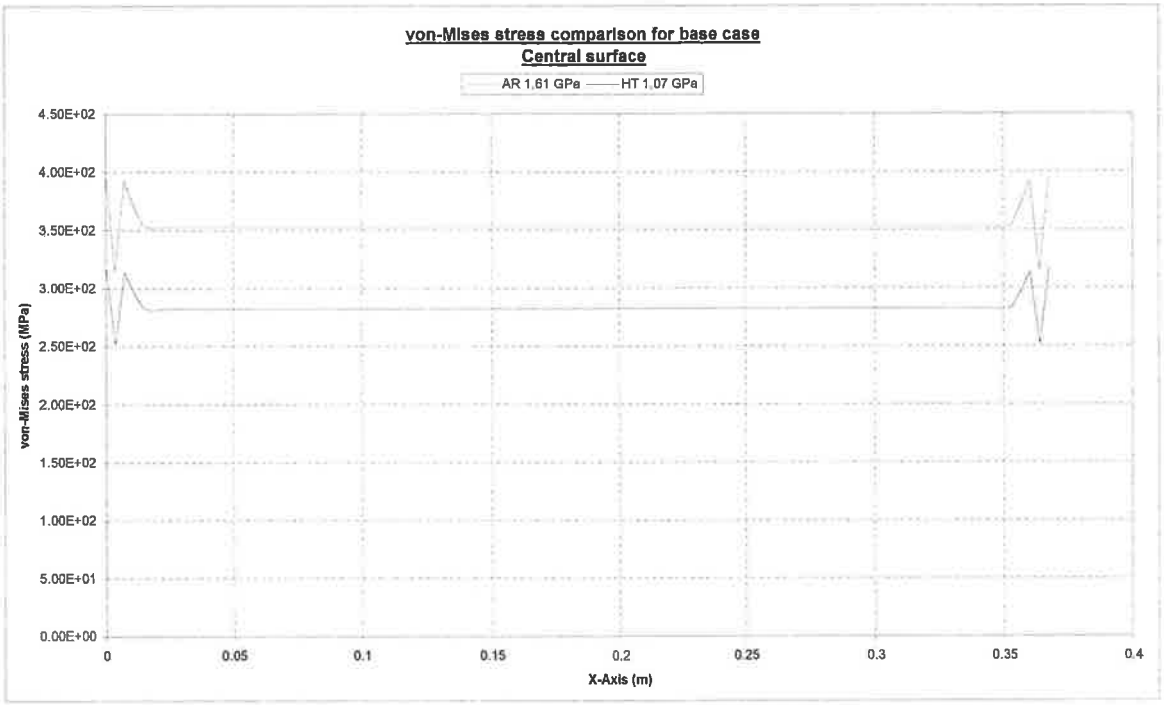

Figure 67, von-Mises stress along the axial direction in the mid-plane of the casing for the base case. AR represents as received while HT corresponds to heat treatment.

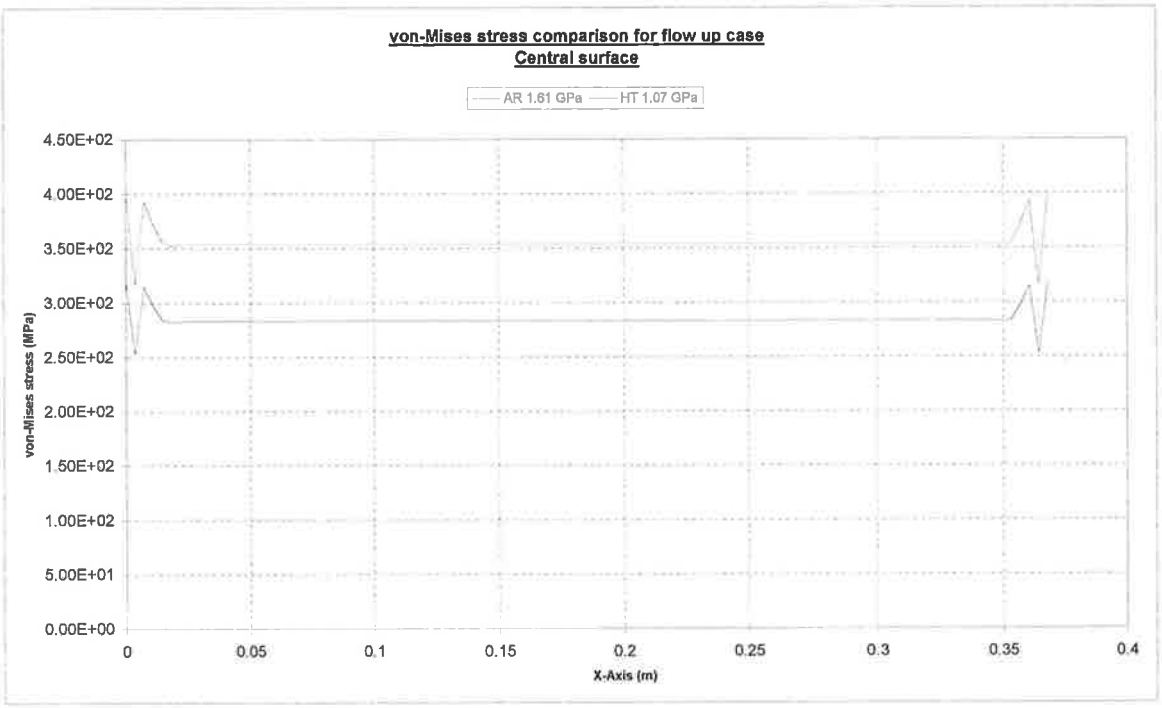

Figure 68, von-Mises stress along the axial direction in the mid-plane of the casing for +10% mass flow rate case. AR represents as received while HT corresponds to heat treatment.

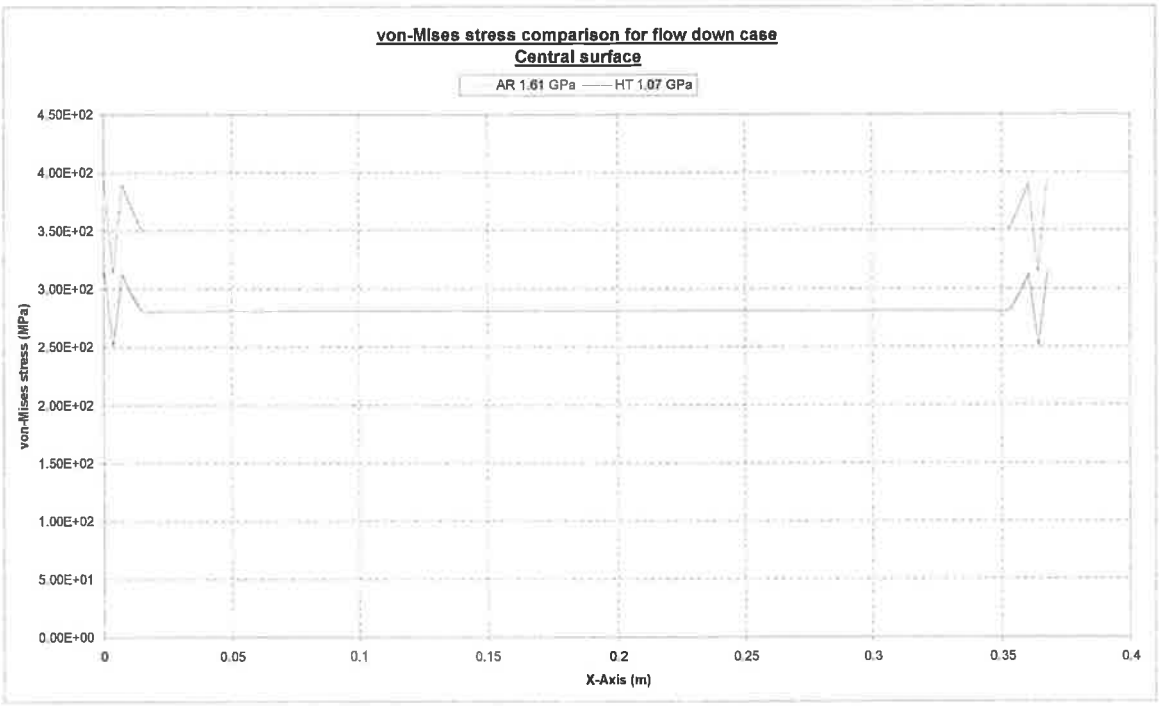

Figure 69, von-Mises stress along the axial direction in the mid-plane of the casing for -10% mass flow rate case. AR represents as received while HT corresponds to heat treatment.

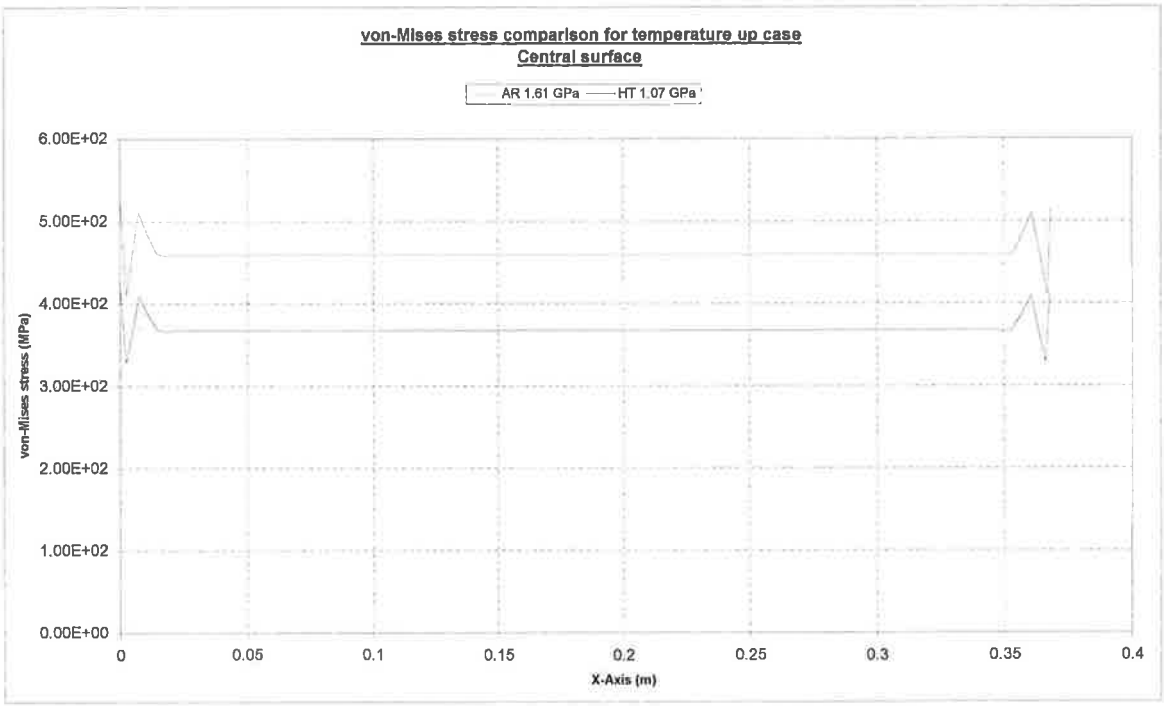

Figure 70, von-Mises stress along the axial direction in the mid-plane of the casing for +10% entry temperature case. AR represents as received while HT corresponds to heat treatment.

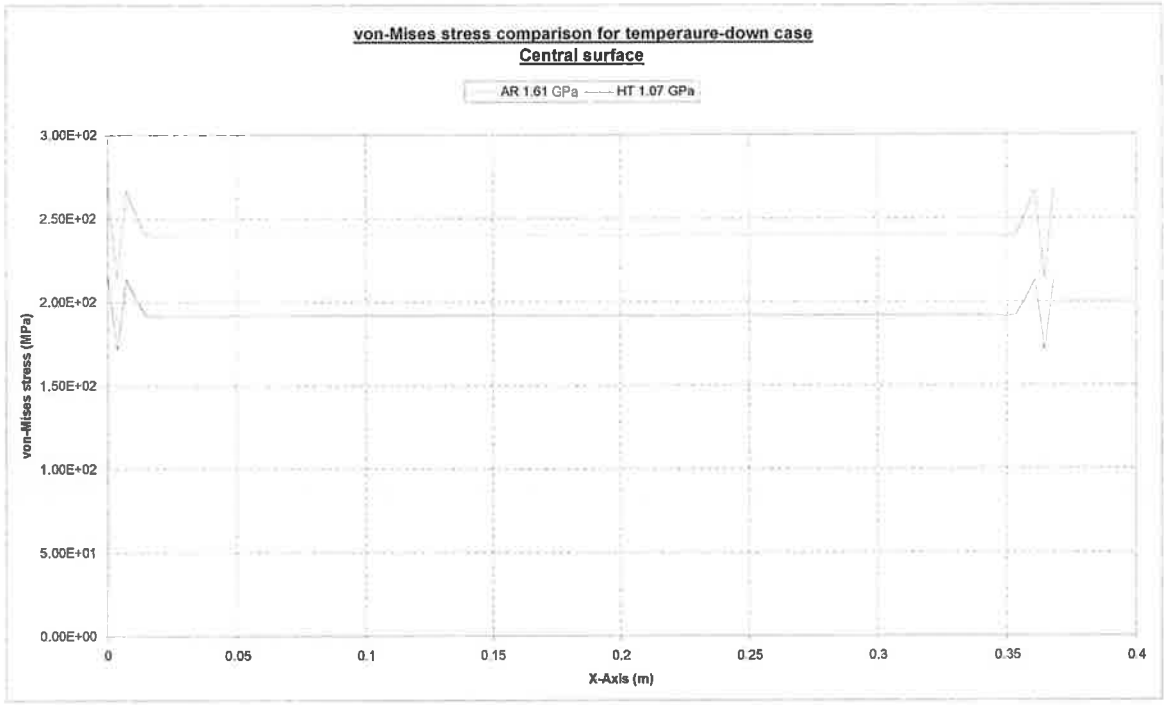

Figure 71, von-Mises stress along the axial in the mid-plane of the casing for -10% entry temperature case. AR represents as received while HT corresponds to heat treatment.

In the case of inner-plane (Figures 72-76), von-Mises stress attains high values at the ends of the transition-piece. Therefore, similar observations can be made for Figures 72-74 as those made for Figures 62-64 and 67-69. This is due to the similarities in temperature distributions. The von-Mises stress level in the axial direction of the middle section attains the same values as noted before at 350 MPa and 275 MPa for the as received and heat treated cases, respectively. However, at the fixed ends the maximum value was 530 MPa and a minimum of 370 MPa for the as received, and a maximum of 420 MPa and minimum of 220 MPa for the heat treated version.

In the cases of temperature variation at the transition-piece entry temperature (Figures 75-76) the value of the thermal stress for the case of entry temperature increase by 10% in the axial distance in the middle section, was 450 MPa and 380 MPa for the as received and the heat treated material conditions, respectively. While for the decrease of the entry temperature by 10%, the von-Mises stress value was 240 MPa and 190 MPa for the as received and heat treated material, respectively. The stress level values for the 10% increase in entry temperature case at the fixed ends were a maximum of 580 MPa and a minimum of 360 MPa for the as received and a maximum of 450 MPa and a minimum of 280 MPa for the heat treated condition. For the case of 10% decrease in the entry temperature, the maximum von-Mises stress value at the fixed was 390 MPa and the minimum was 280MPa for the as received material condition while the maximum was 280 MPa and the minimum was 150 MPa for the heat treated material condition. In this case, the magnitude of von-Mises stress is affected by the proximity to the hot gas, and hence the high temperature gradient developed inside the transition-piece.

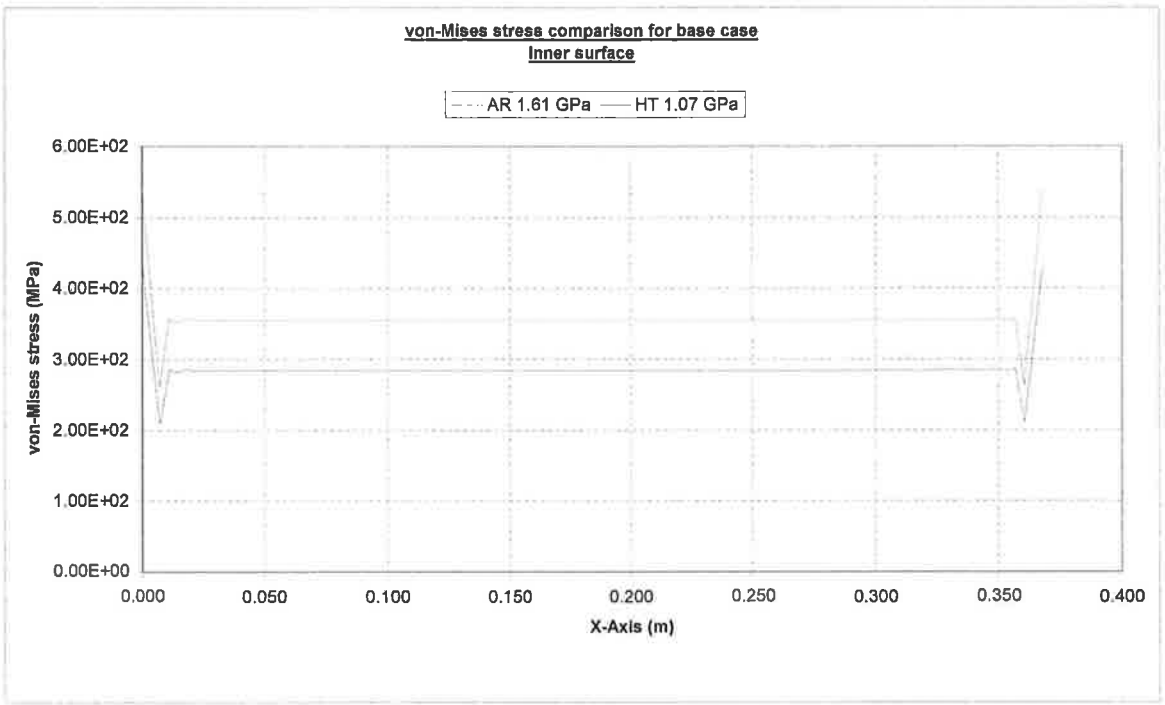

Figure 72, von-Mises stress along the axial direction in the inner wall for the base case. AR represents as received while HT corresponds to heat treatment.

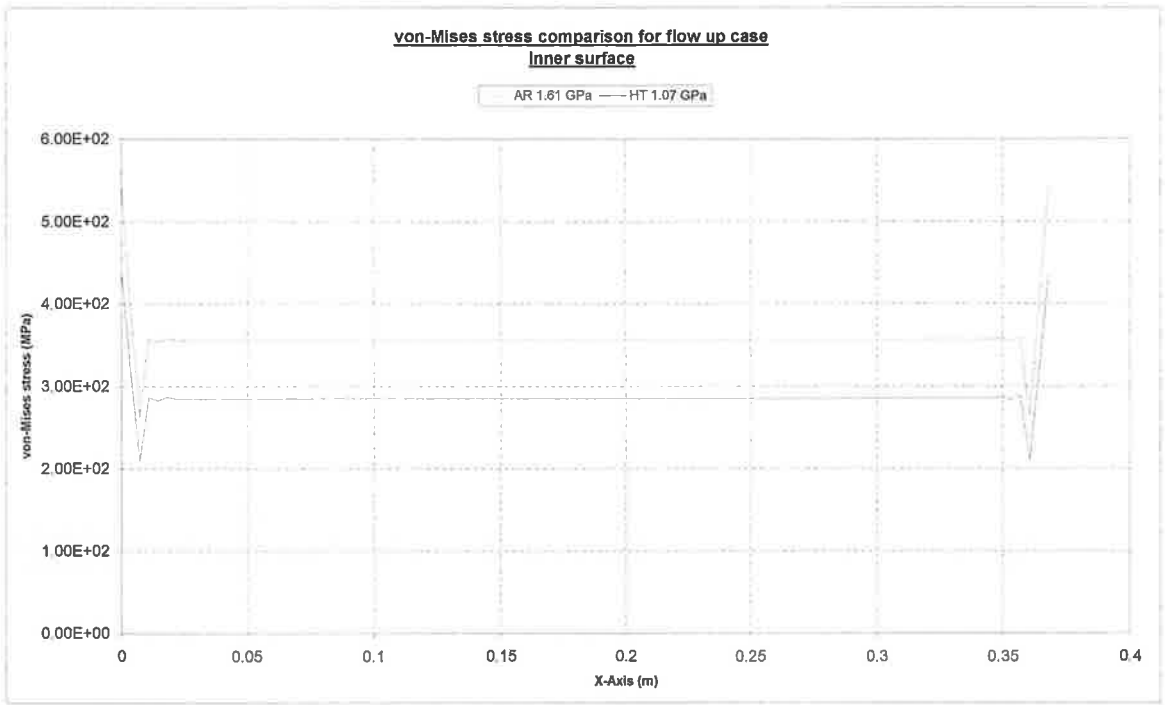

Figure 73, von-Mises stress along the axial direction in the inner wall for the +10% mass flow rate case. AR represents as received while HT corresponds to heat treatment.

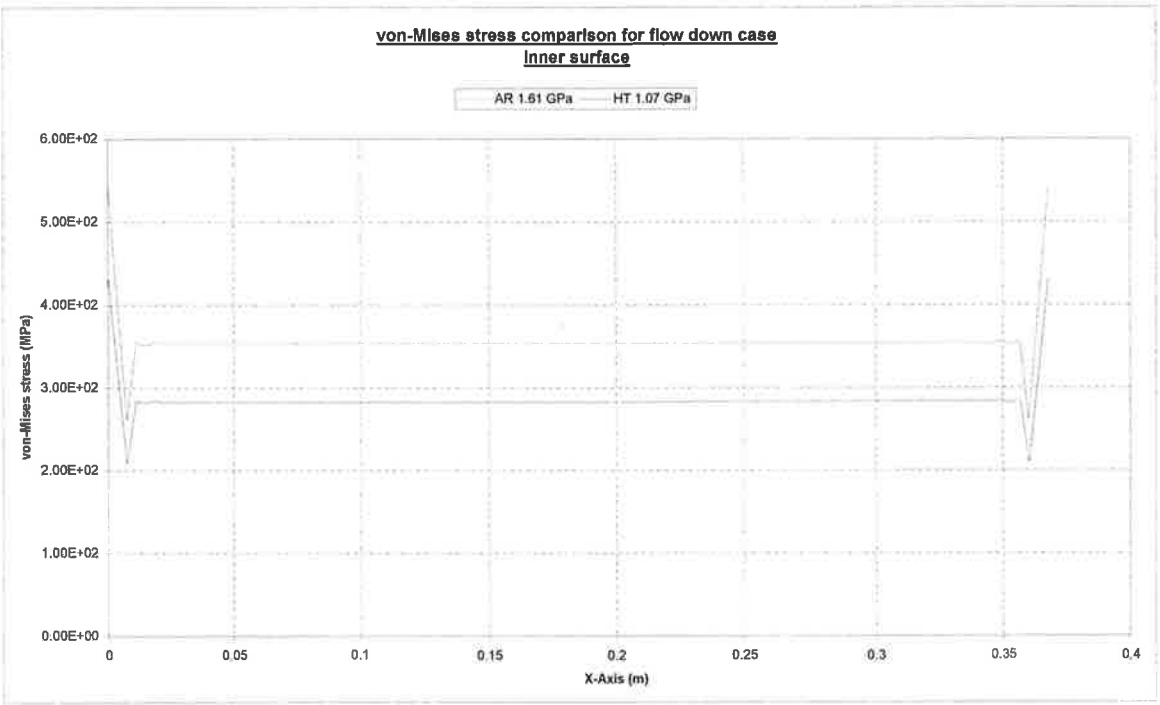

Figure 74, von-Mises stress along the axial direction in the inner wall for the -10% mass flow rate case. AR represents as received while HT corresponds to heat treatment.

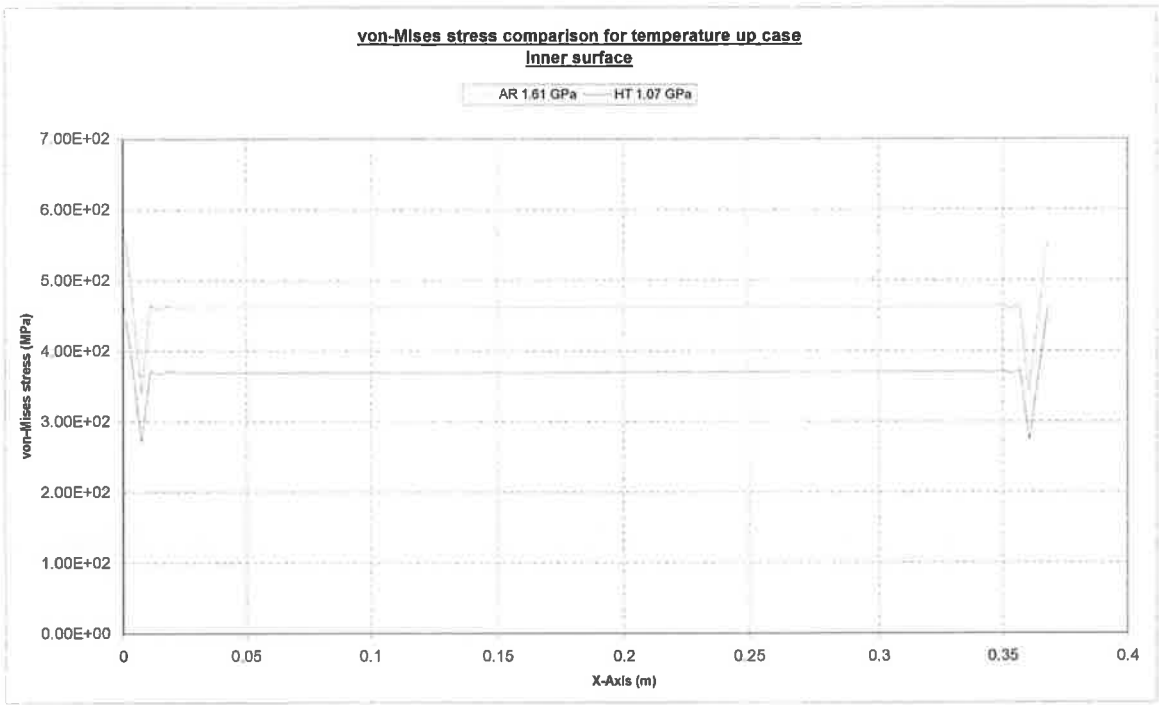

Figure 75, von-Mises stress along the axial direction in the inner wall for the +10% entry temperature case. AR represents as received while HT corresponds to heat treatment.

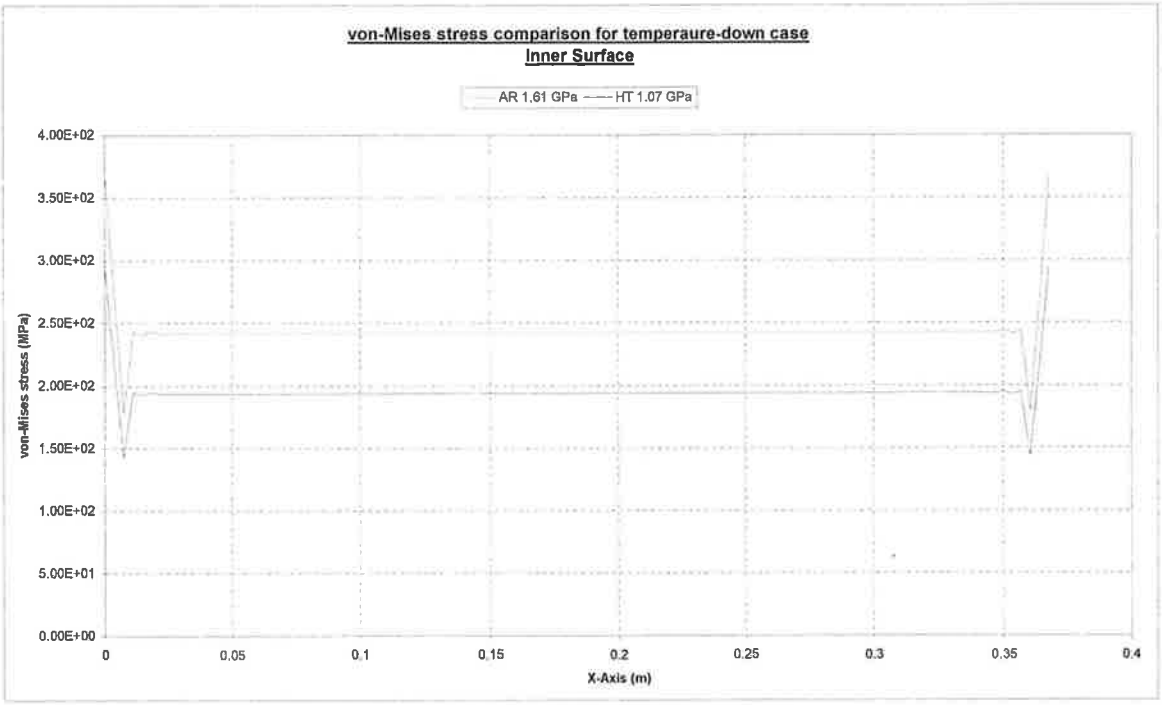

Figure 76, von-Mises stress along the axial direction in the inner wall for the -10% entry temperature case. AR represents as received while HT corresponds to heat treatment.

6

CONCLUSIONS AND RECOMMENDATIONS

6.1 CONCLUSIONS

In the present research, flow through a transition-piece of an aero-derivative gas turbine engine used in a mechanical drive application was considered, and temperature distribution in the transition-piece casing was predicted numerically. To resemble the high temperature operating environment, the transition-piece substrate material (Iron-Base A286 Superalloy) was heat treated. Tensile and three-point bending tests were carried out to determine the Modulus of Elasticity of the AR and HT material conditions. The effect of elevated temperature operation on the transition-piece was incorporated in the Modulus of Elasticity. The resultant Modulus of Elasticity for both conditions was then accommodated in the numerical simulation to predict the thermally induced stresses in the casing of the transition-piece. The microstructure of the A286 alloy before and after the heat treatment was examined by SEM, EDS, and XRD.

The conclusions resulting from the investigation are summarised as follows:

- It was found that the geometrical gradual expansion of the transition-piece resulted in flow deceleration towards the inner casing, in the entry region of the transition-piece, where the pressure decreases significantly. As the flow progresses inside the transition-piece, the convective deceleration of the flow increased the pressure towards the exit, and since the pressure increase in the downstream of the transition-piece is gradual, the flow

straightens in the axial direction without separation. Although the flow experienced acceleration in the radial and deceleration in the axial directions in the transition-piece entry region, no separation or swirling flow was observed.

- Temperature in the casing drops gradually in the radial direction towards the outer surface. However, sharp variation in the temperature was observed in the entry region. A similar situation also occurred in the exit region; in this case, flow deceleration and axial conduction heat transfer in the casing were responsible for a sharp decay in the temperature in this region.
- Variation of the entry mass flow rate by ±10% from the nominal operational value does not alter the flow structure inside the transition-piece, and only slight velocity magnitude change was noted between the ± 10% entry mass flow rate change cases. Moreover, the increase or decrease in the velocity magnitude was found to be approximately equal to the increase or decrease in the entry mass flow rate. The static pressure distribution and magnitude were found to be the same for both cases of ±10% mass flow rate variation. It was also noted that there was no change in the static pressure distribution and magnitude, when the two cases of ±10% mass flow rate variation were compared to the static pressure distribution and magnitude results obtained from simulation of the base case. There was no change in the maximum and minimum static temperature values across the transition-piece, but there was slight change in the temperature gradient between the two cases of mass flow rate variation.
- It was found that increase or decrease of the mass flow rate, by ±10% from the nominal operational value, does not change the thermally developed stress, relative to the ones developed during operation with the nominal values used in the simulation of steady state condition, (base case) explained previously. This emphasises the result that variation of the mass

flow rate within the specified operating range of the engine had no effect on the thermally developed stress in the transition-piece.

- It was found that variation of the transition-piece entry temperature by + 10% from the nominal operational value significantly alters the flow structure and velocity distribution inside the transition-piece, with the maximum velocity 20% above the nominal value. The static pressure increased along the axial direction and towards the transition-piece exit, due to the diverging configuration of the transition-piece with no development of a secondary flow or recirculation in the exit region. The static temperature values and distribution changed significantly, which was reflected in the thermal stresses developed in the transition-piece for this case. For the variation of transition-piece entry temperature by -10% from the nominal value there is no change in the velocity, pressure distribution or the static temperature distribution in the transition-piece compared to operating the engine at the base case.
- It was found that in the case entry temperature increase by 10% from the nominal operational value, the axial stress component increased at the fixed ends the same as everywhere else in the transition-piece. The increase at the fixed ends was below the yield limit. The same also can be stated for the radial stress component. For the case of entry temperature decrease by 10% from the nominal operational value, it was found that the axial stress component was significantly below the ones noted in the base case, and the same can be stated in the case of radial stress.
- In general, the axial thermal stress component developed in the metallic casing of the transition-piece was compressive, and attained almost a uniform value along the axial direction, with sharp changes at the inlet and the exit regions, due to expansion constraints in the axial direction at the fixed ends of the transition-piece casing. The radial stress component of the thermal stress was compressive at the fixed ends, and it changed to tensile next to the entry and exit of the transition-piece. The magnitude of the radial stress component was not significant, due to free expansion of the

casing in the radial direction.

- For the von-Mises stress values in the as received material condition;
    - The von-Mises stress in the outer surfaces remained below the yield limit in the middle section for all the cases investigated. At the fixed ends the von-Mises stress level did not exceed the yield limit in all cases investigated with the highest value noted was due to the increase in entry temperature.
    - In the central surfaces, the von-Mises stress stayed below the material yield limit in the middle section and the fixed ends regions for all the cases investigated.
    - In the inner surfaces, the von-Mises stress stayed below the yield limit for all the cases investigated at all locations..
- The von-Mises stress attained high values at the edges of the transition-piece, in the as received material condition case, which is attributed to the fixed ends of the transition-piece and attainment of the high temperature gradient in this region.
- The von-Mises stress in the vicinity of the fixed ends of the transition-piece attained low values, due to the radial expansion of the transition-piece. This was highly notable in the outer surface of the transition-piece which in turn caused the difficulties in aligning of the transition-piece with the free power turbine in the field.
- For the von-Mises stress values in the heat treated material condition;
    - The von-Mises stress in the outer surfaces remained below the yield limit in the middle section and the fixed ends region for all the cases investigated
    - In the central plane, the von-Mises stress also remained below the material yield limit in the middle section as well as the fixed ends regions for the all cases.

  - In the inner plane, the von-Mises stress remained below the yielding limit for all the cases in the middle section and the fixed ends regions.

- The Modulus of Elasticity of the heat treated specimen was significantly lower than that of the as received material. This is due to the grain coarsening, which in turn improves the ductility of the heat treated material.
- The von-Mises stress level for the heat treated work piece was significantly lower than that of the as received material. This is due to the low elastic modulus of the heat treated work piece and the effect of the operating at elevated temperature.
- The XRD analysis showed the depletion of γ' through dissolution at the grain boundaries and formation of η-phase (hexagonal closed- packed- hcp- Ni_3T_i phase). This is considered to be the main factor contributing to the low mechanical performance of the material after the heat treatment process.
- The plastic deformation of the transition-piece material is unlikely during the continuous operation of the engine at elevated temperature, after the initial operation of the transition-piece from new (i.e.AR condition), due to the effect of operating at elevated temperature, which will act as heat treatment process. However, repeated start up and shutdown of the engine (cyclic operation) from high temperature, might lead to formation of η-phase at the grain boundaries, which will act as a nucleation site for the crack formation. This situation results in the transition-piece (installed on engine) with short operation duration (i.e. short cyclic operation and/or higher rate of shop visits). These are the ones which should be paid more attention during the inspections. Moreover, the transition-piece fixed ends are the areas which are most likely to deform and for the cracks to occur at, that means more rigorous inspections are needed on those areas.

6.2 RECOMMENDATIONS FOR FUTURE WORK

The results documented in the present study are significant; however the future work in relation to the present study can be listed as follows:

- The transient heating situation covering the flow and the temperature fields in the transition-piece can be examined. The stress field due to transient heating of the casing can be formulated and predicted.

- Although the A286 Iron-Base Superalloy is widely used in gas turbine engines parts and specifically for transition-pieces for the engines produced before the end of the 1980's, the possibility of the usage of other alloys resulting in improved heat transfer and smaller temperature gradients should be investigated. This can provide the basis for further insight into the life assessment of such alloys in the high temperature flow environment. In addition, cost effective operation, maintenance and overhaul of the parts made from these different alloys can be identified.

- Conduct a CFD detailed study considering the different turbulence models in steady state conditions and transient condition to determine the flow and pressure fields inside the transition-piece and the temperature distribution in the casing outer wall.

- The mechanical properties of the A286 alloy and fatigue conditions can be examined in relation to the transient simulations. Once the flow and temperature fields become transient, thermally induced dynamic effects become more important. This requires the extension of the present work to include the transient response of the transition-piece, such as the fatigue response.

DECLARATION

I herby certify that this material, which I now submit for assessment on the programme of study leading to the award of Doctor of Philosophy, is entirely my own work and has not been taken from the work of others save and to the extent that such work has been cited and acknowledged within the text of my work.

Signed:  I.D. Number: 53122259

Date:

PUBLICATIONS ARISING FROM THIS WORK

Journals

1. **Mustafa, Alaaeldin H**, M.S.J. Hashmi, B.S Yilbas, and M. Sunar "Thermal Stress Analysis in Annular Duct Resembling Gas Turbine Transition-Piece", Journal of Material Processing Technology, (2005).

Conference Papers

2. **Mustafa, Alaaeldin H**, M.S.J. Hashmi, B.S Yilbas, and M. Sunar ., "Thermal Stress Analysis in Annular Duct Resembling Gas Turbine Transition-Piece: Effect of mass flow rate variation" , Proceeding of AMPT 2006, Jul 30-Aug 3, 2006, Las Vegas, USA, (2006).

3. **Mustafa, Alaaeldin H**, M.S.J. Hashmi, B.S Yilbas, and M. Sunar ., "Thermal Stress Analysis in Annular Duct Resembling Gas Turbine Transition-Piece: Effect of entry temperature variation" , Proceeding of MEMEC 2007, November 4-7, 2007, Manama, Bahrain, (2007), in print.

4. **Mustafa, Alaaeldin H**, M.S.J. Hashmi, B.S Yilbas, and M. Sunar, "Investigation into thermal stresses in gas turbine transition-piece : Influence of material properties on stress levels", Proceeding of AMPT 2007, Oct 30-Aug 3, 2007, Soul, South Korea, (2007), in print.

REFERENCES

1 Je-Chin Han, Sandip Dutta and Srinath Ekkad. Gas turbine Heat Transfer and Cooling Technology. Published 2000. Taylor& Francis, 29 West 35th Street, NY, NY10001, pp. 4-6.

2 BOHLER EDELSAHL, Inspection Certificate B.

3 GE Energy Products- Europe. Abqaiq Operation and Maintenance Manual. Rev. 0, 22.06.01. Chapter 1, pp 26.

4 Peter Moonen, Bert Blocken, Staf Roels, and Jan Carmeliet. Numerical modeling of the flow conditions in a closed-circuit low-speed wind tunnel. Journal of Wind Engineering and Industrial Aerodynamics 94 (2006), pp. 699-723.

5 T Engin. Study of tip clearance effects in centrifugal fans with unshrouded impellers using computational fluid dynamics. Proceedings of the Institution of Mechanical Engineers, Journal of Power and Energy, vol. 220, Part A (2006), pp. 599-610.

6 Huang, Z. Olson, J.A. Kerekes, R.J. Source. Numerical simulation of the flow round rows of cylinders. Computer & Fluids 35 (2006) pp. 485-491.

7 Leduc Sylvain, Fredriksson Christian, and Hermansson Roger. Particle-tracking option in Fluent validated by simulation of a low-pressure impactor. Advanced Power Technology. Vol. 17, No 1 (2006), pp. 99-111.

8 Frederic Depypere,Jan G. Pieters, and Koen Dawettinck. CFD analysis of air distribution in fluidized bed equipment. Powder Technology 145 (2004) pp.

176-189.

9 Hyung Hee Cho (Dept. of Mech. Eng., Yonsei Univ., Seoul, South Korea); Sang Dong Hwang; Jang, I.H. Source. Experimental study on flow and local heat/mass transfer characteristics inside corrugated duct. International journal of Heat and Fluid Flow 27 (2006) pp. 21-32.

10 S.Ergin and M.Ota. A study of the effect of duct width on fully developed turbulent flow characteristics in a corrugated duct. Heat Transfer Engineering 25, 2 (2005) pp. 54-62.

11 J.Perez-Garcia, E. Sanmiguel-Rojas, J. Hernández-Grau, and A. Viedma. Numerical and experimental investigations on internal compressible flow at T-type junctions. Experimental Thermal and Fluid Science (2006).

12 Murthy Lakshmiraju, Jie Cui. Numerical investigation of pressure loss reduction. Applied Mathematical Modeling (2006). Doi:10.1016/j.apm.2006.06.016.

13 Eric M. Moore, Robert L. Shambaugh, and Dimitrios V. Papavassiliou. Analysis of isothermal annular jets: Comparison of computational fluid dynamics and experimental data. Journal of Applied Polymer Science, Vol. 94 (2004) pp. 909-922.

14 Yong Wang, Guang Yuan, Yong-Kyu Yoon, Mark G. Allen and Sue Ann Bidstrup. Large eddy simulation (LES) for synthetic jet thermal management. International journal of heat and mass transfer 49 (2000) pp. 2173-2179.

15 S.Hogg and M.A.Leschziner. Computation of highly swirling confined flow with a Reynolds stress turbulence model. AIAA Journal, Vol.27,No.1, (1989), pp. 57-63.

16 J.S.Rao and M. Saravanakumar. Numerical simulation of seal flow and determination of stiffness and damping coefficients. 7th IFToMM Conference

on Rotor Dynamics. Vienna, Austria, 25-28, (Sept. 2006).

17 Bert Blocken, Ted Stathopoulos, and Jan Carmeliet, CFD simulation of the atmospheric boundary layer: wall function problems. Atmospheric Environment 41 (2007), pp. 238-252.

18 Juan Abanto, Marcelo Reggio, and Simon Painchaud-Ouellet. On the design of RTO unit using CFD. Applied Thermal Engineering 26 (2006) pp. 2327-2335.

19 Calcagni, B. (Dipt. di Energetica, Univ. Politecnica delle Marche, Ancona, Italy); Marsili, F.; Paroncini, M. Natural convection heat transfer in square enclosures heated from below. Applied Thermal Engineering 25 (2005) pp. 2522-2531.

20 Kilic M. Determination of heat transfer rate and Nusselt number on the thermal-entry region in ducts. International Comm. Heat and Mass Transfer, Vol. 31, No 1 (2004), pp. 181-190.

21 Huseyin Yapici and Gamze Basturk, Numerical solutions of conjugate heat transfer and thermally induced stress distribution in a heated and rotating hollow disk. Energy Conversion and Management (2005) pp. 61-84.

22 Andrej Horvat and Borut Mavko. Calculation of conjugate heat transfer problem with volumetric heat generation using the Galerkin method. Applied Mathematical Modeling 29 (2005) pp. 477-495

23 E Y Ng, P W Johnson, S Watkins. An analytical study on heat transfer performance of radiators with non-uniform airflow distribution. Proceedings of the Institution of Mechanical Engineers, Journal of Automobile Engineering, vol 219, Part D (2005), pp. 1451-1467.

24 S.W.Ahn .The effects of roughness types on friction factors and heat transfer in roughened rectangular duct. Int. Comm. Heat transfer Vol. 28 (2001). pp.

933-942.

25 Owen, I. and Barrow, H. A Simple Method for Predicating Turbulent Annular Flow & Heat Transfer. Heat & Technology, Vol. 10. No 1-2 (1992).

26 Seung Dong Lee and Kune Yull Suh. Natural convection heat transfer in two-dimensional semicircular slice pool. Journal of Nuclear Science and Technology, Vol 40, No 10 (2003) pp. 775-782.

27 Povilas Poskas and Robbertas Poskas. Turbulent opposing mixed convection heat transfer in a vertical flat channel with one-side heating. Heat Transfer Engineering 25, 2 (2004) pp. 17-23.

28 Robert E. Spall, Adam Richards, and Donald M. Mc Eligot. An assessment of κ-ω and $v^2 - f$ turbulence models for strongly heated internal gas flows. Numerical Heat transfer. Part A 46 (2004) pp. 831-849.

29 Jerome Hebrard, Olivier Métais, and Martin Salinas-Vasquez, Large-eddy simulation of turbulent duct flow: heating and curvature effects. International Journal of Heat and Fluid Flow 25 (2004), pp. 569-580.

30 Liu, Zhi-Gang (Energy Research Institute, Shandong Academy of Sciences); Zhao, Yao-Hua Experimental studies of heat transfer in a tube bundle model Journal of Beijing University of Technology, v 32, n 12, December, 2006, p 1125-1129.

31 Witry, A.; Al-Hajeri, M.H.; Bondok, Ali A. Thermal performance of automotive aluminum plate radiator. Applied Thermal Engineering 25 (2005), pp. 1207-1218.

32 Pelletier, O. Stromer, F. Carlson, A., CFD simulation on heat transfer in compact brazed plate heat exchangers. ASHRAE Transactions (2000), pp. 846-854.

33 Cole, K.D. Conjugate heat transfer from a small heated strip. Int. J. Heat and

Mass Transfer Vol 40, No 11 (1997) pp. 2709-2719.

34 Yapici, Huseyin (Muhendislik Fakultesi, Erciyes Universitesi); Basturk, Gamze; Albayrak, Bilge. Numerical study on conjugate heat transfer in laminar fully developed flow with temperature dependent thermal properties through an externally heated SiC/SiC composite pipe and thermally induced stress. Energy conservation and management 46 (2005), pp. 633-654.

35 Ya-Wei Lee (Dept. of Mech. Eng., Nat. Taiwan Univ., Taipei, Taiwan); Chih-Wei Chang; Jr-Ming Miao; Ping-Hei Chen., Conjugate heat transfer of a disk-shaped miniature heat pipe. Numerical Heat Transfer, Part A, 49 (2006), pp. 25-45.

36 Luna, N. (Instituto Mexicano del Petroleo, Mexico City, Mexico); Mendez, F.; Trevino, C. Conjugate heat transfer in circular ducts with a power-law laminar convection fluid flow. International Journal of Heat & Mass Transfer 45 (2002), pp. 655-666.

37 Bilir, Sefik. Transient conjugated heat transfer in pipes involving two-dimensional wall and axial fluid conduction. Int. J. Heat and Mass Transfer 45 (2002) pp. 1781-1788.

38 Gh. Juncu. Unsteady conjugate heat/mass transfer from a circular cylinder in laminar cross flow at low Reynolds numbers. International Journal of Heat and Mass Transfer 47 (2004) pp. 2469-2480.

39 J.S.Rao. and M.Saravanakumar. Heat transfer Studies in Cryogenic Systems with liquid oxygen at -150° Celsius. 7th annual GE gas turbine Users Conference 12th-13th September 2006, Dubai, UAE.

40 Mazur, Z. (Inst. de Investigaciones Electr.as, Cuernavaca Morelos, Mexico); Hernandez-Rossette, A.; Garcia-Illescas, R.; Luna-Ramirez, A ., Analysis of conjugate heat transfer of a gas turbine first stage nozzle. Applied Thermal

Engineering 26 (2006), pp. 1796-1806.

41 J.S.Rao and M. Saravanakumar. Numerical prediction of cavitations flow on a marine propeller using a CFD code. Int. Conference on Computational Fluid Dynamics, Acoustics, Heat Transfer and Electromagnetic. CFEMATCON-06, July 24-25 (2006) Andhra University, Visakhapatnam-530003, India.

42 Peng, X.F. (Dept. of Thermal Eng., Tsinghua Univ., Beijing, China); Li, L.; Liu, T., Combustion and cooling performance in an aero-engine annular combustor. Applied Thermal Engineering 26 (2006), pp. 1771-1779.

43 Dixon, J.A. (Dept. of Thermal Syst., Airlines Eng., Derby, UK); Verdicchio, J.A.; Benito, D.; Karl, A.; Tham, K.M., Recent developments in gas turbine component temperature prediction methods using computational fluid dynamics and optimization tools, in conjunction with more conventional finite element analysis techniques. Proceedings of the Institution of Mechanical Engineers, Power and Energy, vol 218, Part A (2004), pp. 241-255.

44 Rashid A. Ahmad. Convective heat transfer in the reusable solid rocket motor of the space transportation system. Heat Transfer Engineering, vol 26-10 (2006), pp 30-45.

45 Vassiliev, V. (ALSTOM (Switzerland) Ltd.); Irmisch, S.; Claridge, M.; Richardson, D.P., Experimental and numerical investigation of the impact of swirl on the performance of industrial gas turbine exhaust diffusers. Proceedings of ASME Turbo Expo 2003 Power for Land, Sea, and Air. June 16-19, 2003, Atlanta, Georgia, USA.

46 Kumar, D.S, Numerical Study of Swirling Flow through Annular Diffusers. I Mech. E. (Institute of Mechanical Engineers) Conference Publications (1984) pp.33-39.

47 Jian Zhang (Dept. of Eng. Mech., Tsinghua Univ., Beijing, China); Linjiang Dong; Lixing Zhou; Nieh, S., Simulation of Swirling Turbulent Flows and Heat Transfer in an Annular Duct. Numerical Heat Transfer, part A 44 (2003) pp. 591-609.

48 Nouar, C. Numerical Solutions for Laminar Mixed Convection in a Horizontal Annular Duct. Temperature – Dependent Viscosity Effect. Int. Journal for Numerical Methods in Fluids (1999) pp. 849-864.

49 Huseyin Yapici and Bilge Albayrak, Numerical Solutions of Transient Conjugate Heat Transfer and Thermally Stresses in Circular Pipe Externally Heated with Non-uniform Heat Flux. Energy Conversion and Management, (2004) pp. 927-937.

50 Cha'o-Kuang Chen (Dept. of Mech. Eng., Nat. Cheng Kung Univ., Tainan, Taiwan); Li-Wen Wu; Yue-Tzu Yang., Estimation of Unknown Outer –Wall Heat Flux in Turbulent Circular Pipe Flow with Conduction in The Pipe Wall. Int. Journal of Heat and Mass Transfer 48 (2005) pp. 3971-39811.

51 De Vine III, J.C. and Peterson, P.F. Conjugate Heat Transfer in Converging-Diverging Nozzle Flow. HTD-Vol-245/NE-Vol-11, American Society of Mechanical Engineers pp. (1993).

52 Edimilson J. Brag and Marcelo J. S. deLemos. Numerical Simulation of Turbulent Flow in Small-Angle Diffusers and Contractions using a New Wall Treatment and Linear High Reynolds κ-ε Model. Numerical Heat Transfer. Part A., 45(2004) pp. 911-933.

53 Shuja.Z.S. and Habib. A.M. Fluid Flow and Heat Transfer Characteristics in Axisymmetric Annular Diffusers. Computers & Fluids Vol. 25. No. 2 (1996) pp. 133-150.

54 Guardo, A. (Chemical Engineering Department, ETS d'Enginyeria Indust. Barcelona, Univ. Politecnica de Catalunya); Coussirat, M.; Larrayoz, M.A.;

Recasens, F.; Egusquiza, E. Influence of the turbulence model in CFD modeling of wall-to-fluid heat transfer in packed beds. Chemical Engineering Science 60 (2005), pp. 1733-1742.

55 Ishikawa, K. and Nakamura, I. Experimental Study on the Performance of Mixed-Flow-Type Conical Walled Annular Diffusers. American Society of Mechanical Engineers (1988) pp. 73—80.

56 De Cicco, H. (Dept. Mater., Comision Nacional de Energia Atomica, Buenos Aires, Argentina); Luppo, M.I.; Raffaeli, H.; Di Gaetano, J.; Gribaudo, L.M.; Ovejero-Garcia, J., Creep behavior of an A286 type stainless steel. Material Characterization 55, (2005), pp. 97-105.

57 Kohno, Masayoshi and Honjo, Takemitsu. Effect of Hot Working Conditions on the Grain Size of A286 Alloy. Transactions ISIJ. Vol 23. 105th ISIJ meeting. Lecture No. S611. 1983.

58 Bengtesson, Bengt and Korhonen, Seppo, Behavior of A286 in BWR Environment: Service Experience and Test Results. Proceedings of Int. Symposium on Environmental Degradation of Materials in Nuclear power Systems- Water Reactors. Myrtle Beach, South Carolina, August 22-25, 1983.

59 Wilson, I. L. W, and Mager, T. R. Stress Corrosion of Age Hardenable Ni-Fe-CR Alloys. Technical Symposia - Corrosion 85. Boston, MA, USA. NACE, 1985, p 96. 1-96. 15.

60 Kohno, Masayoshi (Kobe Steel, Jpn); Honjo, Takemitsu; Kinoshita, Shushi; Suzuki, Akira., Properties of large A286 Alloy rotor forging. Kobelco Technology Review, No 2. August 1987.

61 Prager, M. and Leyda, W.E. The effects of heat treatment and composition on A286 creep rupture behavior. American Society of Mechanical Engineers,

Materials Properties Council – MPC, V28 (1988), pp. 83-99.

62 De Cicco, H. (Comn. Nac. de Ener. Atomica, Departamento Materiales); Luppo, M.I.; Gribaudo, L.M.; Ovejero-Garcia, J., Microstructure development and creep behavior in A286 superalloy. Material Characterization 52, (2004), pp. 85-92.

63 Ducki, K.J. (Dept. of Mater. Sci., Silesian Univ. of Technol., Katowice, Poland); Rodak, K.; Hetmanczyk, M.; Kuc, D., Subgrain and dislocation structure changes in hot-deformed high-temperature Fe-Ni austenitic alloy. Materials Chemistry and Physics 81, (2003), pp. 493-495.

64 Ducki, K.J. (Materials Science Department, Silesian University of Technology); Hetmanczyk, M.; Kuc, D., Analysis of the precipitation process of the intermetallic phases in a high-temperature Fe-Ni austenitic alloy. Materials Chemistry and Physics 81, (2003), pp. 490-492.

65 Hicks.P.D and Altstetter. C. J. Internal Hydrogen effects on tensile properties of iron and nickel base superalloys. Metallurgical Transactions A. Vol 21A. February 1990. 365-372.

66 M. A. Daeubler, A. W. Thompson, and I. M. Bernstein., Crack initiation and near-threshold surface fatigue crack propagation behavior of the iron-base superalloy A-286. Metallurgical transaction A, Vol 19A (1988), pp. 301-308.

67 Huang, B.X. (Sch. of Mater. Sci. & Eng., Shanghai Jiao Tong Univ., China); Wang, X.D.; Rong, Y.H.; Wang, L.; Jin, L., Mechanical behavior and martensitic transformation of a Fe-Mn-Si-Al-Nb Alloy. Materials Science and Engineering A (2006).

68 Xie, Xishan (High Temp. Mat. Res. Lab., Univ. of Sci. and Technol. Beijing); Mao, Zhengdong; Dong, Jianxin; Hu, Yaohe., Investigation on high temperature strengthening and toughening of iron-base superalloy. Journal of University of Science and Technology Beijing. Vol. 10, No 1, (2003), pp.

44-48.

69 Rho, B.S. (Korea Adv. Inst. of Sci. & Technol., Taejon, South Korea); Nam, S.W.; Xie, X., The effect of test Temperature on the Intergranular Cracking of Nb-A286 alloy in Low Cycle Fatigue. Journal of Materials Science 37, (2002), pp . 203-209.

70 B.S.Rho and S.W.Nam.,The effect of applied strain range on the fatigue cracking in Nb-A286 iron-base superalloy. Materials Letters 48 (2001), pp. 49-55.

71 Rho, Byung Sup (Korea Advanced Inst of Science and Technology); Hong, Hyun Uk; Nam, Soo Woo., Analysis of the intergranular cavitations of Nb-A286 alloy in high temperature low cycle fatigue using EBSD technique. Scripta Mater. 43, (2000), pp. 167-173.

72 Strum, M. J. (Lawrence Berkeley Lab, Berkeley, Calif, USA); Summers, L. T.; Morris, J. W. Jr., The Aging Response of a Welded Iron-Based Superalloy. Welding Research supplement September (1983), pp. 235-242.

73 Kim, Han Soo (Metallurgical Processing Group, Steel Research Center, National Institute for Materials Science); Kobayashi, Y.; Tsukamoto, S.; Nagai, K., Effect of cooling rate on microstructure evolution of rapidly cooled high-impurity steels. Materials Science and Engineering A 403, (2005), pp. 311-317.

74 Ferguson, B.L. (Deformation Control Technol. Inc., Cleveland, OH, USA); Li, Z.; Freborg, A.M., Modeling of heat treatment of steel parts. Computational Materials Science 34, (2005), pp. 274-281.

75 De Cock, T. (Solid-Solid Phase Transformation Group (Materalia), Department of Physical Metallurgy, Centro Nacional de Investigaciones Metalurgicas (CENIM)); Ferrer, J.P.; Capdevila, C.; Caballero, F.G.; Lopez, V.; Garcia de Andres, C., Austenite retention in low Al/Si multiphase steels.

Scripta Materialia 55, (2006), pp. 441-443.

76 Srivastava, Ashok Kumar (Department of Metallurgical and Materials Engineering, Indian Institute of Technology); Jha, G.; Gope, N.; Singh, S.B., Effect of heat treatment on microstructure and mechanical properties of cold rolled C-Mn-Al-Si TRIP-aided steel. Materials Characterization. (2006).

77 A.R.Mirak and M.Nili-Ahmadabad. Effect of modified heat treatments on the microstructure and mechanical properties of low alloy high strength steel. Materials Science and Technology Vol.20 (2004), pp. 897-902.

78 Zhang, Z. (Electromech. & Mater. Eng. Coll., Dalian Maritime Univ., China); Delagnes, D.; Bernhart, G., Ageing effect on cyclic plasticity of tempered martensitic steel. International Journal of fatigue Vol.29 (2007), pp. 336-346.

79 Filippov, M.A. (Ural State Eng. Univ., Ekaterinburg, Russia); Belozerova, T.A.; Blinov, V.M.; Kostina, M.A.; Val'kov, E.V., Effect of heat treatment on the wear resistance of high-carbon and high-nitrogen steels subjected to abrasive wear. Metal Science and Heat Treatment. Vol.48 (2006), pp. 170-174.

80 Ros-Yanez, Tanya (Facultad de Ingenieria Mecanica y Electrica, Universidad Autonoma de Nuevo Leon); Ruiz, Daniel; Barros, Jose; Houbaert, Yvan; Colas, Rafael., Study of deformation and aging behavior of iron-silicon alloys. Materials Science and Engineering A 447 (2007), pp. 27-34.

81 Srivastava, Ashok Kumar (Department of Metallurgical and Materials Engineering, Indian Institute of Technology); Bhattacharjee, D.; Jha, G.; Gope, N.; Singh, S.B., Microstructural and mechanical characterization of C-Mn-Al-Si cold-rolled TRIP-aided steel. Material Science and Engineering A445-446 (2007), pp. 549-557.

82 K.Komori. Ductile fracture criteria for simulating shear by node separation method. Theoretical and applied Fracture Mechanics 43 (2005),pp. 101-114.

83 Li, H. (Sch. of Mech. & Production Eng., Nanyang Technol. Univ., Singapore); Khor, K.A.; Cheang, P., Young's modulus and fracture toughness determination of high velocity oxy-fuel sprayed bioceramic coatings. Surface and Coatings Technology 155, (2002), pp. 21-32.

84 N Fawcett. A novel method for the measurement of young's modulus for thick- film resistor material by flexural testing of coated beams. Meas.Sci.Technol.9, (1998), pp. 2023-2026.

85 Stallybrass, C. (Max-Planck-Inst. fur Eisenforschung GmbH., Dusseldorf, Germany); Schneider, A.; Sauthoff, G., The strengthening effect of (Ni, Fe) Al precipitates on the mechanical properties at high temperature of ferritic Fe-Al-Ni-Cr alloys. Intermetallic 13(2005), pp.1263-1268.

86 Al-Anazi, D. (KFUPM); Hashmi, M.S.J.; Yilbas, B.S., Three-point bend testing of HOVF AMDRY 9954 coating on Ti-6A1-4V alloy. Journal of Material processing technology 174 (2006), pp. 204-210.

87 Hong, Seong-Gu (Department of Mechanical Engineering, Korea Adv. Inst. of Sci./Technology); Yoon, Samson; Lee, Soon-Bok., The effect of temperature on low-cycle fatigue behavior of prior cold worked 316L stainless steel. International Journal of Fatigue 25, (2003), pp. 1293-1300.

88 A.F.M. Arief and B.S.Yilbas. Three-point bending testing of HVOF Inconel 625 coating: FEM simulation and experimental investigation. Surface & Coating Technology 201 (2006), pp. 1873-1879.

89 Yilbas, B.S., Arif, A.F.M., and Gondal, M.A., "HVOF Coating and Laser Treatment: Three-Point Bending Tests", Journal of Materials Processing Technology, (2005), Vol. 164-165,pp. 954-957.

90 Hornhede A. Nylund A., "Adhesion Testing of Thermally Sprayed and Laser Deposited Coatings", Surface and Coating Technology, (2003), Vol. 184, pp. 208-218.

91 Xiping Guo and Kiyoshi Kusabiraki. Aging a Fe-Ni-Co-Nb-Ti-Si superalloy under tensile stress. Z.Matallkd 91, (2000), pp. 601-606.

92 Alzaharnah, I.T. (Mechanical Engineering Department, King Fahad Univ. of Petro./Minerals); Hashmi, M.S.; Yilbas, B., Thermal stresses in thick-walled pipes subjected to fully developed laminar flow. Journal of materials processing technology, 118, (2001), pp. 50-57.

93 Grzegorz Grabowski and Zbigniew Pedzich. Residual stresses in particulate composites with alumina and zirconia matrices. Journal of the European Ceramic Society 27, (2007), pp. 1287-1292.

94 Sanchez Sarmiento, G. (Universidad de Buenos Aires, Facultad de Ingenieria); Castro, M.; Totten, G.E.; Harvis, L.; Webster, G.; Cabre, M.F., Modeling residual stresses in spring steel quenching. Proceedings of the 21st conference, Nov 5-8 2001, Indianapolis, IN, USA. Pp. 191-200.

95 Brown, T.B. (Mitsui Babcock Energy Ltd., Renfrew, UK); Dauda, T.A.; Truman, C.E.; Smith, D.J.; Memhard, D.; Pfeiffer, W., Predications and measurements of residual stress in repair welds in plates. International Journal of pressure vessels and piping 83, (2006), pp. 809-818.

96 Huseyin Yapici and Gamze Basturk. Reduction of thermally induced stress in a solid disk heated with radially periodic expanding and contracting ring heat flux. Journal of Materials Processing Technology 180, (2006), pp. 279-290.

97 Al-Zaharnah, I.T. (Dept. of Mech. Eng., King Fahd Univ. of Pet. & Miner., Dhahran, Saudi Arabia); Yilbas, B.S.; Hashmi, M.S.J., Conjugate Heat Transfer in Fully Developed Laminar Pipe Flow and Thermally Induced

Stresses. Computer Methods Appl. Mech. Engineering (2000), pp. 1091-1104.

98 Ashraf, Mahmud (Department of Civil Engineering, Bangladesh University of Engineering and Technology); Gardner, Leroy; Nethercot, David A., Finite element modelling of structural stainless steel cross-sections. Thin-Walled Structures (2006), doi: 10.1016/j.tws.2006.10.010.

99 Liu, M.-S. (Zhengzhou Univ of Technology); Dong, Q.-W.; Wang, D.-B.; Ling, X., Numerical Simulation of Thermal Stress in Tube-Sheet of Heat Transfer equipment. International Journal of Pressure Vessels and Piping 76 (1999) pp. 671-675.

100 Pavier, M.J. (Dept. of Mech. Eng., Univ. of Bristol, Bristol, UK); Bateman, M.G.; Miller, O.H.; Palmer, T.J.; Breen, C.E.P.; Kingston, E.J.; Smith, D.J., Measurement of residual stress in thick section composite laminates using the deep-hole method. International Journal of Mechanical Sciences 47, (2005), pp. 1718-1739.

101 Ishihara, Sotomi (Department of Mechanical Engineering, Toyama University); Goshima, T.; Iwawaki, S.; Shimizu, M.; Kamiya, S., Evaluation of thermal stresses induced in anisotropic material during thermal shock. Journal of thermal stresses, 25 (2002), pp. 647-661.

102 Thomas, A. (SPG, Component Test Lab., Dresden, Germany); Pathiraj, B.; Veron, P., Feature tests on welded components at higher temperatures-Material performance and residual stress evaluation. Engineering Fracture Mechanics, 74 (2007), pp. 969-979.

103 Litos, P. (Dept. of Thermomechanics of Technol. Processes, West Bohemia Univ., Czech Republic); Svantner, M.; Honner, M., Simulation of strain gauge thermal effects during residual stress hole drilling measurements. Journal of strain analysis for engineering design, Vol. 40,7 (2005), pp. 611-

619.

104 D A Golański and J Grześ. The numerical analysis of residual stresses in surface layers deposited by brush-plating method. Journal of Engineering Manufacture Vol.220,part B (2006),pp.429-437.

105 F. De Paolis, R. Capriotti, M. Colavita, P. Silvestri., Hydrogen embrittlement detection on high-strength steel by means of XRD residual stress determination technique. 15th World Conference on Non-Destructive Testing, 15th- 21th October 2000, Rome, Italy.

106 Golovchan VT. On the thermal residual micro stresses in WC-Co hard metals. International Journal Refract Metals (2006), doi:10.1016/j.ijrmhm.2006.08.002.

107 H W Ng and C K., Remaining life of a vessel containing an internal corner crack under repeated thermal shock. Journal of Process Mechanical Engineering 211 Part E, (1997), pp. 215-219.

108 A.P.Nichipuruk, E.S.Gorkunovon. Evaluation of residual stresses in ferromagnetic steels by means of magnetic and magnetoelastic procedures. 15th World Conference on Non-Destructive Testing, 15th-21th October 2000, Rome, Italy.

109 A.M. Hodgea, , , R.J. Foremanb and G.F. Gallegosb., Residual stress analysis in thick Uranium films. Journal of Nuclear Materials. UCRL-JRNL-208590. December, 14, 2004.

110 Pavel Marcra and Antonin Fiala. Experimental residual stress analysis at welded pipelines.40th International conference experimental stress analysis. 3-6 VI 2002. Praha/Prague, Czech Republic.

111 Baczmanski, A. (Fac. of Phys. & Appl. Comput. Sci., AGH Univ. of Sci. & Technol., Krakow, Poland); Dakhlaoui, R.; Braham, C.; Wronski, S.;

Wierzbanowski, K.; Oliver, E.C., Effect of residual stresses on individual phase mechanical properties of austeno-ferritic duplex stainless steel. Acta Materialia 54,(2006), pp. 5027-5039.

112 Aruiz and P.B.Nagy. Residual stress assessment in surface-treated metals by laser-ultrasonic spectroscopy. Review of Quantitative Non-destructive Evaluation Vol 23, By D.O. Thompson and D.E. Chimenti. American Institute of physics (2004), pp. 1208-1215.

113 Becker, T.L., Jr. (Dept. of Mech. Eng., California Univ., Berkeley, CA, USA); Cannon, R.M.; Ritchie, R.O., An approximate method for residual stress calculation in functionally graded materials. Mechanics of Materials 32, (2000), pp. 85-97.

114 Lazoglu, I. (Dept. of Mech. Eng., Koc Univ., Istanbul, Turkey); Ulutan, D.; Alaca, B.E., Analytical modeling of residual stresses in machining. Journal of Material Processing Technology. (200^0, doi:10.1016/j.jmatprotec.2006.09.032.

115 H.K.Versteeg and W. Malalasekera. An Introduction to Computational Fluid Dynamics, the Finite Volume Method. Longman Scientific and Technical 1995.

116 Fluent Manual, Version 2d,dp, segrergated. Release: 6.1.22. Copyright © 1998, Fluent Inc.

117 S.Hogg and M..Leschziner. Second-moment-closure calculations of strongly swirling confined flow with large density gradients. International Journal of Heat and Fluid Flow, 10(1):16-27, 1989.

118 C.Benocci. Introduction to modeling of turbulence. 1991-02. Von -Karaman Institute of Fluid Dynamics, March 1991.

119 Pantankar, S.V. Computer analysis of fluid flow and heat transfer, chapter 8,

pages 223-252. Pineridge press Ltd, Swansea, U.K., 1981.

120 Pantankar, S.V. Numerical Heat Transfer and Fluid Flow, chapter 2, pages 15-16. Taylor &Francis, DC, 1980.

121 Kreith, Frank. Bohn, Mark S. principal of heat Transfer, Chapter 2, pages 78-81, 110-111. 5th edition. West Publishing Co.1993.

122 American Society of Heating, Refrigeration and Air-Conditioning Engineers, Inc, "ASHARAE Handbook 1981 Fundamentals". 1981. Ch 2, pp. 2.11-2.13.

123 Wood Group Pratt & Whitney, Industrial Turbine Services, LLC. Aramco GG4A-9B S/N P686916. Post M.S.I. Test Results. October 28th 2002.

124 Wood Group Pratt& Whitney Industrial Turbine Services, LLC. Aramco GG4A-9B, S/N P686907, Post M.S.I. Test Results. May 8th 2002.

125 ANSYS, Inc.2005 SAS IP, Inc. Release 10.

126 Yogesh K.Potdar and Alan T.Zehnder. Measurements and simulations of temperature and deformation fields in transient metal cutting. Journal of Manufacturing Science and Engineering, Vol. 125, pp. 645-655, 2003.

127 INSTRON 8801, Three-point testing facility, Instron Limited. Coronation Road, High Wycombe, Bucks, UK.

128 INSTRON 5569, tensile testing facilities, Instron Limited. Coronation Road, High Wycombe, Bucks, UK.

129 SEM -JEOL (U.K.) Limited, 35 Vine Street, London, EC3N 2PX.

130 Hollerith, C. (Dept. of Phys., Technische Univ. Munchen, Garching, Germany); Wernicke, D.; Buhler, M.; Feilitzsch, F.; Huber, M.; Hohne, J.; Hertrich, T.; Jochum, J.; Phelan, K.; Stark, M.; Simmnacher, B.; Weiland, W.; Westphal, W., "Energy dispersive X-ray spectroscopy with

microcalorimeters"Nuclear Instruments and Methods in Physics Research, Section A: Accelerators, Spectrometers, Detectors and Associated Equipment, (2004), Vol. 520 (1-3), pp. 606-609.

131 Mustapha, Z. (Henry Krumb Sch. of Mines, Columbia Univ., New York, NY, USA); Siu-Wai Chan; Lam, A.; Gerhardt, R., "Accuracy of energy dispersive X-ray composition analysis of YBCO films on yttrium-containing substrates as compared to Rutherford backscattering spectroscopy", Journal of Materials Science, (2000), Vol. 35 (2), pp. 443-448.

132 Boettinger, W.J. (Materials Science and Eng. Lab., Natl. Inst. of Stand. and Technol.); Vaudin, M.D.; Williams, M.E.; Bendersky, L.A.; Wagner, W.R., "Electron backscattered diffraction and energy dispersive X-ray spectroscopy study of the phase $NiSn_4$", Journal of Electronic Materials, Vol. 32 (6), pp. 511-515.

133 X-Ray Diffraction-D8 advance equipment. Bruker AXS GmbH, Oestliche Rheinbrueckenstr. 49 -D-76187, Karlsruhe, Germany.

134 Tube Furnace, Koyo Thermo Systems Co., Ltd. Company, Nara, Japan.

135 Micro-hardness Tester, Buehler Ltd, worldwide Headquarters, 41 Waukegan Road, P. O. Box 1, Lake Bluff, Illinois, USA.

136 Polishing wheel. Buehler Ltd, worldwide Headquarters, 41 Waukegan Road, P. O. Box 1, Lake Bluff, Illinois, USA.

137 Mounting Press. Buehler Ltd, worldwide Headquarters, 41 Waukegan Road, P. O. Box 1, Lake Bluff, Illinois, USA.

138 Optical Microscope Axioplan 2 Imaging. Carl Zeiss, Königsallee 9-21, 37081 Göttingen, Germany.

139 Kharlanova, E. (PyroGenesis, Inc.); Lafreniere, S.; Kim, G.E.; Brzezinski,

T.A., "Development of Tailored Metallographic Preparation Techniques for Thermally Sprayed Coatings", Proceedings of the International Thermal Spray Conference, (2000), pp. 967-970.

140 ASTM E45-5$^{\varepsilon 1}$ (2005), "Standard Test Methods for Determining the Inclusion Content of Steel", (2005).

141 ASTM D 790, "Standard Test Methods for Flexural Properties of Unreinforced and Reinforced Plastics and Electrical Insulating Materials". American Society for Testing and Material Standards, Philadelphia, (2003).

142 ASTM E8M-00B, "Standard Method of Tension Testing of Metallic Materials", American Society for Testing and Material Standards, Philadelphia, (2004).